

# **POLITECNICO DI TORINO**

Master Degree in  
Automotive Engineering

Master Degree Thesis

## **1D Modelling and Analysis of Thermal Conditioning Systems for Electric Vehicles**



Relatore  
Marco Masoero

Candidato  
Carlo Ciacci

Anno Accademico 2019/2020

## **Declaration of Originality**

I hereby certify that I am the sole author of this thesis and that no part of this thesis has been published or submitted for publication.

I certify that, to the best of my knowledge, my thesis does not infringe upon anyone's copyright nor violate any proprietary rights and that any ideas, techniques, quotations, or any other material from the work of other people included in my thesis, published or otherwise, are fully acknowledged in accordance with the standard referencing practices. Furthermore, to the extent that I have included copyrighted material that surpasses the bounds of fair dealing within the meaning of the Canada Copyright Act, I certify that I have obtained a written permission from the copyright owner(s) to include such material(s) in my thesis and have included copies of such copyright clearances to my appendix.

I declare that this is a true copy of my thesis, including any final revisions, as approved by my thesis committee and the Graduate Studies office, and that this thesis has not been submitted for a higher degree to any other University or Institution.

## **Abstract**

The limited driving range, due to the poor storage capability of electric batteries, represents one of the greatest challenges in the development of electric vehicles. This concern leads to an extremely demanding design of every component within the vehicle powertrain in order to achieve their maximum energy efficiency and decrease the demand on the battery. Additionally, in cold climate conditions, the efficiency of the heating system of an electric vehicle decreases and it can result in further reducing its driving range. In this thesis, 1D modelling in Amesim will be used to analyze different concepts of thermal management for an electric vehicle. Firstly, a 1D model of the original refrigeration system of the chosen vehicle (Fiat 500e) was built by implementing the data of each component. The components were individually modelled, then assembled within a system level model and the final model was validated. Secondly, starting with the validated system, a 1D model of a heat pump system was proposed as a replacement for the commonly used positive temperature coefficient heater (PTC). This model was obtained exploiting the information available on the refrigeration system and assuming all the unknown characteristics. An energy and exergy analysis was carried out to determine the individual components and overall system performance. Finally, the vehicle cabin was modelled exploiting a new Embedded CFD tool of Amesim capable of combining the advantages of 1D and 3D modelling, hence providing lower CPU resources and time consumption required to perform a simulation due to the lower effort to model the temperature distribution inside the cabin. This approach gives also the chance to study zonal heating and cooling of the cabin in order to reduce the energy demand on the battery. Numerous simulations were performed to analyze the impact of different settings and parameters validating each of them through comparison with experimental data.

## **Acknowledgements**

This work represents the peak of my academic path. I would have never expected to have the opportunity to be involved in such a life-changing project. This experience made me grow as a person, as a student and as a future worker thanks to the collaboration and kindness of the people that I met.

I would like to express my deepest gratitude to my academic advisor at University of Windsor, Dr. Ofelia A. Jianu, for the effort and passion you put into guiding me during the development of my thesis. Thanks to you I was able to understand the nature of academic research and develop a work skill that I am proud of.

I want to thank my academic advisor at Politecnico di Torino, Dr. Marco Masoero for supporting my project despite the distance.

Great thanks to my ARDC advisors, Shankar Natarajan and Pooya Mirzabeygi who continuously assisted and supported me throughout the entire project. Your collaboration allowed me to learn how to act and behave in a company.

I would like to thank my advisor at Centro Ricerche Fiat, Matteo Maria Rostagno. You helped and guided me with patience during the year to reach the goals of the project.

Special thanks to the coordinators of this project. Dr. Giovanni Belingardi, Dr. Jennifer Johrendt, Edoardo Rabino and Marie Mills for the great opportunity that they gave me and for their support during the year.

I would like to thank my committee members, Dr. Tam and Dr. Eaves, for spending time to review this thesis giving precious suggestions and contributions for its improvement.

I want to thank Ishant Dudhwal and Benoit Honel for the help you gave me while I was working on Amesim. Your contribution allowed me to explore into deep the possibilities of the software and, therefore, to add significant value to my research.

I would like to express my appreciation to Suresh Ganesan who went out of his way in order to help me retrieving information that were missing for long time.

Un sentito ringraziamento alla mia famiglia, Leonardo, Rossella e Marco che mi sostenete ogni giorno e senza i quali non sarei diventato la persona che sono. Grazie di cuore a Valentina, che non vedo l'ora di rivedere e che mi hai dato il tuo appoggio ogni giorno di quest'anno. Condividere New York con te ha reso il mio viaggio indimenticabile.

Gio, Greg, Pasqua e Ale non vedo l'ora di rivedervi e raccontarvi di questo lungo anno.

Ai miei compagni di viaggio Stefano e Paolo, condividere questa esperienza con voi l'ha resa ancora più unica. Grazie per il supporto, l'allegria e la compagnia che mi hanno permesso di sentirmi a casa pur così lontano.

James, Daniel, Mike thank you for welcoming us to Canada. I am really glad I could spend my year with you and I am grateful for all your support. I hope to see you again in Italy and return the favor. Stephen, Ewon and Max it was a pleasure to share this experience with you and I am looking forward to hanging out with you in Turin. A special thanks to Ewon for always driving me to the ARDC.

## Table of Contents

Declaration of Originality .....	ii
Abstract .....	iii
Acknowledgements .....	iv
List of Tables.....	viii
List of Figures .....	x
List of Abbreviations.....	xv
Chapter 1 – Introduction .....	1
1.1 Statement of the Purpose.....	1
1.2 Literature Review.....	2
1.3 Objectives and Contributions .....	17
Chapter 2 – Refrigeration cycle .....	18
2.1 Introduction.....	18
2.2 Vapour-compression cycle – cooling loop.....	19
2.3 Components modelling .....	21
2.3.1 Compressor.....	21
2.3.2 Condenser.....	23
2.3.3 Thermostatic expansion valve (TXV).....	27
2.3.4 Evaporator.....	29
2.4 System level model .....	31
2.5 Virtual refrigerant charge calculation .....	32
2.6 Model validation .....	34
2.6.1 Preparation of the model .....	34
2.6.2 Simulation set up.....	35
2.6.3 Result Comparison .....	39
Chapter 3 – Heat Pump Model.....	43
3.1 Introduction.....	43
3.2 Schematic of the system.....	43
3.3 Modelling.....	45
3.3.1 Components shared with the AC system.....	45
3.3.2 Components Added to the Loop.....	47
3.3.3 System level model .....	48
3.3.4 Results .....	51
3.4 Second simulation in different environmental conditions.....	55
3.5 Energy and Exergy Analysis .....	58
Chapter 4 – Cabin Model .....	63
4.1 Introduction.....	63

4.2 Embedded CFD Tool .....	63
4.3 Development of the Model.....	66
4.3.1 External Variables Input.....	67
4.3.2 Geometry Definition .....	70
4.3.3 Material Characterization .....	72
4.3.4 Stopping Criterion.....	72
4.3.5 Results cleaning.....	73
4.3.6 First simulation.....	74
4.3.7 Soaking Pre-simulation .....	77
4.4 Simulations with Gravity Enabled .....	80
4.4.1 Third Simulation .....	80
4.4.2 Fourth simulation .....	84
Chapter 5 – Conclusions and Future Work .....	87
5.1 Heat Pump Model .....	87
5.2 Cabin Model.....	88
5.3 Future work .....	89
References.....	90
Vita Auctoris .....	97

## List of Tables

Table 1. 1: Fanger Thermal Sensation Scale [53].	12
Table 2. 1: Input parameters for the calculation of the optimal virtual refrigerant charge.	33
Table 2. 2: Values of the validation metric and of the cumulative average error for the validation of the refrigeration cycle.	42
Table 3. 1: Input parameters of the heat pump model. These parameters will be also used for the calculation of the optimal virtual refrigerant charge.	50
Table 3. 2: Thermodynamic properties of the 4 states of the cycle performed by the heat pump shown in Figs. 2.7 and 2.8.	52
Table 3. 3: Thermodynamic properties of the air at the inlet and outlet of condenser and evaporator shown in Figs. 3.7 and 3.8.	54
Table 3. 4: Heat rejection in the heat exchangers evaluated from both the refrigerant and the air side.	54
Table 3. 5: Thermodynamic properties of the 4 states of the cycle performed by the heat pump shown in Figs. 3.9 and 3.10.	56
Table 3. 6: Thermodynamic properties of the air at the inlet and outlet of condenser and evaporator shown in Figs. 3.9 and 3.10.	57
Table 3. 7: Heat rejection in the heat exchangers evaluated from both the refrigerant and the air side.	58
Table 3. 8: Thermodynamic properties of the air at the inlet and outlet of condenser and evaporator.	60
Table 3. 9: Reference state considered for the refrigerant and the air.	60
Table 3. 10: Results of the energy and exergy analysis performed on the system proposed in paragraph 3.3.	62
Table 4. 1: Values of the validation metric and of the cumulative average error for the validation for the temperature of the 8 main volumes of the cabin and for the temperature of the recirculation air for the first simulation.	76
Table 4. 2: Values of the validation metric and of the cumulative average error for the validation for the temperature of the 8 main volumes of the cabin and for the temperature of the recirculation air for the second simulation.	80
Table 4. 3: Values of the validation metric and of the cumulative average error for the validation for the temperature of the 8 main volumes of the cabin and for the temperature of the recirculation air for the third simulation.	83

Table 4. 4: Values of the validation metric and of the cumulative average error for the validation for the temperature of the 8 main volumes of the cabin and for the temperature of the recirculation air for the fourth simulation. ....86

## List of Figures

Fig. 1. 1: Atmospheric CO <sub>2</sub> levels measured at Mauna Loa Observatory in Hawaii [2].	2
Fig. 1. 2: CO <sub>2</sub> levels during the last three glacial cycles, as reconstructed from ice cores [2].	3
Fig. 1. 3: R134a heat pump system structure and operation for electric vehicles [17].	5
Fig. 1. 4: Cooling and heating cycle, respectively, of a heat pump system determined by the position of a reversing valve.	6
Fig. 1. 5: Main element technologies of the electric compressor [20].	8
Fig. 1. 6: Schematic diagram of the microchannel evaporator: (a) Front view (left) and side view (right) of the microchannel evaporator; (b) Louver fin used in the microchannel evaporator; (c) Microchannel tube [27].	9
Fig. 1. 7: Bi-directional receiver/expansion device [31].	10
Fig. 1. 8: Predicted Percentage Dissatisfied (PPD) as a function of Predicted Mean Vote (PMV) [53].	13
Fig. 1. 9: Thermal comfort zones defined by ASHRAE standard 55 [52].	13
Fig. 1. 10: 1D model of the cabin of a vehicle built in AMESim.	14
Fig. 1. 11: Post-Processor tool in AMESim for the calculation of the occupant thermal comfort indexes.	14
Fig. 1. 12: Factors that influence the cabin heat load [60].	15
Fig. 2. 1: Phases of the modelling process followed to build the AC system for the refrigeration loop.	18
Fig. 2. 2: T-s diagram of a general vapour-compression refrigeration cycle [2].	20
Fig. 2. 3: p-h diagram of a general vapour-compression refrigeration cycle [2].	20
Fig. 2. 4: Element adopted for the modelling of the compressor; list of external variables and parametrization.	21
Fig. 2. 5: Isentropic efficiency (Y) defined as a function of the compression ratio (X1) [null] and the angular speed (X2) [RPM].	22
Fig. 2. 6: Volumetric efficiency (Y) defined as a function of the compression ratio (X1) [null] and the angular speed (X2) [RPM].	23
Fig. 2. 7: Model of the condenser connected with the heat exchanger (HEX) calibration tool.	24
Fig. 2. 8: Element adopted for the modelling of each pass element of the condenser; list of external variables and parametrization (the pass shown is the fourth).	24
Fig. 2. 9: Element adopted for the modelling of the integrated receiver; list of external variables and parametrization.	25
Fig. 2. 10: Calibration of the thermodynamic performances of the condenser using the heat exchanger calibration tool provided by AMESim.	27

Fig. 2. 11: Element adopted for the modelling of the thermostatic expansion valve; list of external variables and parametrization.....	28
Fig. 2. 12: A four-dimension diagram characterizing the thermostatic expansion valve. ....	29
Fig. 2. 13: Element adopted for the modelling of the evaporator.....	30
Fig. 2. 14: Calibration of the thermodynamic performances of the evaporator using the heat exchanger calibration tool provided by AMESim.....	31
Fig. 2. 15: Assembled model of the AC system responsible for cooling operations. ....	31
Fig. 2. 16: Graph collecting the behavior of the refrigerant subcooling after the condenser for all the simulations performed, the plateau used for the calculation of the refrigerant charge is highlighted in red and it is limited by 6.5 and 9 oz. ....	33
Fig. 2. 17: Modified model of the AC system ready to be validated. a) Branch of the system with the added TXV and chiller; b) electronic control of the compressor RPM to obtain a minimum temperature of the evaporator outlet air of 10 °C.....	35
Fig. 2. 18: Graph showing the speed of the vehicle during the simulation as a function of time. ....	36
Fig. 2. 19: Behavior of the air temperature measured in different points of the condenser front as a function of time: in red the average one.....	37
Fig. 2. 20: Behavior of the relative humidity of the air at the condenser inlet as a function of time. ....	37
Fig. 2. 21: Behavior of the mass flow rate of the air flowing through the condenser as a function of time.....	38
Fig. 2. 22: Behavior of the air temperature measured in the recirculation duct. ....	39
Fig. 2. 23: Behavior of the assumed absolute humidity of the air flowing through the evaporator. ....	39
Fig. 2. 24: Comparison between the numerical evaporator outlet air temperature and the experimental one. ....	40
Fig. 2. 25: Comparison between the numerical evaporator outlet refrigerant temperature and the experimental one. ....	40
Fig. 2. 26: Comparison between the numerical compressor head pressure and the experimental one. ....	41
Fig. 3. 1: Schematic of the refrigeration cycle in the new structure of the system: the refrigerant goes through two bypass valves after the compressor, flows in the external heat exchanger (operates as a condenser), and it is directed by the three-way valve in a TXV and in the internal evaporator, completing the loop back to the compressor. ....	43
Fig. 3. 2: Schematic of the heat pump cycle in the new structure of the system: the refrigerant goes through the internal condenser after the compressor, into an expansion valve, which precedes the external heat exchanger (operates as an evaporator) and finally is redirected to the compressor by the three-way valve. ....	44

Fig. 3. 3: Basic model of the AC system highlighting the components to be implemented also in the heat pump system. ....	46
Fig. 3. 4: Element adopted for the modulated generic restriction representing the expansion valve; list of external variables and parametrization.....	47
Fig. 3. 5: Heat pump model with highlighted the components shared with the AC system. ....	49
Fig. 3. 6: Graph collecting the behavior of the refrigerant subcooling after the condenser for all the simulations performed, the plateau used for the calculation of the refrigerant charge is highlighted in red and it is limited by 3 and 9 oz. ....	51
Fig. 3. 7: Pressure-enthalpy diagram of the thermodynamic cycle performed by the heat pump (from 1 to 2 the compressor, from 2 to 3 the condenser, from 3 to 4 the expansion valve and from 4 to 1 the evaporator). ....	53
Fig. 3. 8: Temperature-entropy diagram of the thermodynamic cycle performed by the heat pump (from 1 to 2 the compressor, from 2 to 3 the condenser, from 3 to 4 the expansion valve and from 4 to 1 the evaporator). ....	53
Fig. 3. 9: Pressure-enthalpy diagram of the thermodynamic cycle performed by the heat pump (from 1 to 2 the compressor, from 2 to 3 the condenser, from 3 to 4 the expansion valve and from 4 to 1 the evaporator). ....	56
Fig. 3. 10: Temperature-entropy diagram of the thermodynamic cycle performed by the heat pump (from 1 to 2 the compressor, from 2 to 3 the condenser, from 3 to 4 the expansion valve and from 4 to 1 the evaporator). ....	57
Fig. 3. 11: Simple schematic of the heat pump system to define each state of the cycle: 1 refrigerant evaporator outlet/compressor inlet, 2 refrigerant compressor outlet/condenser inlet, 3 condenser outlet/expansion valve inlet, 4 expansion valve outlet/evaporator inlet, 5 air evaporator inlet, 6 air evaporator outlet, 7 air condenser inlet, 8 air evaporator outlet. ....	59
Fig. 4. 1: Representation of the cabin space split in 10 volumes. ....	64
Fig. 4. 2: The Embedded CFD Tool and its external variables. ....	65
Fig. 4. 3: Graph showing the speed of the vehicle during the simulation as a function of time. ....	67
Fig. 4. 4: Graph showing the temperature of the wind tunnel during the simulation as a function of time.....	68
Fig. 4. 5: The air vents used in the cool down test are shown in red.....	68
Fig. 4. 6: Behavior of the assumed absolute humidity of the air flowing through the evaporator. ...	69
Fig. 4. 7: Temperature of the air flowing in the top front vents during the cool down test. ....	69
Fig. 4. 8: Dimensions required to parametrized the CAD geometry: external dimensions of the car cabin on the left; dimensions of the seats on the right. ....	70
Fig. 4. 9: Side view of the match between the virtual shape and the cabin CAD to extrapolate the measurements needed in the geometry definition. ....	71

Fig. 4. 10: Front view of the match between the virtual shape and the cabin CAD to extrapolate the measurements needed in the geometry definition. ....	71
Fig. 4. 11: Instants (in red) at which the simulation on Amesim stops and asks to STAR-CCM+ for an update on the boundary conditions, compared to the profile of the vehicle speed (in black). ....	73
Fig. 4. 12: Comparison between the experimental values measured from the thermocouple Head Front Left and the numerical results obtained for the zone Top Front Left (TFL) in the first simulation. ....	75
Fig. 4. 13: Comparison between the experimental values measured from the thermocouple Head Front Right and the numerical results obtained for the zone Top Front Right (TFR) in the first simulation. ....	75
Fig. 4. 14: Comparison between the experimental values measured from the thermocouple Feet Rear Passenger Left and the numerical results obtained for the zone Bottom Rear Left (BRL) in the first simulation. ....	76
Fig. 4. 15: Behavior of the temperature of the 10 volumes during the soaking simulation, at 1922 s the average temperature reaches 60 °C. ....	78
Fig. 4. 16: Comparison between the experimental values measured from the thermocouple Head Front Left and the numerical results obtained for the zone Top Front Left (TFL) in the second simulation. ....	79
Fig. 4. 17: Comparison between the experimental values measured from the thermocouple Feet Rear Passenger Left and the numerical results obtained for the zone Bottom Rear Left (BRL) in the second simulation. ....	79
Fig. 4. 18: Comparison between the experimental values measured from the thermocouple Head Front Right and the numerical results obtained for the zone Top Front Right (TFR) in the first attempt of the third simulation. ....	81
Fig. 4. 19: Instants (in red) at which the simulation on Amesim stops and asks to STAR-CCM+ for an update on the boundary conditions, compared to the profile of the vehicle speed (in black). ....	82
Fig. 4. 20: Comparison between the experimental values measured from the thermocouple Head Front Left and the numerical results obtained for the zone Top Front Left (TFL) in the third simulation. ....	82
Fig. 4. 21: Comparison between the experimental values measured from the thermocouple Feet Rear Passenger Left and the numerical results obtained for the zone Bottom Rear Left (BRL) in the third simulation. ....	83
Fig. 4. 22: Behavior of the temperature of the 10 volumes during the soaking simulation, at 1708 s the average temperature reaches 60 °C. ....	84
Fig. 4. 23: Comparison between the experimental values measured from the thermocouple Head Front Left and the numerical results obtained for the zone Top Front Left (TFL) in the fourth simulation. ....	85

Fig. 4. 24: Comparison between the experimental values measured from the thermocouple Feet Rear Passenger Left and the numerical results obtained for the zone Bottom Rear Left (BRL) in the fourth simulation. ....85

## List of Abbreviations

CO <sub>2</sub>	Carbon Dioxide
NASA	National Aeronautics and Space Administration
HSB	Hybrid System Battery
HEV	Hybrid Electric Vehicle
CSEEs	Cold-Start Extra Emissions
EV	Electric Vehicle
PHEV	Plug-In Electric Vehicle
ICE	Internal Combustion Engine
BEV	Battery Electric Vehicle
SOC	State of Charge
PTC	Positive Temperature Coefficient
HVAC	Heating, Ventilation and Air Conditioning
TXV	Thermostatic Expansion Valve
AC	Air Conditioning
MCHX	Micro-Channel Heat Exchanger
DHP	Dehumidifying Heat Pump
COP	Coefficient of Performance
HPAC	Heat Pump Air Conditioner
SLHP	Secondary Loop Heat Pump
RHP2	Regenerative High-Performance Heat Pump
GWP	Global Warming Potential
EXV	Electric Expansion Valve
PMV	Predicted Mean Vote
PPD	Predicted Percentage Dissatisfied
RH	Relative Humidity
CAD	Computer-Aided Design
CFD	Computational Fluid Dynamics
CPU	Central Processing Unit
HBM	Heat Balance Method
SAE	Society of Automotive Engineers
RPM	Revolutions Per Minute
FCA	Fiat Chrysler Automobiles
PI	Proportional Integral
RI	Relative Irreversibility

ECFD	Embedded CFD
PVB	Polyvinyl Butyral
EVA	Ethylene-Vinyl Acetate
TFL	Top Front Left
TFR	Top Front Right
TRL	Top Rear Left
TRR	Top Rear Right
BFL	Bottom Front Left
BFR	Bottom Front Right
BRL	Bottom Rear Left
BRR	Bottom Rear Right
WS	Windshield
RS	Rear shield

## **Chapter 1 – Introduction**

### **1.1 Statement of the Purpose**

The heating system of an internal combustion engine vehicle is composed of a heat core, which exploits the waste heat withdrawn by the engine coolant. However, an electric vehicle motor does not release large amounts of heat that could be recovered and reused to warm the air in the car cabin. Therefore, alternative heat sources are needed to perform the heating operations in cold climate conditions. A solution widely used in many electric vehicles, among them also the previous version of the Fiat 500e, is the positive temperature coefficient heater (PTC heater). Even if electric heaters usually have a high First Law efficiency, in cold climate conditions such systems become the largest energy consumption system in the vehicle. In order to decrease the energy demand on the battery by the heating system, a heat pump system has been proposed as an alternative or supporting solution for two reasons. Firstly, a heat pump system operates using the same thermodynamic cycle used in the air conditioning (AC) system, the vapour-compression cycle, with the purpose of rejecting heat to the cabin environment instead of withdrawing it. This can be achieved by inverting the direction of the heat rejection, hence reverting the direction of the cycle. Therefore, it is possible to implement the system in the vehicle with limited addition to its weight by exploiting components already present in the refrigeration cycle. Secondly, the coefficient of performance (COP) of a heat pump system is usually higher than 1, which means that with a kilowatt of electric energy the system should be able to transfer 2, 3 or even 4 kilowatts of heat to the cabin environment.

The design of an HVAC system for a vehicle is dependent on its effects on the cabin of the vehicle. Hence, a common approach by the automotive industry is to develop a cabin model in a 1D software. One of the most important reasons behind this approach is to determine the temperature and the relative humidity achieved inside the vehicle without having to develop a complex and expensive (in time and computational resources) CFD simulation and/or experimental model. According to this, a 1D software gives the chance to consider the entire space inside the vehicle as a lumped mass interacting with different thermic loads and calculate its temperature and relative humidity (they are considered as an average inside the cabin). This approach could be sufficient to obtain some useful information at early design stages, but many companies are experimenting new solutions to improve their know-how on this matter.

## 1.2 Literature Review

As powertrains continue to increase in efficiency, less engine waste heat is available for warming the passenger compartment. In order to still be able to conduct the operations of comfort heating and defogging windows, it is necessary to look for alternative heat sources. M. Hosoz and M. Direk [1] studied the performance characteristics of a R134a automotive air conditioning system capable of operating as an air-to-air heat pump using ambient air as a heat source. They concluded that the system could provide enough heat only when the temperature is not particularly low, otherwise as the temperature dropped, the heating performance degraded dramatically.

Along with this issue, the automotive industry has to face another great concern regarding the environmental pollution and CO<sub>2</sub> emissions. The graphs published by NASA [2] show: the atmospheric CO<sub>2</sub> levels measured at Mauna Loa Observatory in Hawaii (Fig. 1.1) and the CO<sub>2</sub> levels during the last three glacial cycles, as reconstructed from ice cores (Fig. 1.2). It is evident that the level of CO<sub>2</sub> has been increasing in the past decades reaching the highest levels on history.

### DIRECT MEASUREMENTS: 2005-PRESENT

Data source: Monthly measurements (average seasonal cycle removed). Credit: NOAA

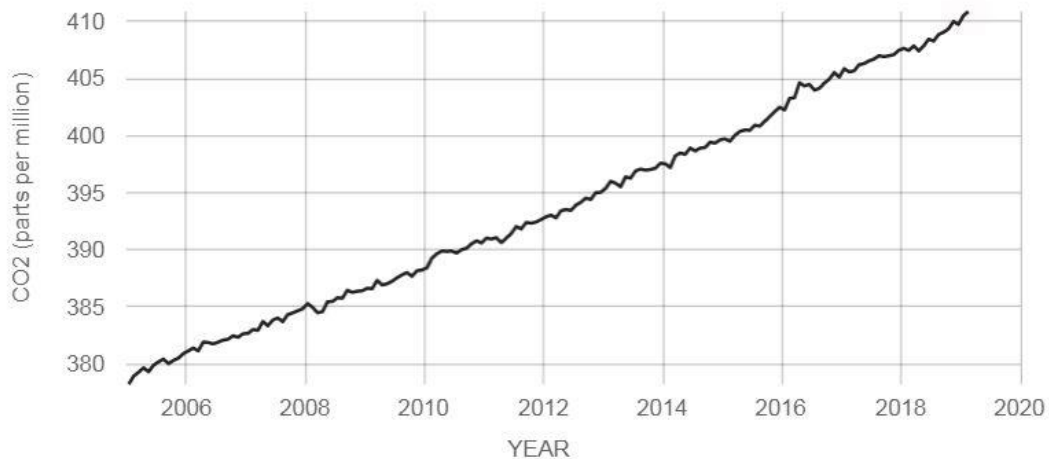


Fig. 1. 1: Atmospheric CO<sub>2</sub> levels measured at Mauna Loa Observatory in Hawaii [2].

## PROXY (INDIRECT) MEASUREMENTS

Data source: Reconstruction from ice cores.  
Credit: NOAA

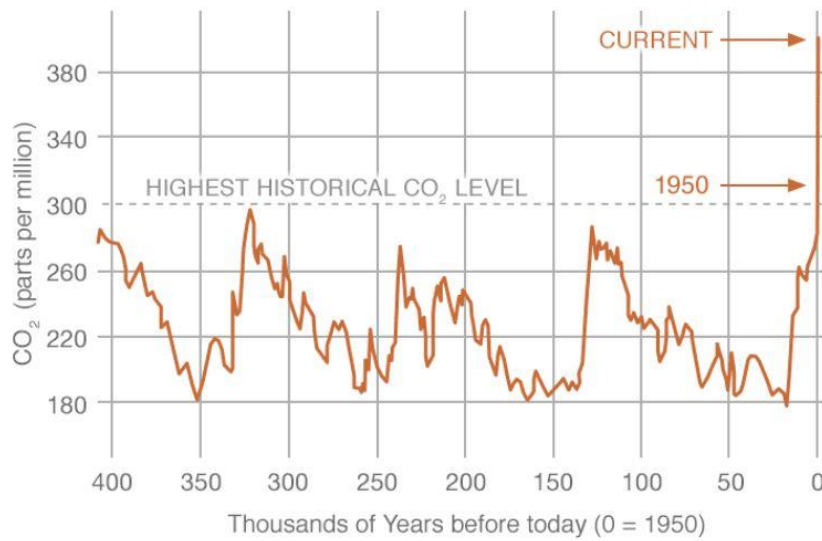


Fig. 1. 2: CO<sub>2</sub> levels during the last three glacial cycles, as reconstructed from ice cores [2].

In 2005, automotive pollution was responsible for 20% of the European Union's CO<sub>2</sub> emissions, roughly 60% of which can be attributed to private automobiles [3]. In order to address this problem, through the years the EU legislation set mandatory emission reduction targets for new cars in order to meet the targeted 95 grams of CO<sub>2</sub> per kilometer by 2021, a significant drop from the 130 grams per km recorded in 2015 [4]. Emissions limits are set according to the mass of the vehicle, using a limit value curve. This means that heavier cars are allowed higher emissions than lighter cars, so only the fleet average is regulated. One of the most effective solutions that has been adopted by companies is the electric vehicle. In their work R. Alvarez and M. Weilenmann [5] firmly stated that the recuperated kinetic vehicle energy stored as electric energy in a hybrid system battery (HSB) used in hybrid electric vehicles (HEVs) has great potential to reduce vehicle fuel consumption and CO<sub>2</sub> emissions. In this study, they investigated the influence of low ambient temperatures on HEV fuel consumption, pollutant and CO<sub>2</sub> emissions. The experimentation showed a reduction (30-85% on average) of the amount of HEV cold-start extra emissions (CSEEs) of regulated pollutants with respect to conventional gasoline vehicles. An interesting study published by R. T. Doucette and M.D. McCulloch [6] modelled the CO<sub>2</sub> emissions of electric vehicles (EVs) and plug-in Hybrid electric vehicles (PHEVs) and compared them with the ones produced by conventional vehicles with internal combustion engine (ICEs). In this scenario they concluded that PHEVs may be able to emit less CO<sub>2</sub> than both conventional vehicles and EVs, considering certain given power generation mixes, for two important reasons: they require less batteries than EVs, hence they are lighter; they can operate their onboard ICEs more efficiently than conventional vehicles.

The efficiency improvement of internal combustion engines has led to a low amount of heat waste to exploit as a source for the heating system of the vehicle's cabin. On the other hand, electric vehicles do not release any waste heat which means that other sources are needed to perform the thermal management of the vehicle with one source for heating being the conversion from electric energy. However, the electric energy used for cabin heating can drastically affect the operating range of electric vehicles, even resulting even in up to a 50% reduction in range under extreme cold conditions [7]. In their studies, A. Lajunen [7] performed a simulation model of cabin heating and cooling system developed in the Amesim to understand the impacts of the cabin HVAC system configuration on the vehicle energy consumption. Similar research has been conducted by J. Neubauer and E. Wood [8] in order to evaluate the effects of ambient temperature conditions and driver aggression on the utility of battery electric vehicle (BEV). The primary challenge against cold-climate BEV operation is the inefficiency of the cabin heating systems, which request an excessive amount of energy from the battery, and the inefficiency of the battery itself. Hence, one of the limitations of lithium-ion (Li-ion) batteries, which at the moment are used for both EVs and PHEVs, is their poor low-temperature performance. In their work J. Jaguemont, L. Boulon and Y. Dubé [9] studied the effects of low temperatures on batteries performances pointing out three main issues and their contributions on capacity/power fade: reduction of battery's available energy; increase of battery's internal impedance; performance-hampering cell degradation. Khoury and Clodic [10] in their paper performed experiments in order to study the effect of electrical AC operation on electricity consumption in a hybrid electric vehicle. The tests demonstrated that the AC system became the largest energy consumption system, thus having a high impact on overall vehicle fuel consumption. A consideration worthy of note is that the procedures adopted for these tests take into account the driving conditions and the state of charge of the batteries (SOC) due to the climatic conditions.

The most common separate heater used to ensure cabin thermal comfort in cold environments is the positive temperature coefficient (PTC). This electric heater is used either to warm up a cooling liquid or to directly heat the cabin air flow. In [11] the design and the analysis of a PTC heater for electric vehicles were presented and the performance characteristics were investigated experimentally. In their paper R. Musat and E. Helerea [12] presented PTC heaters as an auxiliary device in ICE vehicles to improve the conventional heating system. The issue is that the PTC heater demands a large quantity of electric current, hence it operates only when the engine is running which causes the fuel consumption to increase hence raising pollution during operation of ICE. According to that, using such a device on an electric vehicle leads to an excessive reduction in the driving range [7]. Furthermore according to the studies of B. Torregrosa, J. Paya and J.M. Corberan [13] there are some other barriers for the use of PTC: among these there are the high cost with high power and more energy consumption. From the results of their studies, they realized that the use of PTC can affect the driving distance with fully charged batteries, leading to losses up to 24%.

In a research project conducted on an internal combustion engine vehicle, the benefits of using a heat pump instead of the conventional air conditioning were assessed [14]. Measuring and comparing the in-car heating curve the authors stated that the heat pump system had a better performance than the baseline one of their vehicle. In mild temperatures the driving range of electric vehicles can be improved by the heat pump system in comparison to a conventional HVAC system consisting of air conditioning and PTC heater, by recovering waste heat from the power electronics and electric motor and using the heat to increase the performance of the heat pump [7]. According to these and several research sources [15]–[17], the heat pump air conditioning system is a potential climate control system in order to improve its efficiency and to avoid further limitations on the operating range of electric vehicles. Extensive literature reviews have been performed on different aspects concerning heat pump: a review of applications of alternative environmentally friendly refrigerants and of advanced technologies, innovative components and system structures for electric vehicles [15]; another one on the mobile heat pump cycle design, system performance and alternative working fluids [16]; and a third one on recent developments in heat pump technologies classified under energy efficiency, hybrid systems novel solutions/applications [17]. The literature indicates that heat pumps could be a viable solution to improve the thermal management energy efficiency in electric vehicles, becoming a key component in an energy recovery system with great potential for energy saving. The paper published by T. Suzuki and K. Ishii [18] is the first one to present an R134a heat pump system for EVs with open experimental data. In their study, the adoption of a 4-way valve to reverse the refrigerant flow direction, as shown in Fig. 1.3, was proposed in order to improve the system efficiency.

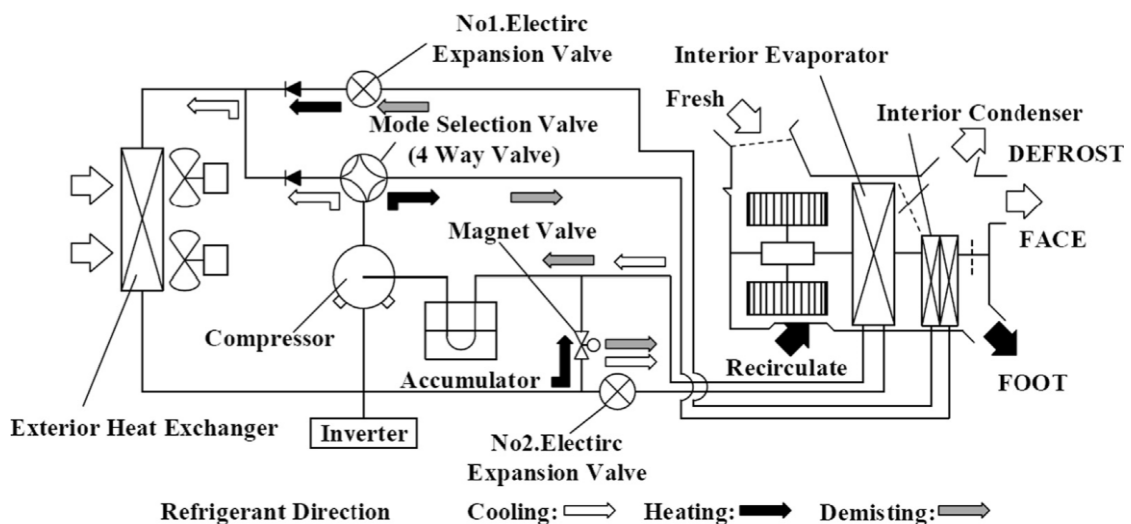


Fig. 1. 3: R134a heat pump system structure and operation for electric vehicles [17].

Today there are many different types of heat pumps available on the market that can be categorized in different categories according to various features: either by the cycle type adopted by the heat pump (for example, vapour compression cycle, absorption cycle, chemical reaction cycle); or by energy requirements for operation (which could be external mechanical work or external thermal energy) [17].

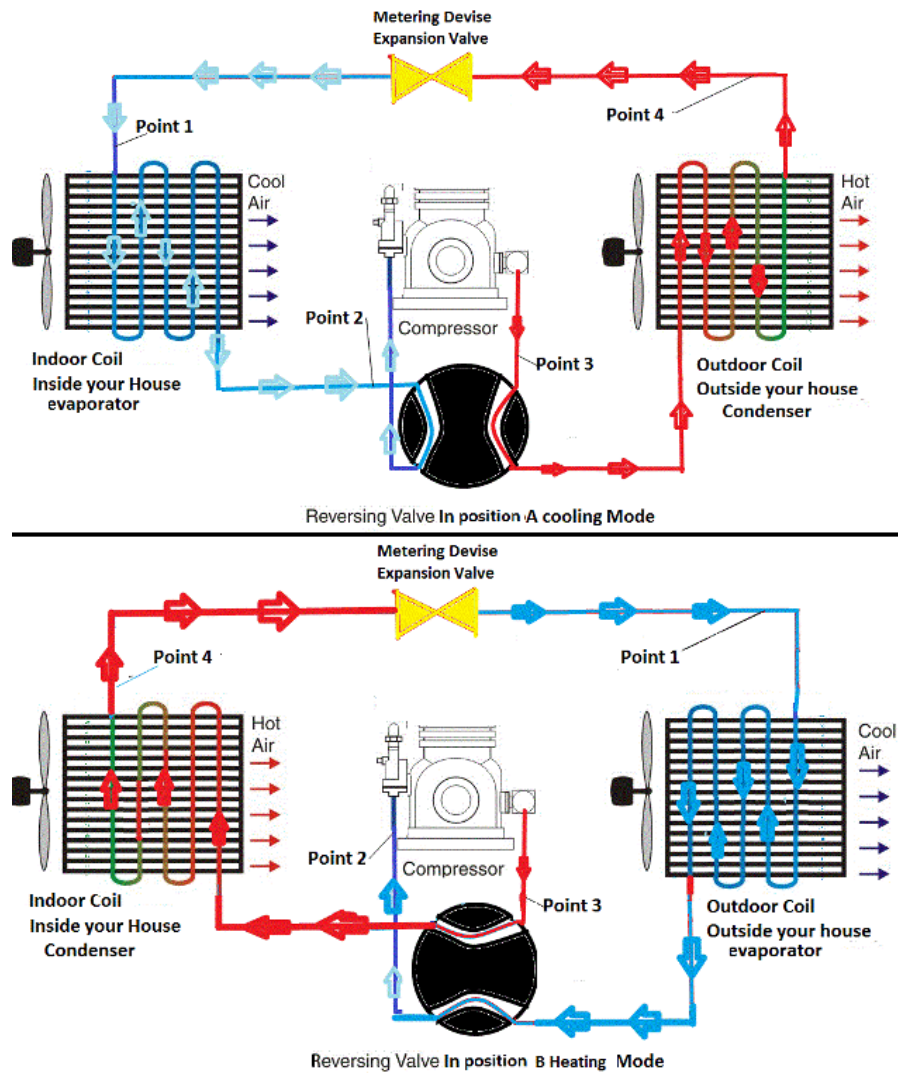


Fig. 1. 4: Cooling and heating cycle, respectively, of a heat pump system determined by the position of a reversing valve.

One of the most common commercial heat pumps is based on the vapour compression cycle. The fundamental components needed to perform this cycle are: a compressor, a condenser, a pressure regulating device and an evaporator [19]. The compressor pressurizes the working fluid, in its gaseous state, and allows it to flow along the system. Any liquid refrigerant will destroy the compressor. The condenser is a heat exchanger used to dissipate the heat from the working fluid towards the flow of air. The pressure regulating device could be an orifice tube or a thermostatic expansion valve (TXV) which are used to control the refrigerant flow through the evaporator. The

TXV requires liquid refrigerant to operate efficiently and avoid it to freeze itself. The evaporator is a heat exchanger used to perform the heat transfer from the air towards the refrigerant. In order to be able to perform both the heating and cooling functions, the system needs a valve that can allow to reverse the flow (Fig. 1.4). In the system there are other devices that are used to realize secondary operations which are not essential for its functioning.

The first step to increase the efficiency and performance of heat pump systems is to improve its individual components starting from the fundamental ones. Makino et al. [20] developed an electric compressor capable of achieving high reliability; low vibration and noise; small size, light weight, and high efficiency (Fig. 1.5). Another advantage of using an electric compressor is that they have low refrigerant emissions, flexible packaging and an efficient variable speed operation [21]. As an alternative to the traditional configuration with scroll compressor motor and separate main electric motor, R. Baumgart et al. [22] developed an innovative and energy efficient drivetrain structure for electric vehicles which integrates the compressor motor directly into the drivetrain. The advantages of this new configuration are many. Firstly, it is possible to switch from the compressor motor to the main motor or vice-versa so that in certain situations the main motor can be used to drive the compressor, hence allowing to its operating point to be shifted to a better efficiency. On the other hand, when the efficiency of the compressor motor is higher than the one of the main motor, it can be used to drive the vehicle itself. Secondly, this configuration leads to better results in terms of space installation, weight and costs. There are many different manufactures of air-conditioning compressors (piston-type, vane-type, scotch yoke and scroll compressors), which operate similarly [19]. Wei *et al.* [23] experimentally compared the performances of an EV heat pump AC system using different types of compressors: a swash plate variable displacement compressor, a scroll compressor and an electric scroll compressor. The swash plate-based system obtained the best results in terms of average vehicle cabin temperature when the ambient one was below 10°C. Moreover, D. Krähenbühl et al. [24] developed a miniature electrically driven turbocompressor which allowed the reduction of heating, ventilation, and AC system to an ultra-compact size maintaining high efficiency. This was achieved by increasing the rotational speed of the compressor to 500 000 rpm and employing new electrical drive system technology and materials.

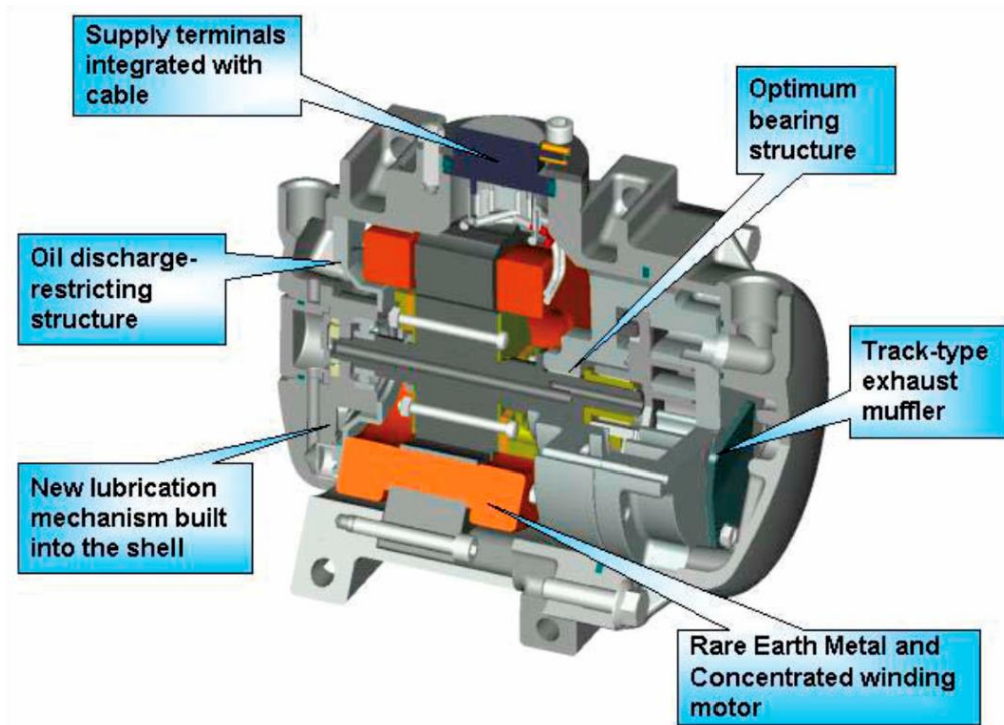


Fig. 1. 5: Main element technologies of the electric compressor [20].

Another component that offers great possibilities for improvement is the heat exchanger (condenser or evaporator) as Cummings *et al.* [25] showed in their comprehensive review of testing of AC heat exchangers in vehicles. One of the greatest developments in the heat exchanger technologies is the use of micro-channel heat exchanger (MCHX). Among its many advantages are higher heat transfer rate, less refrigerant charge needed, compact structure and low costs, as shown in the review published by Y. Han et al. [26] and experimentally demonstrated in the paper written by Z. Qi et al. [27]. The disadvantage of the MCHX is that in cold weather conditions the AC system frequently focus on the defrosting cycle affecting the heating capacity and the heating performance coefficient [15].

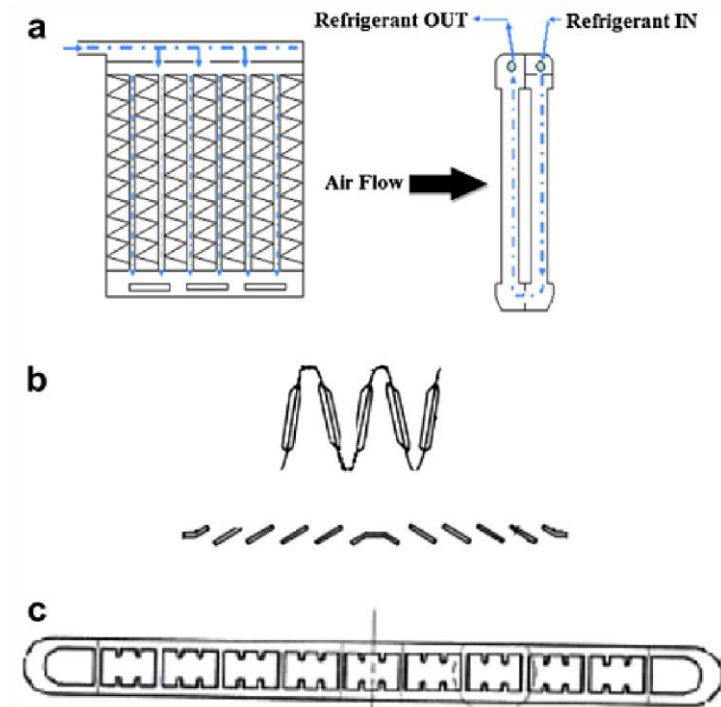


Fig. 1. 6: Schematic diagram of the microchannel evaporator: (a) Front view (left) and side view (right) of the microchannel evaporator; (b) Louver fin used in the microchannel evaporator; (c) Microchannel tube [27].

In order to further increase the performance of the heat pump, other studies have been conducted to develop new technologies for improvement. A dehumidifying heat pump (DHP) has been proposed to save energy consumption in electric vehicles during the dehumidifying and heating operation [28]. The objective of this study is to investigate the performance improvement of a DHP by using various additional heat sources (such as air source, waste heat source, and dual heat source of air and waste heat) in electric vehicles with low occupancy. Heat pump performance degradation is inevitable at very low ambient temperatures. For this reason in [29] the authors introduced a vapor injection heat pump system to overcome the performance degradation thus increasing heat recovery in the evaporator and improving heating capacity and the coefficient of performance (COP). Another configuration of the system has been proposed in order to scavenge heat from unused sources providing heating with COP greater than 1 [30]. The Unitary Heat Pump Air Conditioner (HPAC) provides hot and cold coolant that is used to manage the vehicles thermal needs. V. Pomme [31], describing a heat pump for electric vehicles similar to the one proposed by T. Suzuki and K. Ishii [18], introduced a specially designed device called bi-directional receiver/expansion device (Fig. 1.7). In this way the system can still perform its functions (refrigerant filtering and drying, refrigerant accumulator, refrigerant expansion and heating/cooling mode operation) while replacing six components with a single one. The system was also improved with an additional external heat source to exploit the waste heat of the main battery to save energy on itself: the results showed a saving of about 15% with respect to PTC.

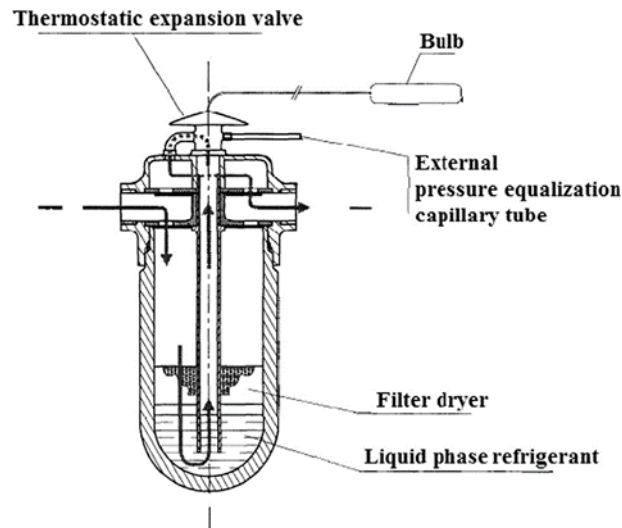


Fig. 1. 7: Bi-directional receiver/expansion device [31].

Studying new technologies to enhance the heat pump system is not the only way to improve its efficiency: another important field of research is the development of different configurations of the system in order to obtain the best achievable results. One study has investigated the feasibility of a dual source heat pump in an electric vehicle using both air and heat waste to increase thermal efficiency of the pump [32]. Another proposed configuration exploits the use of a dual-evaporator heat pump system for effective dehumidifying and heating of the cabin using waste heat recovery from the dehumidifying process [33]. This system showed superior performance to the conventional AC system in the dehumidifying and heating operation. One more research on heat pump investigated the characteristics of R134a mobile heat pump system for electrical vehicle application and compared two different configurations, direct heat pump and secondary loop heat pump (SLHP), considering: effects of indoor and outdoor temperatures on system performance; impacts of coolant flow rate on the capacity and COP; heat transfer effectiveness of heater core and plate heat exchanger [34]. This latter solution achieved to improve air outlet temperature uniformity, but with harmful effects on systems efficiency. The secondary loop causes a great loss for the COP, but its impact on heating capacity is almost negligible. S. Bilodeau [35] introduced a new integrated climate control system called Regenerative High Performance Heat Pump (RHP2) in which, waste heat during the exothermic battery operation and thermal energy recovered from evacuated stale air were taken into account. The tests performed indicated that the system could operate independent of weather conditions as low as  $-25\text{ }^{\circ}\text{C}$  without loss of COP. On the other hand D. Antonijevic and R. Heckt [36] developed a supplemental heat pump system for mobile heating system in order to gain an additional 1.5-3.0 kW heat capacity under different climatic and driving conditions.

A great concern in the development of cooling systems is the choice of the working fluid. This decision is critical in order to achieve the best trade-off between performances and environmental

sustainability. At present, the refrigerant R-134a is still dominant in automotive AC systems, although it has a global warming potential (GWP) of 1300. The global warming potential is a measure of how much heat is trapped in the atmosphere by a greenhouse gas up to a specific time horizon (20, 100, 500), referred to the amount of heat

Trapped by a similar mass of carbon dioxide (whose GWP is standardized to 1). For future environmental considerations this solution is no longer considered acceptable and many measures are being taken: the Kyoto and Montreal protocols have banned or limited the use of chemical refrigerants [37] and similarly, the European Union has passed regulations to restrict the use of refrigerants with a GWP higher than 150 in mobile AC systems [38]. Much research has been conducted to study different alternatives for the coolant adoption [15], [16]. The review performed by Z. Qi in [16] presents different heat pump systems analyzing AC/HP based on a vapour compression cycle with different working fluid (R-134a, CO<sub>2</sub>, R-152a, R-290, R-600a and R-C270) and AC/HP based on different applications, such as magnetocaloric or thermoelectric effect. Among these, the heat pump using CO<sub>2</sub> refrigerant as a working fluid is one of the most studied options because of its adequate thermophysical properties and its lack of ozone depletion potential (GWP = 1) [39], [40]. Experimental tests evaluated the effects on system performance of outdoor temperature, outdoor air velocity, indoor temperature, indoor air flow rate, compressor speed, and electric expansion valve (EXV) opening [41]. In an environment in which the working fluid replacement problem becomes increasingly prominent, the natural refrigerant CO<sub>2</sub> becomes one of the potential candidates of alternative refrigerants. Other studies experimentally assessed the performances of a prototype of R-744 (CO<sub>2</sub>) refrigeration system operating in both air conditioning and heat pump mode in supercritical regions [42], [43]. The results show significant heating capacity at relatively low operating temperatures and higher capacity at heating up transient. Although CO<sub>2</sub> AC systems have special benefits, they have some disadvantages, such as low critical temperature and high operating pressure [44]. In order to enhance the performances S.C. Kim et al. [45] re-arranged the radiator and outdoor heat exchangers of the CO<sub>2</sub> heat pump system in electric cars, obtaining an increase of the heating capacity by 54% and of the COP by 22%. The R-1234yf (2,3,3,3-Tetrafluoropropene) is the first of a new class of refrigerants designed to replace the R-134a as working fluid: it has a GWP lower than 1 [46]. In their work [47] Y.H. Lee and D.S. Jung performed a comparison between R-1234yf and R-134a. It was determined that the COP and capacity of the former were up to 2.7% and 4.0% lower than those of the latter, respectively, while the compressor discharge temperature and amount of refrigerant charge were 6.5 °C and 10% lower. Consequently, the R-1234yf AC system can be considered the most feasible candidate for automobiles from the standpoint of system performance and operating conditions. However different resources [47]–[49] stated that more work has to be completed before the R-1234yf system can be widely accepted in EVs.

A fundamental aspect of the research conducted on the cooling system is the study of the thermal management of the cabin in order to fulfill the prime objective of an HVAC system: provide thermal comfort to the passengers. The first step to understand this concept requires to give a definition of thermal comfort. Reading through the literature and the regulations, it is easy to find many of those and I am reporting here the ones that in my opinion are more significant. The regulation DIN EN ISO 7730 defines thermal comfort as “that condition of mind, which expresses satisfaction with the thermal environment” [50]. Another definition is provided by ASHRAE 55 standard [51] : “a subjective concept characterized by a sum of sensations, which produce a person's physical and mental wellbeing, condition for which a person would not prefer a different environment”. The second step consists in the determination of all the factors influencing the thermal comfort inside a vehicle. These factors can be divided in two classes: measurable factors and personal factors. The former include air temperature, air velocity, radiant temperature and relative humidity, while the latter include activity level and clothing insulation [52]. Therefore, it is evident that the most critical point is the connection between the objective analysis of the cabin thermal management and the subjective perceived thermal comfort. This correlation is realized by the choice of the most appropriate method to assess thermal comfort perceived by customers [53]. Taking into account these classes, a Predicted Mean Vote (PMV) index can be evaluated representing the average of the votes of a large group of people on the 7-point thermal sensation scale (Tab. 1), based on the heat balance of the human body [50]. PMV is a function of the metabolic rate, clothing insulation, moist air temperature, mean radiant temperature, moist air local velocity and moist air relative humidity and can be calculated by:

$$PMV = 0.303(e^{-0.036M+0.028})E_{st} \quad (1.1)$$

PMV value	Thermal sensation
-3	Cold
-2	Cool
-1	Slightly cool
0	Neutral
+1	Slightly warm
+2	Warm
+3	Hot

Table 1. 1: Fanger Thermal Sensation Scale [50].

Another index that can be the Predicted Percentage Dissatisfied (PPD) that establishes a quantitative prediction of the percentage of thermally dissatisfied people. PPD is a function of PMV as given below in Eq. 1.2 and depicted in the Fig. 1.8.

$$PPD = 100 - 95(e^{-(0.03353PMV^4+0.2179PMV^2)}) \quad (1.2)$$

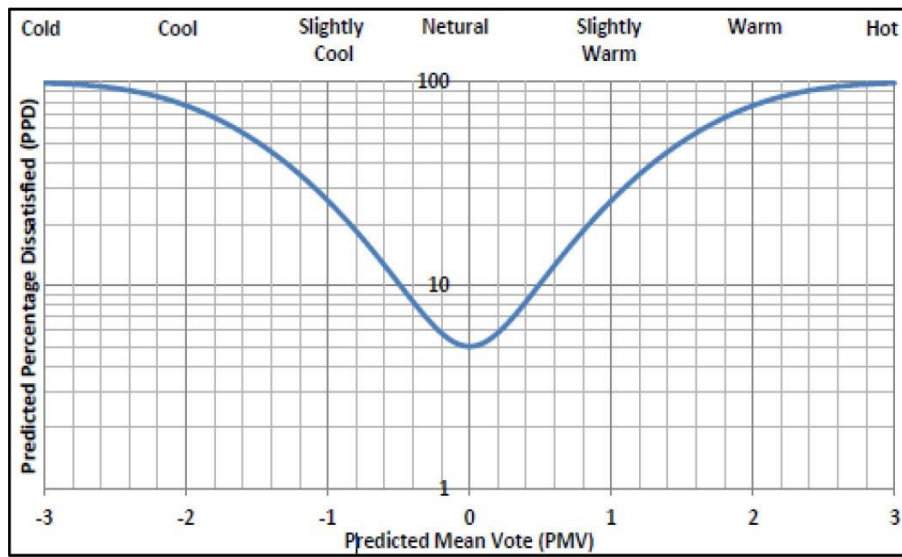


Fig. 1. 8: Predicted Percentage Dissatisfied (PPD) as a function of Predicted Mean Vote (PMV) [50].

The ASHRAE standard 55 [54] identifies comfort zones which are defined by a group of combination of different values for the relative humidity (RH) and the temperature inside the vehicle. These comfort zone depend on the season: in winter it is between 20°C with 90% RH and 24°C with 25% RH; in summer between 23°C with 90% RH and 27°C with 25% RH (Fig. 1.9).

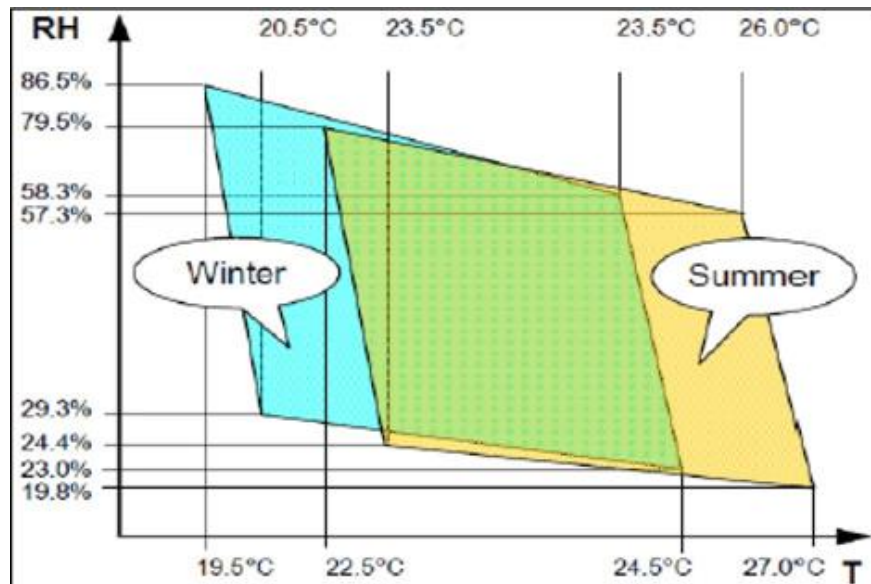


Fig. 1. 9: Thermal comfort zones defined by ASHRAE standard 55 [52].

Nowadays 1-D analysis is a useful tool to predict the system performance in the early stages of the vehicle HVAC systems development in a cheap and fast way. However the modelling of a cabin is a demanding operation in any 1D platform due to the high complexity of the cabin and numerous components involved.

In the library of the 1D model software Amesim it is proposed an example of model of a cabin vehicle which includes different materials, the heat transfer between cabin and environment through the frontal windshield, the side and rear windows, the roof and the side panels as shown in Fig. 1.10. The model also provides a post-processor tool to calculate the thermal comfort indexes defined above: PMV and PPD represented in Fig. 1.11.

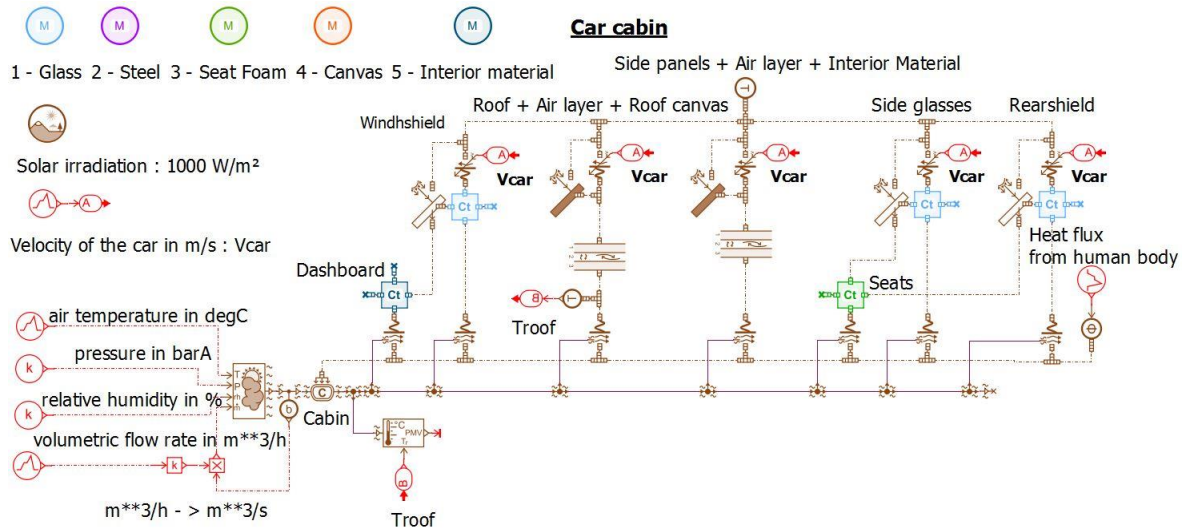


Fig. 1. 10: 1D model of the cabin of a vehicle built in Amesim.

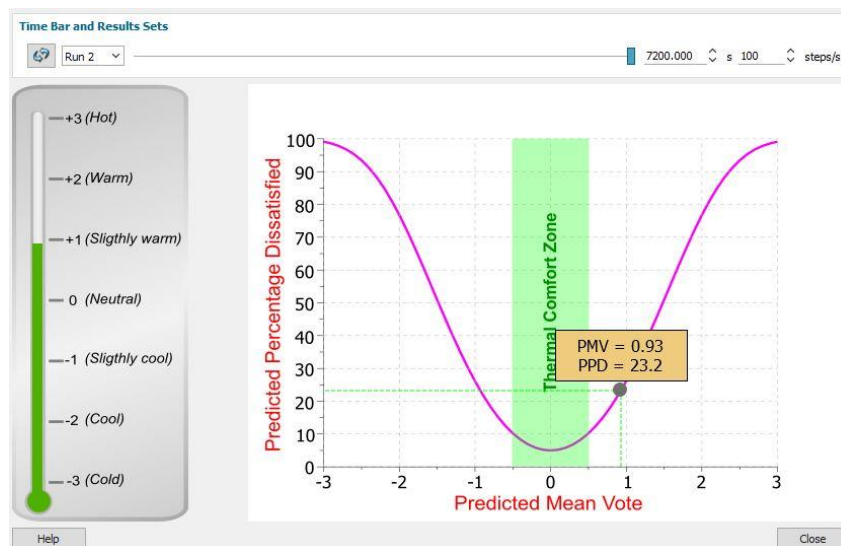


Fig. 1. 11: Post-Processor tool in Amesim for the calculation of the occupant thermal comfort indexes.

This software has been used, for instance, by G. Peri et al. [50] to model a vehicular cabin taken from a 3D CAD consisting of sheet metal parts, glass parts, insulation, instrumentation panel and seats. The cabin is compartmentalized into three different zones (driver zone, co-driver zone, passengers zone) and for each one of them the heat loads are individually modelled. All the three zones present a mixed connective load between them to describe the thermodynamic interactions happening

through the virtual division. Even if the model is using a connective load to link together the different volumes of the multi-zone, the lack of temperature distribution inside the vehicle is a huge limitation of 1D models, which consider the cabin as a lumped mass. The only way to overcome such a limit consists in modelling using a 3D CFD software, which though requires a huge modelling effort and CPU-time consumption. Recently different software companies, such as Amesim and KULI, have tried to combine the advantages of both the approaches integrating the two software. Sanket Shah [55] in his paper proposed a cool down simulation performed with three different approaches: 1D simulation, 3D CFD simulation, integration of the 1D simulation with the 3D CFD one. The purpose was to integrate the 3D Computational Fluid Dynamics software with the 1D thermal management software to achieve accurate prediction of temperature diffusion inside the cabin simultaneously reducing the modelling effort and CPU-time consumption.

The aim of research and analysis in this field is to investigate new ways and configurations to improve the system efficiency. In this article [56] a transient thermal model of a passenger car's cabin is developed to investigate the dynamic behavior of cabin thermal conditions. According to what has been discussed previously, the model has been simulated applying several alternative refrigerants and discussing their performance. In another paper instead is presented a method to estimate the heating cooling loads encountered in a vehicle cabin. By using the Heat Balance Method (HBM), the pattern of upcoming changes in the comfort level can be predicted in real-time in order to reduce overall power consumption while maintain driver thermal comfort [57]. In order to develop a reliable model, it is necessary to consider all the external factor that could affect the cabin temperature, as they are shown in Fig. 1.12. Among these the most important ones to affect cabin thermal balance are the solar radiation effect [58], the engine heat through the firewall, the heat flow through the windshield and side windows [59]. The aim of this SAE paper is to investigate different glass properties to reduce cabin heating under solar irradiance.

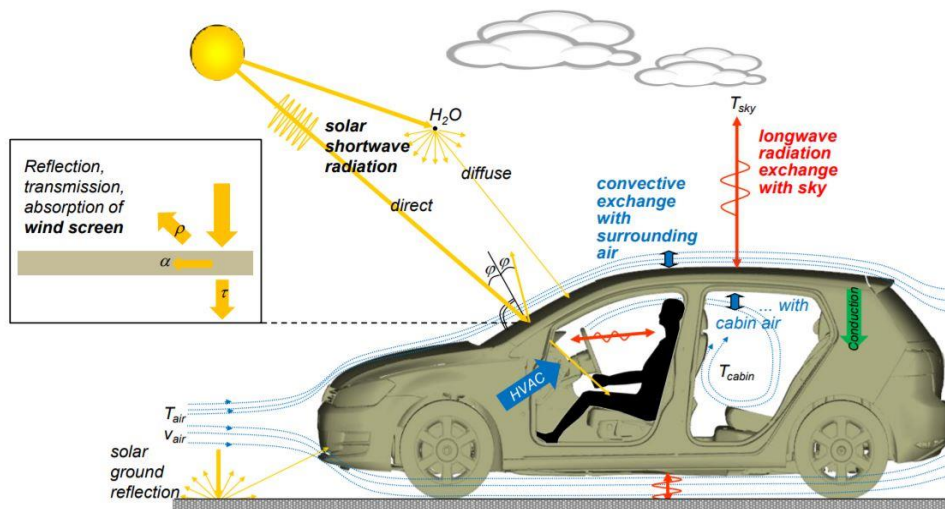


Fig. 1. 12: Factors that influence the cabin heat load [60].

Throughout the years, a significant amount of research has been conducted in order to improve the COP of heat pumps, focusing on the development of new components, technologies, configurations and refrigerants. This has been achieved considering the first law of thermodynamics with no considerations about the consequences of the second law. The first law is related to the conservation of energy without giving insights on the system performance degradation. While energy analysis is focused on system performance assessment, exergy analysis allows researchers to quantify the amount of energy losses in each component revealing itself as a powerful tool in the design, optimization, and performance evaluation of energy systems [61]–[63]. E. Bilgen and H. Takahashi [62] focused their research on the understanding of the irreversibilities due to heat transfer and friction in each component, which cause the system performance to degrade. Therefore, exergy analysis enables researchers to improve the real heat pump cycle minimizing the exergy destruction in each process; and, in order to do so, it is fundamental to understand its dependence on the system parameters. This was investigated by various researchers [61], [64] who realized that exergy is strongly affected by evaporating and condensing temperature, sub-cooling, compressor pressure and environmental temperature. The literature shows various samples of exergy analysis on different applications of the heat pump system generally related to cooling and heating system in building: ground source (geothermal) heat pump system [65], solar-assisted heat pumps [66] and many others presented in the review performed by J. U. Ahamed et al. [64]. In this context, performing an energy and exergy analysis on a heat pump system designed for the application to electric vehicle will bring new value in the literature. This analysis will be performed considering a heat pump system virtually modelled using the components of the refrigeration system of a Class A electric vehicle: the Fiat 500e. The results of this analysis will contribute to an understanding of the actual benefits of the heat pump system as a replacement for the commonly used PTC heater.

The study of the literature pointed out different aspects of the selected topic that need further exploration in order to deeply and clearly understand its nature. Some identified gaps in the literature are as follows:

- The sources studied do not propose or describe in detail specific approaches or methodologies to address the reversion of the cycle performed by a refrigeration system of a vehicle in order to develop a related heat pump system
- The sources do not implement the Second Law of Thermodynamics in the analysis of a heat pump system with the specific application to vehicle; hence, performing an exergy analysis is needed
- The design of a fully developed model of a car cabin environment exploiting new embedded CFD features to couple the thermal solution is performed in a 1D software, which limits the modeling as the heat transfer coefficient is constant throughout the cabin.

### 1.3 Objectives and Contributions

The purpose of this research is to develop 1D models to analyze different concepts of thermal management for the conditioning of the cabin of electric vehicles. This study can be divided in two different sections. On one hand, the development of a 1D model of a heat pump system starting from the components used in the current refrigeration system of the Fiat 500e, in order to investigate the potential of its application with the purpose to decrease the energy consumption of the system in cold climate conditions. The heat pump system has been chosen as viable replacement or support to the current heating system adopted: the positive temperature coefficient (PTC) heater. An energy and exergy analysis has been carried out to determine the individual components and overall system performance.

On the other hand, a new methodology of embedded CFD is investigated to develop a 1D model of the cabin of the Fiat 500e. This is a co-simulation where the thermal part is solved in a 1D environment, with the flow part solved in a 3D environment responsible of providing the calculation of the heat transfer coefficient. The Embedded CFD tool generates a coupling between Amesim and the 3D software STAR-CCM+ allowing the 1D model to correctly consider the thermodynamic interactions between different zones. This new approach will enrich the possibilities of 1D modelling giving the chance to evaluate a basic temperature distribution inside the cabin without requiring high computational resources and time consumption proper of an accurate CFD simulation.

In Chapter 2, a 1D model of the refrigeration system implemented in the previous version of the Fiat 500e was built using data provided by FCA. In Chapter 3, this model has been used to develop a heat pump 1D model performing the reverted thermodynamic cycle. This model was used to investigate the potential of the heat pump system as an alternative heating system with respect to the PTC heater in order to reduce energy consumption. An energy and exergy analysis was performed on a heat pump system applied to electric vehicles. In Chapter 4, a cabin model was developed following a new embedded CFD methodology, coupling the operations of a 1D software (Simcenter Amesim) and a 3D software (STAR-CCM+).

## Chapter 2 – Refrigeration cycle

### 2.1 Introduction

The first step to achieve the goals of this project is to gather data and information on the AC system adopted in the previous version of the Fiat 500e, whose function is to perform the cooling operations (the heating operations were fulfilled by a PTC heater). In this chapter the process of retrieving the data and building the refrigerant loop model of the vehicle using the one-dimensional software Amesim is described. In order to do so, at first the cycle performed and the components needed by the system are described. Then the modelling process followed to achieve the final result is defined. This process can be categorized into two macro-sections which can be divided again in two different steps hence, a total of four consequent phases. These phases are described in Fig. 2.1. The first division is between an initial individual modelling of each component and the construction of a complete system level model. The aim of the first step is to obtain the best match between the virtual components designed in Amesim and the real ones. In order to achieve such goal, the user has to go through two different stages: an initial geometrical parametrization followed by a thermodynamic performance calibration. Once every component has reached the best achievable (and reasonable) match with its real counterpart, they can be assembled together to develop a complete system level model. The fundamental outcome of this operation is to define the optimal value of the virtual coolant charge, which will be properly defined later in the chapter. Finally, the entire model will be subjected to a validation through the comparison of its simulation results with actual bench test data. This will prove its precision and reliability allowing engineers to use the model in the future. The information regarding the characteristics and the mathematical model of the Amesim components are provided by the libraries available in the built-in software.

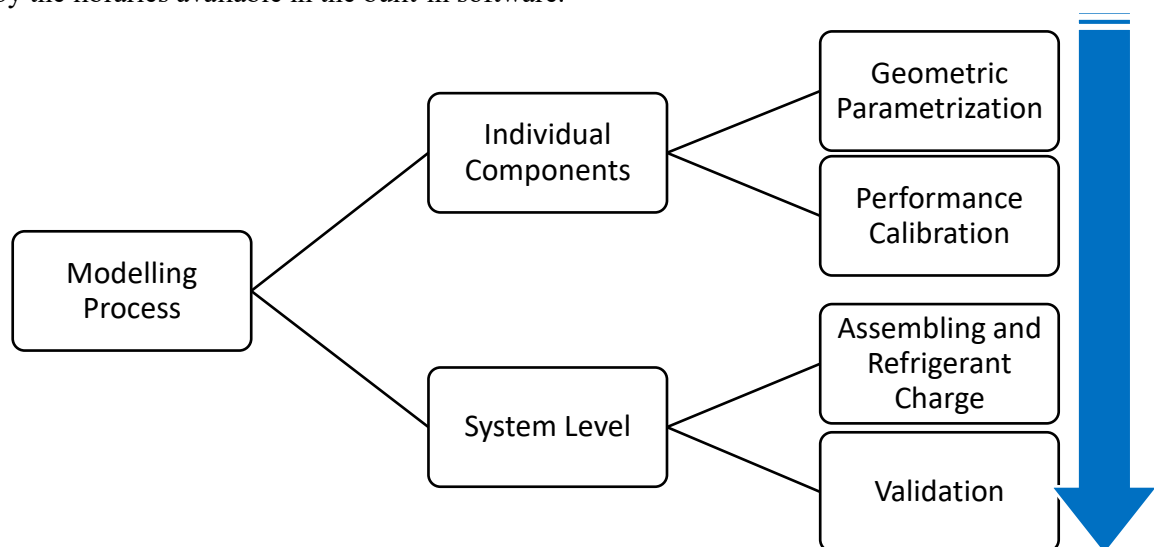


Fig. 2. 1: Phases of the modelling process followed to build the AC system for the refrigeration loop.

## 2.2 Vapour-compression cycle – cooling loop

The purpose of a heating, ventilation and air conditioning (HVAC) system can be identified defining three different main functions: temperature control, performed by adding or removing heat from the vehicle cabin; humidity control, obtained through the dehumidification or drying of the air; and air circulation control, achieved by recirculating and replacing stale air [19].

The AC system considered is in charge of the cool down of the vehicle cabin in hot climate conditions and it uses a fluid known as refrigerant (in this case R134a) to operate. An illustrative cycle is represented in two different figures: the temperature-entropy (Fig. 2.2) and the pressure-enthalpy diagram (Fig. 2.3).

This system is composed of four fundamental components (i.e. compressor, condenser, thermostatic expansion valve and evaporator), each performing a different thermodynamic transformation of the working fluid. The thermodynamic transformations are as follows: compression, ideally adiabatic and isentropic (real process shown in Figs. 2.2 and 2.3, segments 1-2 or 1'-2'); heat transfer at constant pressure from the refrigerant towards the external air (Figs. 2.2 and 2.3, segments 2-3 or 2'-3'); expansion, ideally adiabatic and isentropic (real process shown in Figs. 2.2 and 2.3, segments 3-4 or 3'-4'); and a second heat transfer at constant pressure with the air flowing inside the cabin towards the refrigerant (Figs. 2.2 and 2.3, segments 4-1 or 4'-1'). During both the isobar processes, the refrigerant goes through a phase change and so three different stages can be identified as follows. Firstly, the refrigerant gas is cooled to its saturation point in the condenser where sensible heat is removed as the temperature is decreasing during the process. Secondly, the gas is condensed in liquid refrigerant, the temperature remaining constant at the saturation point and latent heat being exchanged. Finally, the liquid refrigerant can go through a second cool down, also called subcooling (Figs. 2.2 and 2.3, segment 3-3'), which ensures that all the refrigerant has been condensed. Similarly, in the evaporator the liquid refrigerant is initially heated until the saturation point at which point the temperature remains constant while the refrigerant evaporates. Once this operation is completed, the refrigerant gas temperature is further increased in a process called superheating (Figs. 2.2 and 2.3, segment 1-1').

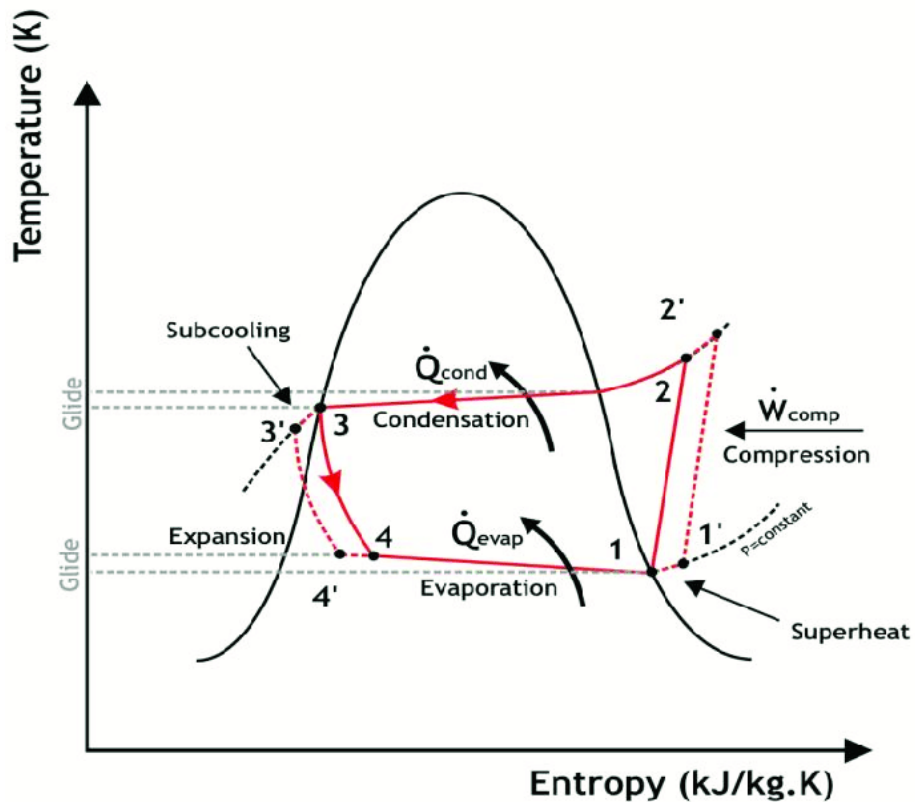


Fig. 2. 2: T-s diagram of a general vapour-compression refrigeration cycle [67].

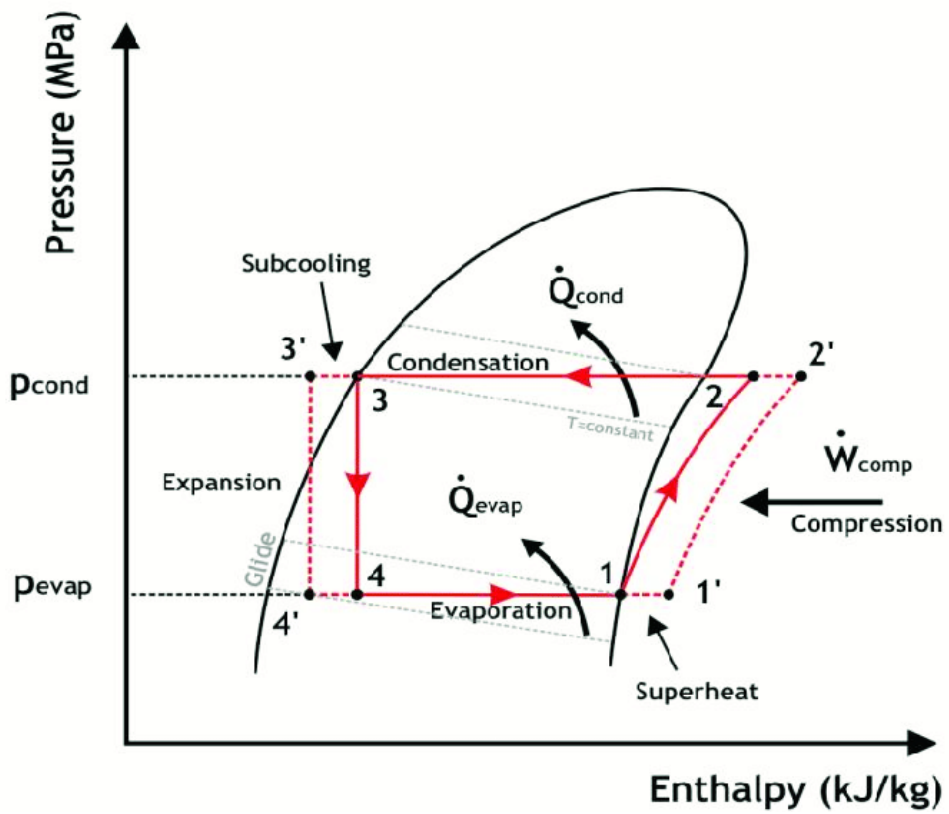


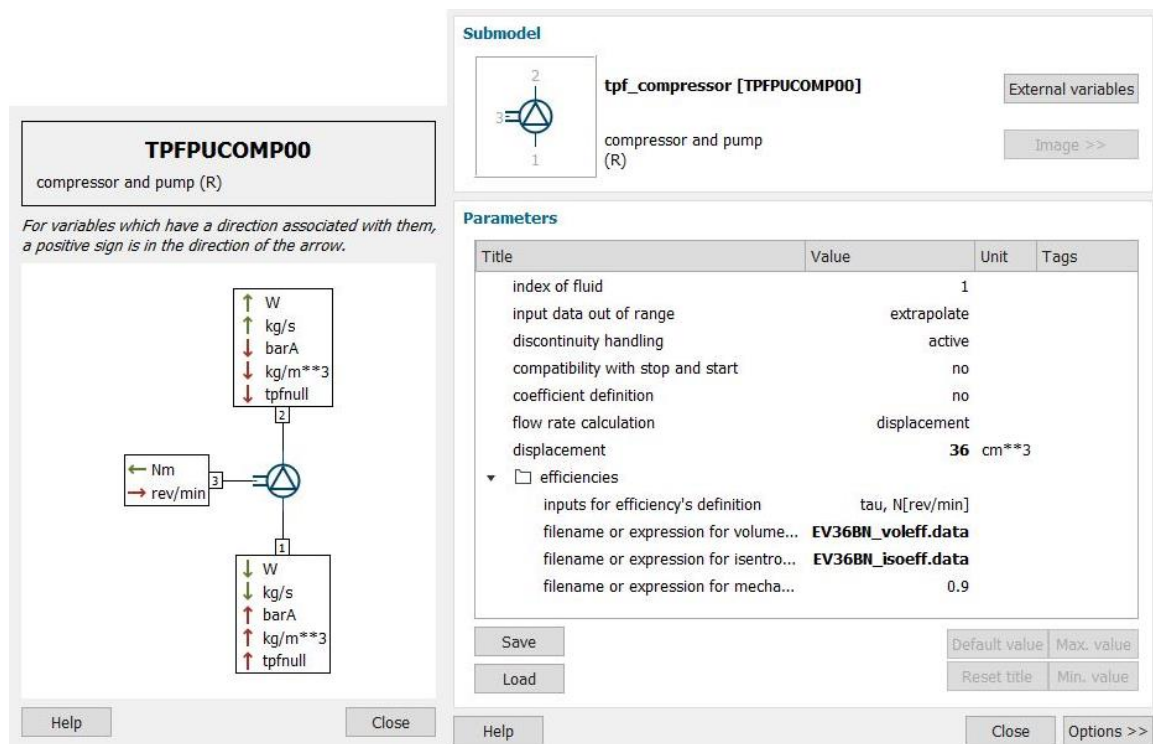
Fig. 2. 3: p-h diagram of a general vapour-compression refrigeration cycle [67].

## 2.3 Components modelling

According to the procedure described in the introduction, the modelling process starts with the geometrical parametrization of each component. Once this first step has been completed, the dimensions and all the other geometric characteristics of the virtual components will perfectly match the real ones. This geometrical correspondence between modelled and actual element is not sufficient to ensure an equivalent relation in their performance, because there is not a strict and univocal correlation between geometry and thermodynamic behavior. Therefore, it is essential to calibrate the equations in charge of the thermodynamic computation through the use of experimental data. The procedure used to parametrize and calibrate each component is unique and strictly related to its characteristics. The following paragraphs describe the approach used for each component.

### 2.3.1 Compressor

The compressor adopted in the system is a small electric compressor with a high-revolutions per minute (RPM) regime. Its volume displacement is  $36 \text{ cm}^3$  and its idle angular speed is 7600 RPM. To model this component the submodel “tpf\_compressor\_tpf\_pump [TPFPUCOMP00]” has been used (Fig. 2.4), which can be characterized by volumetric, isentropic and mechanical efficiencies definition for mass flow rate and enthalpy loss.



The screenshot displays the configuration window for the submodel **TPFPUCOMP00**, which is a compressor and pump (R). The window is divided into several sections:

- Submodel:** Shows the submodel icon and name **tpf\_compressor [TPFPUCOMP00]**. It includes buttons for **External variables** and **Image >>**.
- Parameters:** A table listing various parameters and their values.
- External Variables:** A table listing variables with their values and units.

Title	Value	Unit	Tags
index of fluid		1	
input data out of range		extrapolate	
discontinuity handling		active	
compatibility with stop and start		no	
coefficient definition		no	
flow rate calculation		displacement	
displacement		<b>36</b> $\text{cm}^3$	
<input type="checkbox"/> efficiencies			
<input type="checkbox"/> inputs for efficiency's definition		tau, N[rev/min]	
filename or expression for volume...		<b>EV36BN_voleff.data</b>	
filename or expression for isentro...		<b>EV36BN_iseoff.data</b>	
filename or expression for mecha...		0.9	

Fig. 2. 4: Element adopted for the modelling of the compressor; list of external variables and parametrization.

These efficiencies can be supplied as:

- A constant, if they do not depend on any variable.
- An expression (2D, 3D, 4D table) of the compression ratio  $\tau$  [null] and the rotary speed of the machine  $N$  [rev/min],  $X1$  and  $X2$  which are optional user defined inputs.

Performances of the compressor characterizing the isentropic and volumetric efficiencies as a function of the compression ratio and of the rotary speed, while assuming the mechanical efficiency to be 0.9, have been determined using FCA data. This is shown in Fig. 2.5 and Fig. 2.6, respectively. In this submodel the volumetric efficiency is used to compute the outlet mass flow rate as shown in Eq. 2.1:

$$dm_2 = \eta_v \cdot \rho_1 \cdot N \cdot disp \quad (2.1)$$

where  $\eta_v$  is the volumetric efficiency;  $\rho_1$  is the suction density;  $N$  is the rotary speed of the compressor and  $disp$  is the compressor displacement. On the other hand the enthalpy increase through the compressor is calculated from the expression of the isentropic efficiency, shown in Eq. 2.2:

$$\eta_{is} = \frac{h_{2,i} - h_1}{h_2 - h_1} \quad (2.2)$$

where  $\eta_{is}$  is the isentropic efficiency;  $h_{2,i}$  is the isentropic outlet specific enthalpy;  $h_1$  is the inlet specific enthalpy;  $h_2$  is the outlet specific enthalpy.

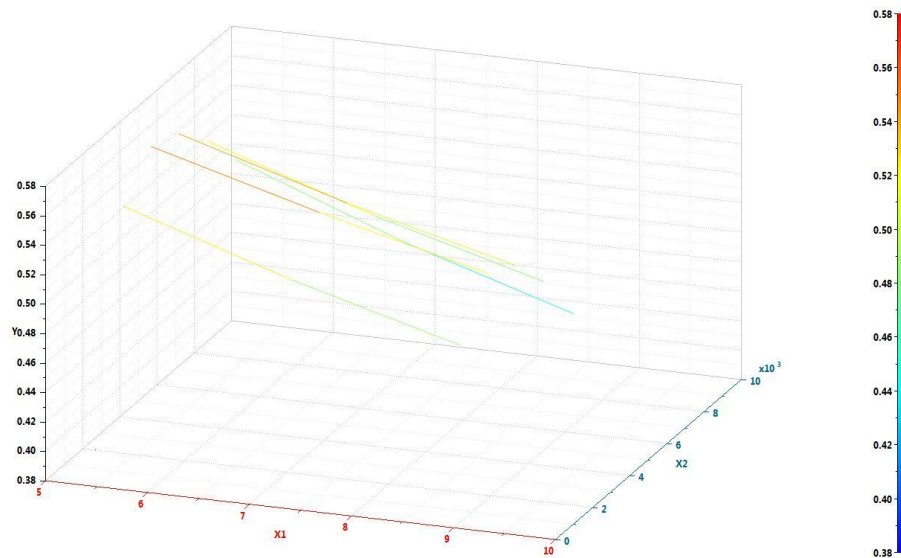


Fig. 2. 5: Isentropic efficiency ( $Y$ ) defined as a function of the compression ratio ( $X1$ ) [null] and the angular speed ( $X2$ ) [RPM].

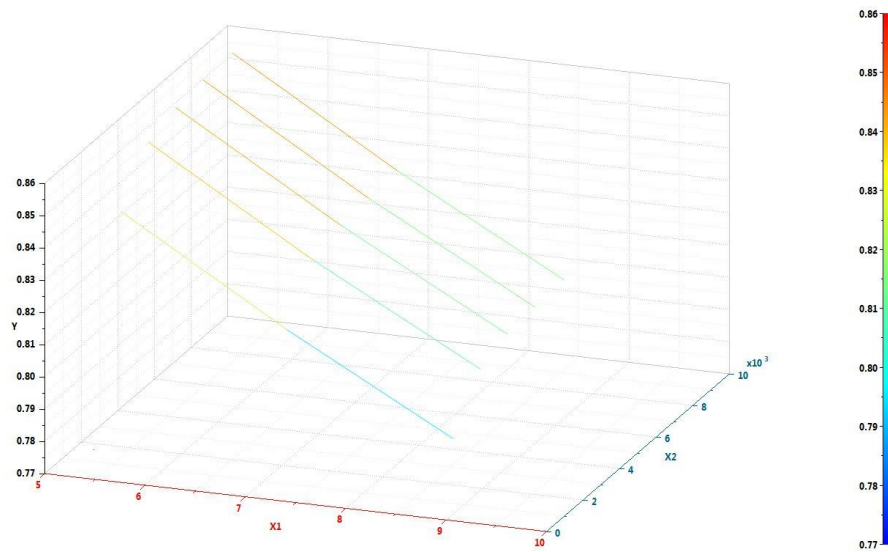


Fig. 2. 6: Volumetric efficiency ( $Y$ ) defined as a function of the compression ratio ( $X1$ ) [null] and the angular speed ( $X2$ ) [RPM].

### 2.3.2 Condenser

The modelling of the heat exchanger is a more complex step, since after the accurate geometrical parametrization it is necessary to calibrate the thermodynamic performances on the air side, optimizing the coefficients of the Nusselt correlation responsible of the calculation of the heat transfer.

The condenser used in the system is a four pass, one row microchannel tube and fin heat exchanger of dimensions 620x313.25 mm with an integrated receiver. This component has been represented with the submodel “ACMCTF0” which allows the user to build the complete heat exchanger (Fig. 2.7) using different pass elements to achieve the correct configuration. The parametrization of the condenser is performed at two levels: a set of global data defined in “ac\_mctf\_global\_data [ACMCTF0]”, completed by a second group of specific data for each pass element (Fig. 2.8). The set of global data required to geometrically parametrize the condenser are: finned tube width, finned tube depth, collector cross-sectional area, refrigerant side cross-sectional per tube, refrigerant side hydraulic diameter, fin pitch, fin thickness, fin length, tube periodicity, external tube height.

This parametrization is completed in the pass elements where it is necessary to define the number of tubes for each pass.

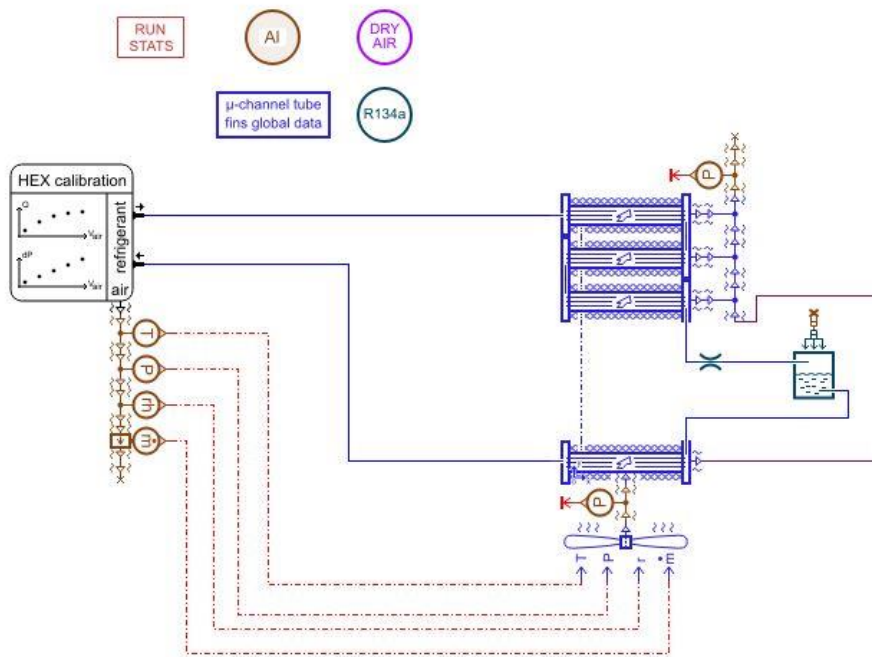


Fig. 2. 7: Model of the condenser connected with the heat exchanger (HEX) calibration tool.

### ACMCTREF1

reference part of a micro channel tube and fins heat exchanger (configuration 1)

*For variables which have a direction associated with them, a positive sign is in the direction of the arrow.*

Variables shown in the diagram include:  $\text{kg/s}$ ,  $\text{g/kg}$ ,  $\text{barA}$ ,  $\text{degC}$ ,  $\text{m}$ ,  $\text{null}$ ,  $\text{W}$ ,  $\text{kg/s}$ ,  $\text{barA}$ ,  $\text{kg/m**3}$ ,  $\text{tpfnull}$ ,  $\text{kg/s}$ ,  $\text{barA}$ ,  $\text{degC}$ .

#### Submodel

**ac\_mctf\_ref1 [ACMCTREF1]** External variables

reference part of a micro channel tube and fins heat exchanger (configuration 1) Image >>

#### Parameters

Title	Value	Unit	Tags
index of fluid			1
solid type index			1
index of micro channel tube and fi...			1
number of tubes			3
number of cells			3 cells
acceleration pressure drop calcula...			no
moist air temperature definition			input signal
type of initialization			<b>pressure and temperature</b>
pressure			<b>Ini_P_C</b> barA
temperature			<b>Ini_T_C</b> degC
frictional pressure drop gain of th...			1 null
filename for air mass flow rate pr...	.../Amesim/libac/data/profile.data		

Buttons: Save, Load, Default value, Max. value, Reset title, Min. value, Help, Close, Options >>

Fig. 2. 8: Element adopted for the modelling of each pass element of the condenser; list of external variables and parametrization (the pass shown is the fourth).

The function of the integrated receiver is to gather and filter the working fluid allowing only the refrigerant in liquid phase to proceed. Ideally, this harvest operation is adiabatic and the refrigerant is not exchanging any heat with the environment during the process. On this purpose, this component has been modelled using the element “tpf\_st\_chamber [TPFSCH00]” (Fig. 2.9). This submodel is a

stratified chamber with an imposed heat flow rate (in the considered case null heat flow rate), in which three variables are observed independently of the state of the fluid: chamber temperature, liquid volume percentage and refrigerant charge. The mass and energy conservation equation are solved receiving as input the enthalpy and mass flow rates at ports 1 and 3 and an external heat flow rate at port 2. Since in this case the external heat flow rate is assumed to be null, the mass and enthalpy flow rates should remain constant. The pressure is considered to be homogeneous in the entire volume, while the densities of the liquid and vapor phases of the refrigerant are assumed homogeneous in their respective volumes.

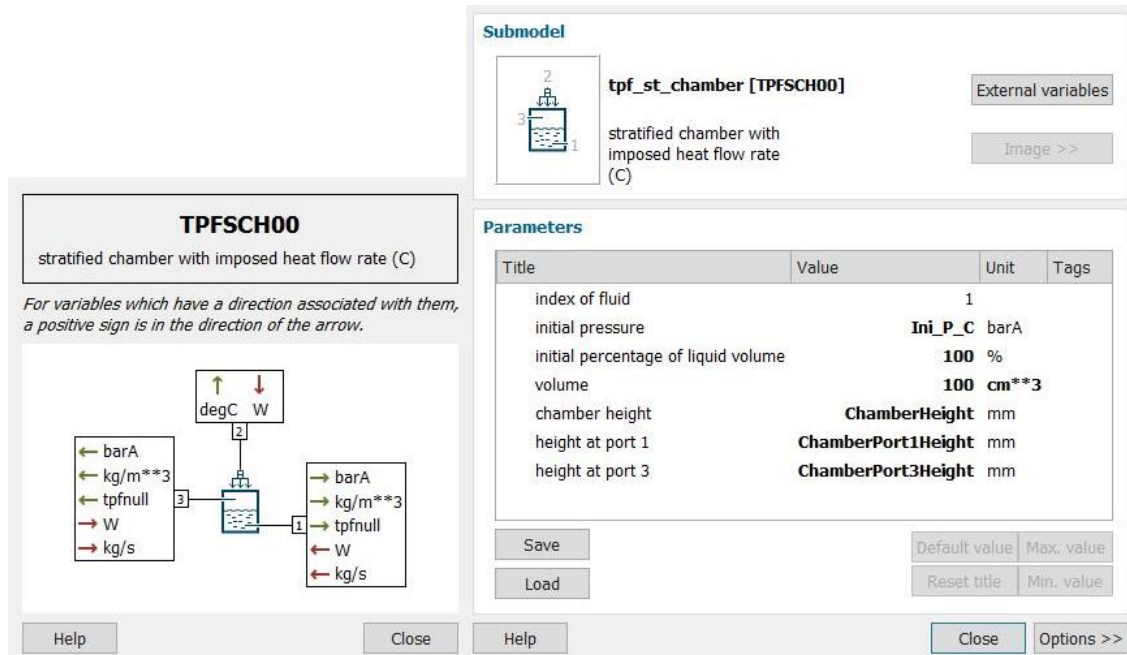


Fig. 2. 9: Element adopted for the modelling of the integrated receiver; list of external variables and parametrization.

Furthermore, in the micro channel tube and fins heat exchanger global data submodel it is also fundamental to define the correlations characterizing the pressure drop in the refrigerant side and the heat transfer on both refrigerant and air side. The total static pressure gradient along the channel tube can be characterized by the choice of a frictional pressure loss gain ( $k_{dp}$ ) and can be expressed as shown in Eq. 2.3 as a sum of respectively a friction pressure drop term, an acceleration pressure drop term (due to changes in the fluid's density) and a gravity contribution term:

$$\frac{dP}{dz} = \left(\frac{dP}{dz}\right)_F + \left(\frac{dP}{dz}\right)_a + \left(\frac{dP}{dz}\right)_z \quad (2.3)$$

Where:

$$\left(\frac{dP}{dz}\right)_F = k_{dp} \cdot \left( \left(\frac{dP}{dz}\right)_{F_{reg}} + \left(\frac{dP}{dz}\right)_{F_{sing}} \right) \quad (2.4)$$

On the other hand, in order to regulate the heat exchange it is necessary to define a thermodynamic correlation for the Nusselt number for both the fluids, shown in Eq. 2.5. While on the refrigerant side the simplicity of the geometry of the case considered, a tube, allows to use a well-known correlation (Gnielinski) and a heat transfer gain (kHeat), on the air side it is fundamental to develop a correlation in the form (2.5), which fits the specific situation considered.

$$Nu = NuA * Re^{NuB} * Pr^{NuC} \quad (2.5)$$

In order to achieve an optimal match between the thermodynamic performance of the virtual condenser and the real one, experimental data are necessary. This match is defined in terms of heat rejection and refrigerant side pressure drop performed by the heat exchanger, which are coupled phenomena as the pressure drop modifies the saturation pressure of the refrigerant affecting the heat rejection, which drives the state of the fluid affecting the friction occurring. The calibration tool allows the user to run an iterative optimization process to find the parameters that best match experimental data.

The calibration tool acts on the values of NuA, NuB and NuC of the correlation, on the internal heat transfer gain (kHeat) and on the pressure drop gain (kdP). As we can see in Fig. 2.10, the calibration tool performs an optimization batch run of these parameters using as input of the model the experimental test data provided by the supplier (air velocity, temperature and relative humidity; refrigerant inlet temperature, mass flow rate and inlet pressure) and minimizing the deviation between the simulation results and the experimental ones. The optimization process adopted has been created by Amesim and it relies on built-in mathematical models to predict the moment of external heat exchange saturation as the outlet temperature of the air cannot overcome the wall temperature of the condenser. The tolerance for the deviation on the heat rejection is very strict with acceptable values below 4-5%. On the other hand the tolerance on the refrigerant pressure drop is more relaxed, as shown in Fig. 2.10.

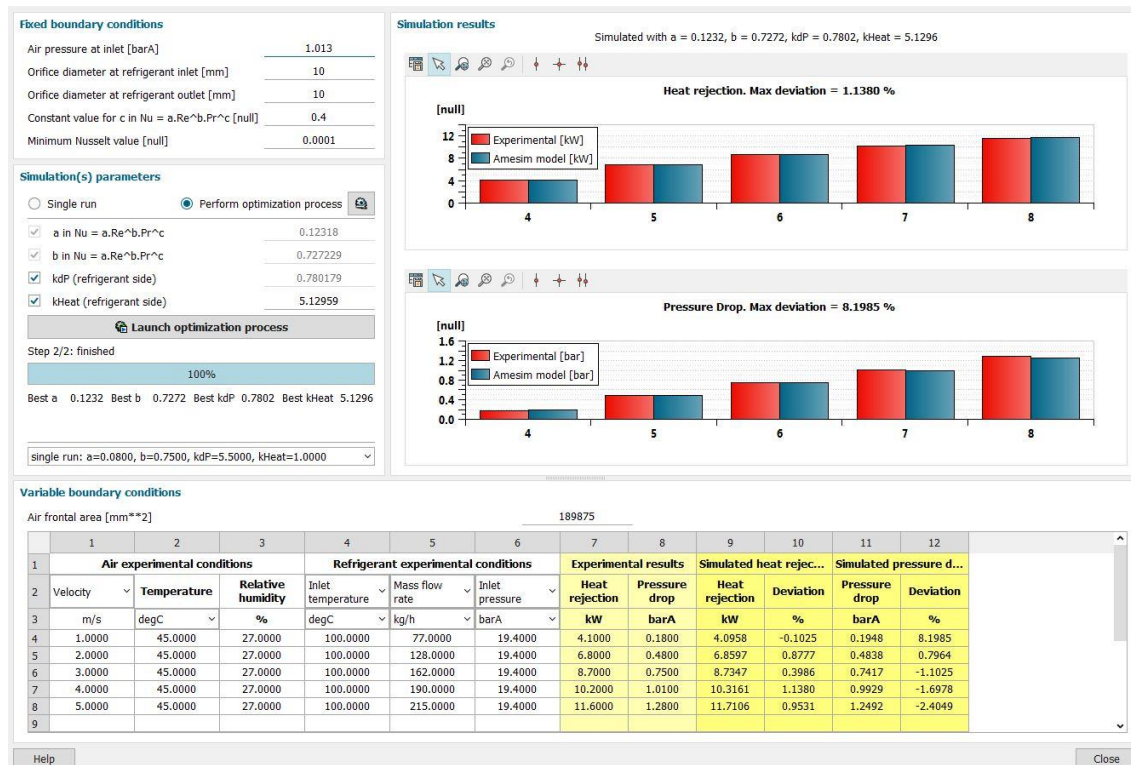
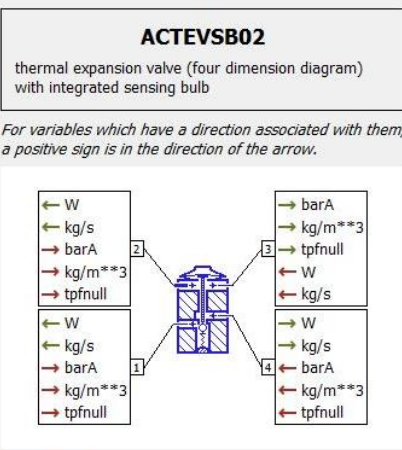


Fig. 2. 10: Calibration of the thermodynamic performances of the condenser using the heat exchanger calibration tool provided by Amesim.

### 2.3.3 Thermostatic expansion valve (TXV)

The thermostatic expansion valve is a metering and pressure regulating device used to control the mass flow rate of refrigerant going through the evaporator in order to maintain a constant superheat at its end. The submodel used is “ac\_txv [ACTEVSB02]” which is a TXV with integrated thermal sensing bulb that controls the refrigerant flow regulating the valve lift due to a force balance acting on a rod via a diaphragm. In fact, as it can be observed in Fig. 2.11 the component receives the refrigerant coming from the condenser on port 4 and releases it from port 1, while the integrated sensing bulb receives the refrigerant from the evaporator at port 2 delivering it towards the compressor at port 3. Between port 1 and port 4, a variable resistive element is considered and its operations depend on the force balance acting on the rod.



**ACTEVS02**  
thermal expansion valve (four dimension diagram) with integrated sensing bulb

*For variables which have a direction associated with them, a positive sign is in the direction of the arrow.*

**Submodel**



**ac\_t xv [ACTEVS02]** External variables

thermal expansion valve (four dimension diagram) with integrated sensing bulb Image >>

**Parameters**

Title	Value	Unit	Tags
bulb temperature	43.33	degC	
index of fluid	1		
maximum valve lift	0.8	mm	
reference high pressure third quadrant	<b>PHigh</b>	barA	
reference low pressure in third quadrant	<b>Plow</b>	barA	
reference subcooling in third quadrant	5	degC	
pressure offset at 0 degC	0	barA	
time constant	5	s	
first quadrant	AMETable		
interpolation type	linear		
linear data out of range mode	...apolation		
discontinuity handling	active		
filename of first quadrant curve for valve opening ...	...nt.data		
second quadrant	AMETable		
interpolation type	linear		
linear data out of range mode	...apolation		
discontinuity handling	active		
filename of second quadrant curve for evaporator...	...nt.data		
third quadrant	AMETable		
interpolation type	linear		
linear data out of range mode	...apolation		
discontinuity handling	active		
filename of third quadrant curve for mass flow rat...	...nt.data		

Fig. 2. 11: Element adopted for the modelling of the thermostatic expansion valve; list of external variables and parametrization.

Normally, the TXV characteristic curves are described in a 4-quadrant diagram (Fig. 2.12). The four quadrants are:

1. The valve opening curve and the refrigerant saturation curve as a function of thermal sensing bulb fluid (evaporator outlet temperature and pressure),
2. The evaporator outlet pressure as a function of the valve lift for different constant temperature values,
3. The evolution of the reference mass as a function of the valve lift,
4. The evolution of the reference mass flow rate as a function of the evaporator outlet temperature.

In both the third and fourth quadrants the reference mass flow rate is limited to a maximum value and it is necessary to set the reference value for the high pressure (at the TXV inlet) and the low pressure (at the TXV outlet). Furthermore, since these curves depend on each other, the fourth quadrant can be deduced from the first and third quadrant, as can be seen in Fig. 2.11.

28

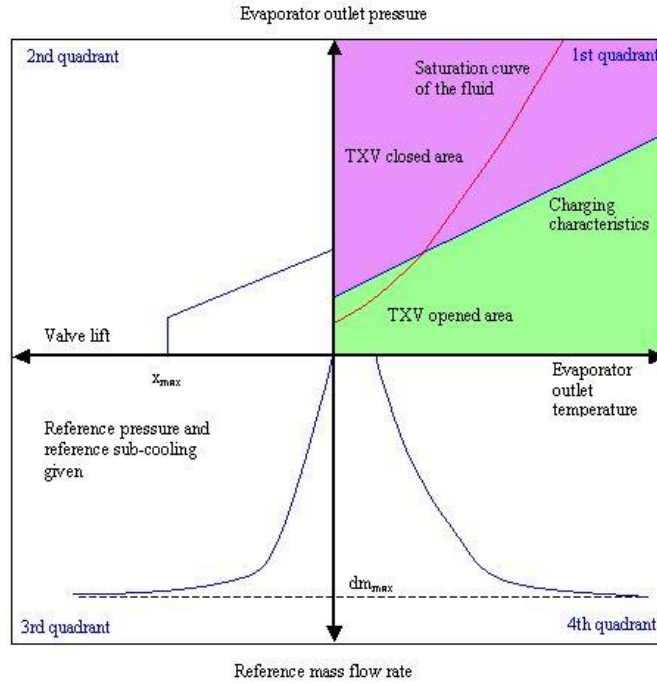


Fig. 2. 12: A four-dimension diagram characterizing the thermostatic expansion valve.

The valve lift depends only on the pressure difference between the valve opening pressure and the evaporator outlet pressure at the same temperature, according to Eq. 2.6:

$$P_{op}(T_{bulb_{ref}}) - P_{ev}(T_{bulb_{ref}}) = p_{op} - p_{ev} \quad (2.6)$$

Where  $P_{op}(T_{bulb_{ref}})$  and  $P_{ev}(T_{bulb_{ref}})$  are respectively the valve opening pressure and the evaporator outlet pressure at bulb temperature, while  $p_{op}$  and  $p_{ev}$  are respectively the current valve opening pressure and the evaporator outlet pressure.

### 2.3.4 Evaporator

As the condenser, the evaporator is a microchannel tube and fin heat exchanger but in this case it is a 2 rows 2 passes configuration. According to this, the modelling and parametrization of this component will be different with respect to the one of the condenser, while the calibration process of the thermodynamic performances will be accomplished using the same tool and following the same procedures. The submodel adopted is “ac\_dual\_core [ACDCHX0]” which represents a dual core heat exchanger based on tube and fin geometry (Fig. 2.13). However, the structure of this heat exchanger is not modelled by using additional elements arranged in the desired configuration but by using a single compact component, composed of two cores (i.e. front and rear). Therefore, in this situation the first step of the parametrization is to define the number of passes for each core and the

number of tubes for each pass. In order to have consistency in the component's dimensions it is important that the sum of the number of tubes used in the front core is equal to the rear core. When the configuration has been set, the characterization of the component can be completed following the exact same procedure explained in paragraph 2.3.2 regarding the geometrical parametrization and the thermodynamic calibration of pressure drop and heat rejection.

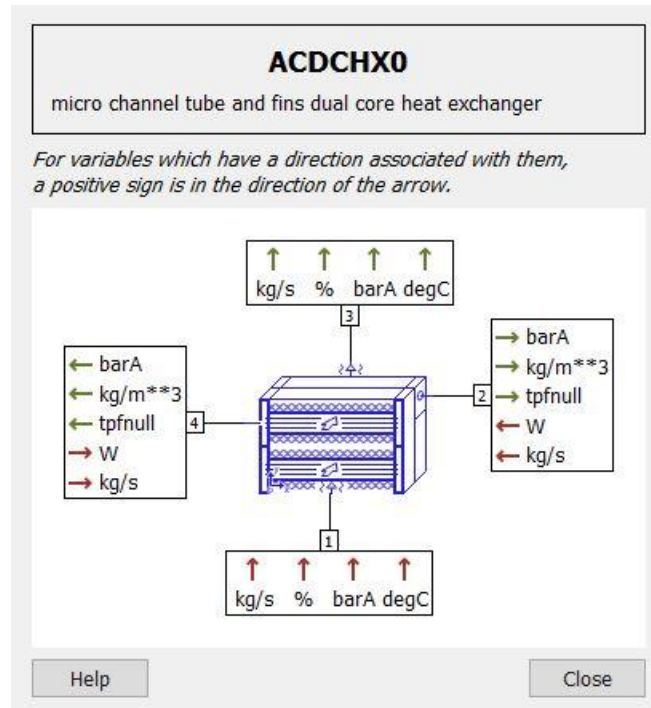


Fig. 2. 13: Element adopted for the modelling of the evaporator.

The calibration of the heat transfer gain, pressure drop gain and of the parameters of the Nusselt correlation proceeds as explained before in the condenser paragraph, minimizing the deviation on the calculation of the heat rejection of the heat exchanger and of the pressure drop on the refrigerant side. However, in this case a different set of experimental data has been used as input: air mass flow rate instead of velocity; inlet specific enthalpy instead of inlet temperature and finally outlet pressure instead of inlet pressure. The choice of the input is determined by the availability of experimental data, but selecting the appropriate and non-redundant combination of data will guarantee a unique definition of the boundary conditions.

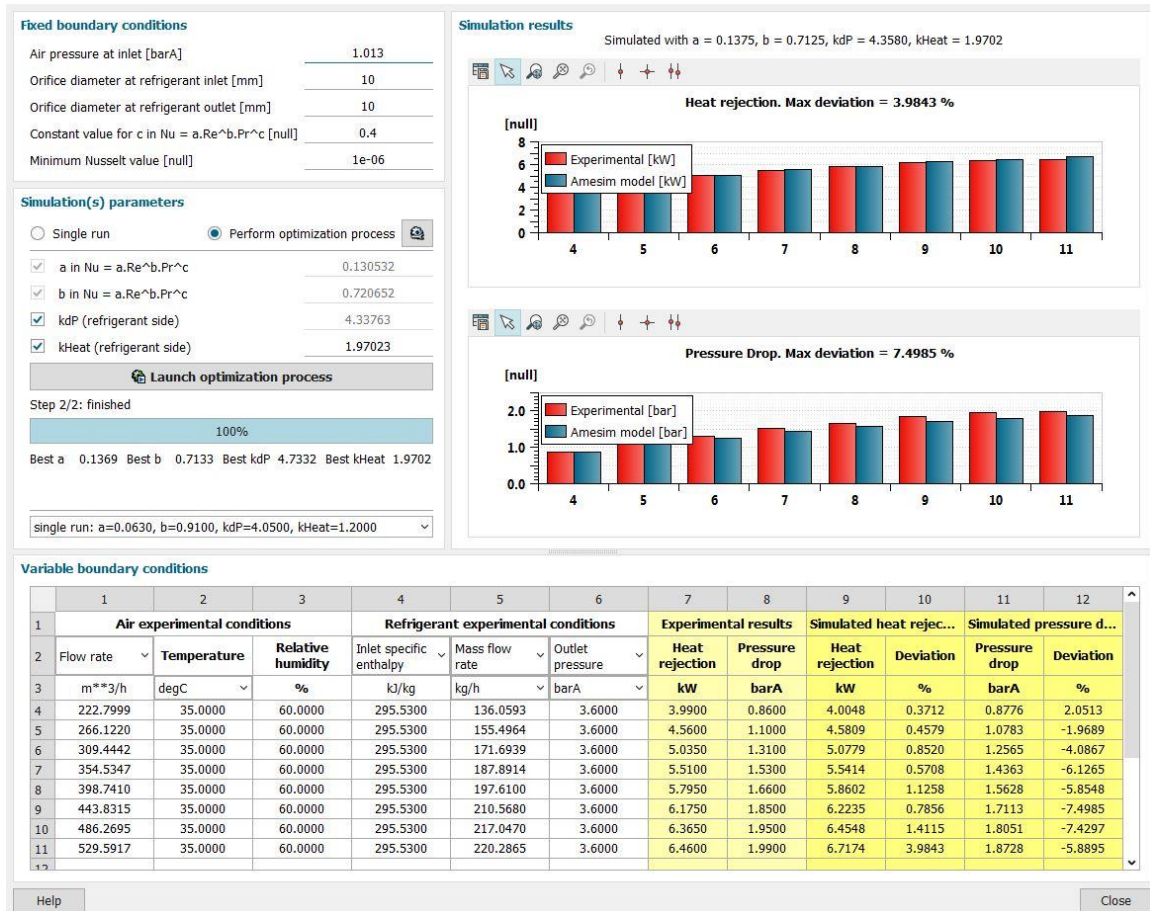


Fig. 2. 14: Calibration of the thermodynamic performances of the evaporator using the heat exchanger calibration tool provided by Amesim.

## 2.4 System level model

The refrigerant loop that performs the cooling operations is an assembly of the modeled and characterized components presented.

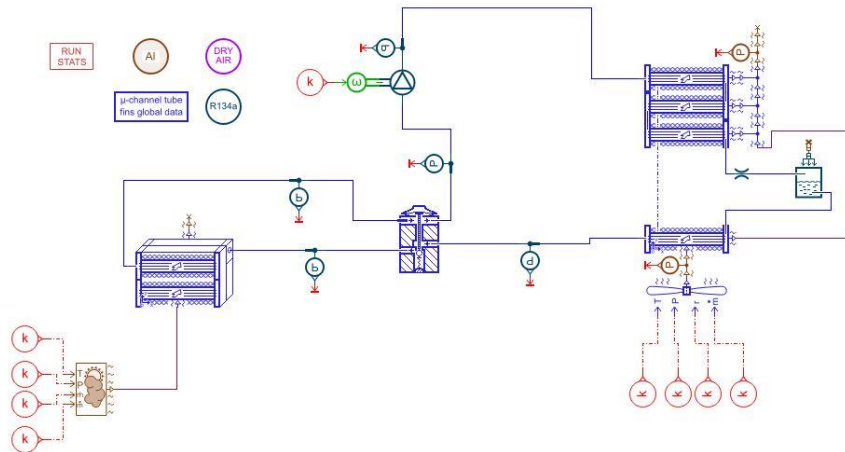


Fig. 2. 15: Assembled model of the AC system responsible for cooling operations.

As it is shown in Fig. 2.15, the refrigerant used is R134a. All the components have been connected in series directly without the use of pipes, because their path and dimensions are still unknown. Therefore, all the interactions of the fluid happening between one component and the other are assumed to be negligible and this consideration will be of great importance while calculating the refrigerant charge needed by the system to operate. Once the system has been assembled, it is possible to identify its inputs:

- **Compressor RPM:**

The compressor used is electric so it is not belt driven as many other compressors in the market. This means that its angular speed is not directly connected with the engine RPM but can be controlled electronically. During idle the rotary speed of the compressor is usually 7600 RPM, while instead it shifts to a maximum of 8400 RPM during motion.

- **Thermophysical properties of air entering the condenser:**

The condenser is placed in the front of the car with the battery and the powertrain radiators, so the thermophysical properties of air entering it are the environment air. The input parameters used to define air at the condenser inlet are temperature, pressure, relative humidity and mass flow rate.

- **Thermophysical properties of air entering the evaporator:**

The evaporator is instead placed after the blower in the ducts to deliver air inside the cabin. It requires the same input data as the condenser however, different situations exist: the entire flow of air is composed of outside air without any recirculation from the cabin; the external ports are shut off and all the air flowing through the evaporator has been recirculated; a mixed situation in which fresh air and recirculated air contribute to the mass flow rate with a specific percentage.

## 2.5 Virtual refrigerant charge calculation

In order to complete the model it is necessary to compute the optimal refrigerant charge needed by the system. The procedure followed to achieve such result is described as follows:

- The model inputs have been filled with the data shown in Table 2.1.
- 19 simulations have been run with different refrigerant charge value starting from 3 oz to 12 oz with a step interval of 0.5 oz.
- For each simulation, the value of the subcooling at the end of the condenser has been collected.
- A graph has been built showing the behavior of the data collected (subcooling) with respect to the refrigerant charge (Fig. 2.16).
- A plateau has been identified on the graph between 6.5 and 9 oz of refrigerant charge.

- Since all the pipes have been neglected in the model, a virtual refrigerant charge which is defined by the charge corresponding to the 75% of the plateau, shown in red in Fig. 2.16, was calculated using Eq. 2.7.

$$\begin{aligned} \text{virtual refrigerant charge} \\ = \text{charge}_{\text{plt},\text{min}} + 0.75 * (\text{charge}_{\text{plt},\text{max}} - \text{charge}_{\text{plt},\text{min}}) \end{aligned} \quad (2.7)$$

Following these procedures the value obtained for the optimal virtual refrigerant charge is 8.375 oz. This is a lower value with respect the actual charge used in the vehicle, because the plumbing has been neglected in the modelling.

<i>INPUT PARAMETER</i>		<i>VALUE</i>
<i>Compressor</i>	RPM	8400
<i>Condenser</i>	Temperature	43 °C
	Pressure	1.01325 bar
	Relative Humidity	19%
	Mass Flow Rate	0.287 kg/s
<i>Evaporator</i>	Temperature	43 °C
	Pressure	1.01325 bar
	Relative Humidity	19%
	Mass Flow Rate	0.103 kg/s

Table 2. 1: Input parameters for the calculation of the optimal virtual refrigerant charge.

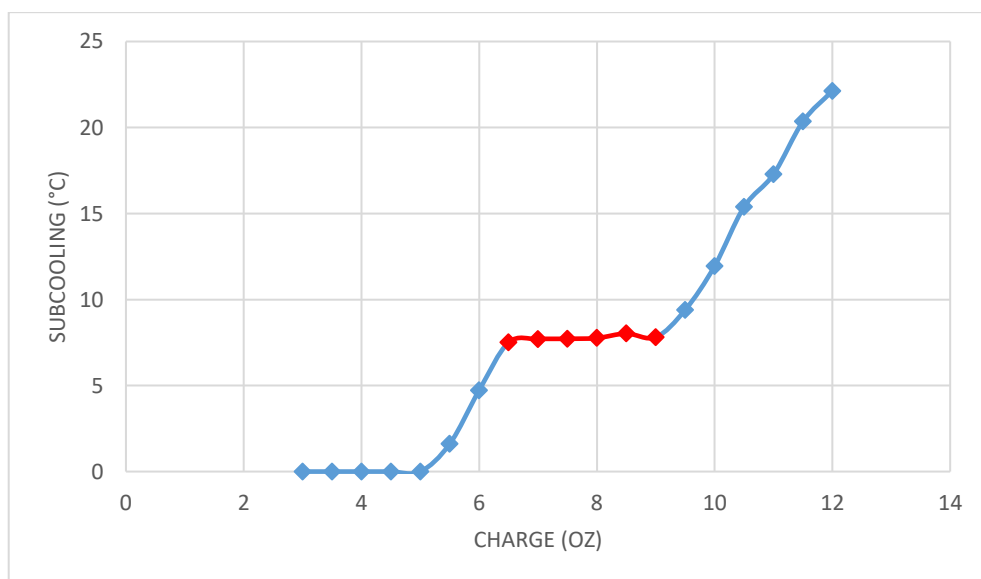


Fig. 2. 16: Graph collecting the behavior of the refrigerant subcooling after the condenser for all the simulations performed, the plateau used for the calculation of the refrigerant charge is highlighted in red and it is limited by 6.5 and 9 oz.

## 2.6 Model validation

The final step to conclude the modelling process is to provide validation that the results obtained are reasonably reliable and accurate. In order to do so, experimental tests are conducted on the actual AC loop and the results are compared with the numerical results obtained simulating the same conditions on the virtual system. The experimental data used for the validation are generally gathered performing bench test in laboratory; however, bench test data for the refrigeration system chosen for this analysis are not available. In order to still be able to validate the model, a different test was considered: cool down performed in a climatic wind tunnel on the entire vehicle. In this test many thermocouples were used to measure the temperature in the vehicle cabin; the air vent outlets; inlets of the air flowing through the heat exchangers of the AC system and on the refrigerant loop itself. Therefore, it was possible to extrapolate enough information to set a simulation reproducing the same experimental conditions and to compare the results obtained. Before going through all the input data selected to set the simulation, some considerations have to be done. Firstly, the test has been performed on the complete vehicle which means that it will be necessary to adjust the system by adding two components in order to match the system examined. Secondly, during the test the vehicle will be in motion and its speed will follow a precise pattern:

- 40 km/h for the first 1820 seconds
- 0 km/h for 120 seconds
- 105 km/h for 780 seconds
- 0 km/h for the last 1180 seconds

Therefore, the simulation performed is transient and, according to this, the input data are not constants but functions of the time.

### 2.6.1 Preparation of the model

In order to compare the results obtained in the simulation with the experimental ones, it is necessary to make two changes to the model. In the first configuration a chiller is added to withdraw heat from a second loop in charge of cool down the batteries of the vehicle. This component is attached to the system on a branch built in parallel with the TXV and the evaporator. In this new section of the system, a TXV is used to control the refrigerant flowing into the chiller, which is modelled as a volume of refrigerant exchanging heat with an external source (Fig. 2.17, detail a). The Thermal expansion valve added is identical to the one adopted in the original model. The heat exchanged in the chiller will be handled as thermic load input of the system. The second modification to be made is the implementation of an anti-frost system for the evaporator. Usually, in a belt-driven compressor, the temperature of the air at the outlet of the evaporator is controlled by disconnecting the compressor

from its source of power (i.e. crankshaft of the engine). Since the compressor adopted in this system is an electric one, the temperature of the air at the evaporator outlet can be regulated by an electronic control able to modulate the compressor RPM. This control has been provided by FCA and provides values for the compressor RPM using as input the speed of the vehicle, the actual air temperature at the outlet of the evaporator and the target temperature (Fig. 2.17, detail b).

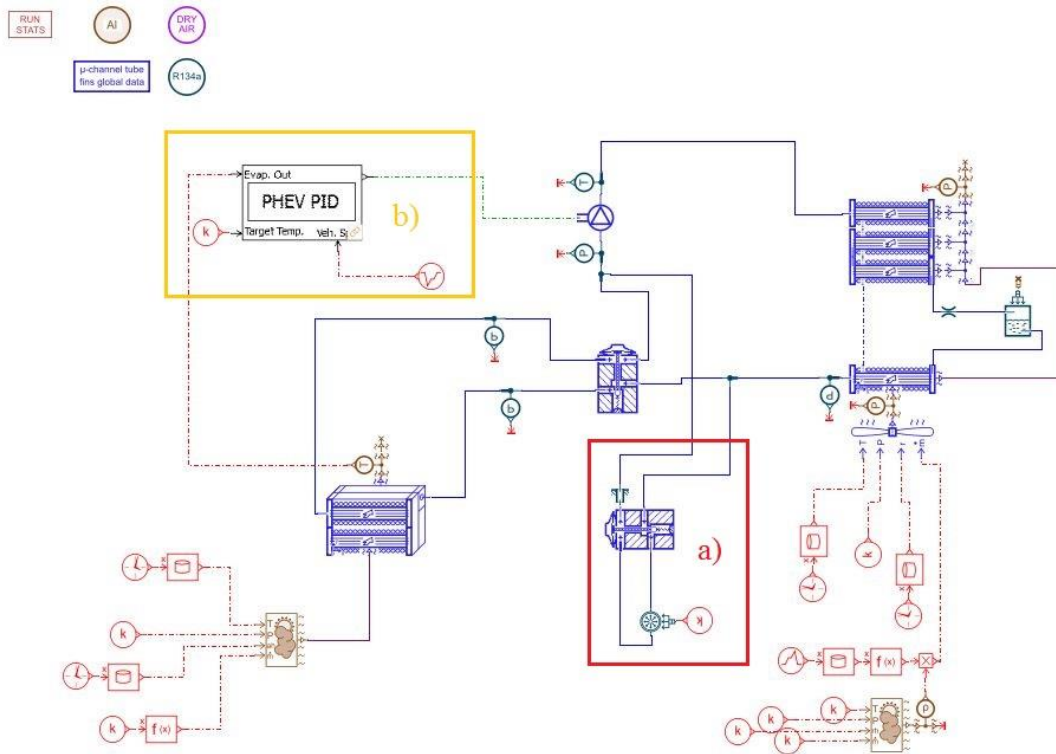


Fig. 2. 17: Modified model of the AC system ready to be validated. a) Branch of the system with the added TXV and chiller; b) electronic control of the compressor RPM to obtain a minimum temperature of the evaporator outlet air of 10°C.

## 2.6.2 Simulation set up

In this paragraph, all the input data and simulation parameter will be defined. The test and the simulation run for 3900 seconds, with a print interval of 2 seconds. According to this, each input has to be a constant or a function of time respecting this limitations.

The compressor RPM controller requires:

- Target temperature of the air at the evaporator outlet, which is a constant and has been set to 5°C
- Vehicle speed, which is a function of time and whose behavior is shown in Fig 2.18.

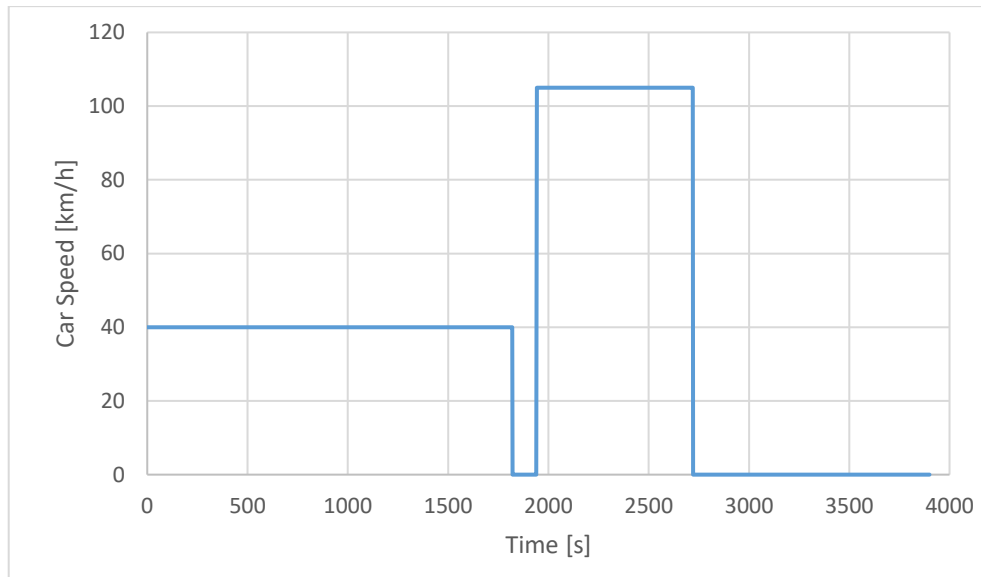


Fig. 2. 18: Graph showing the speed of the vehicle during the simulation as a function of time.

Another parameter to be set is the thermic load requested to the chiller. According to the experimental data gathered, the chiller heat flow rate has been assumed constant at 3 kW.

Finally it is necessary to specify the thermodynamic properties of the air flowing in the two heat exchangers: temperature, pressure, relative humidity, mass flow rate.

For the condenser:

- Air inlet temperature: function of time obtained calculating the average of the values measured by the 12 thermocouples placed in the condenser front (Fig. 2.19).
- Air inlet pressure: it is assumed to be constant at environmental pressure.
- Air inlet relative humidity: it is the relative humidity of the air of the wind tunnel and it is a function of time (Fig. 2.20).
- Air mass flow rate: it is a function of time and is affected by the vehicle speed. From datasheet, a value of mass flow rate corresponds to each value of speed (Fig. 2.21).

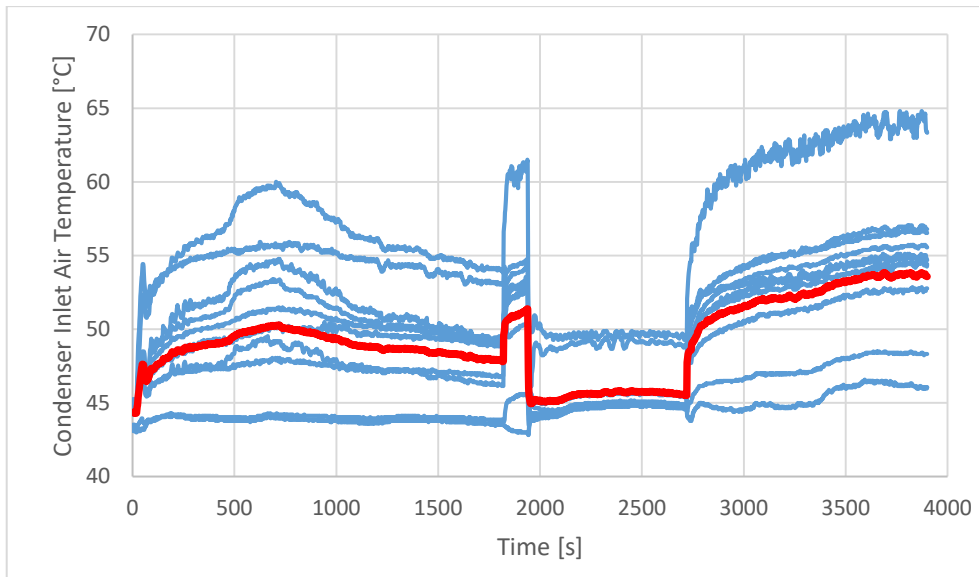


Fig. 2. 19: Behavior of the air temperature measured in different points of the condenser front as a function of time: in red the average one.

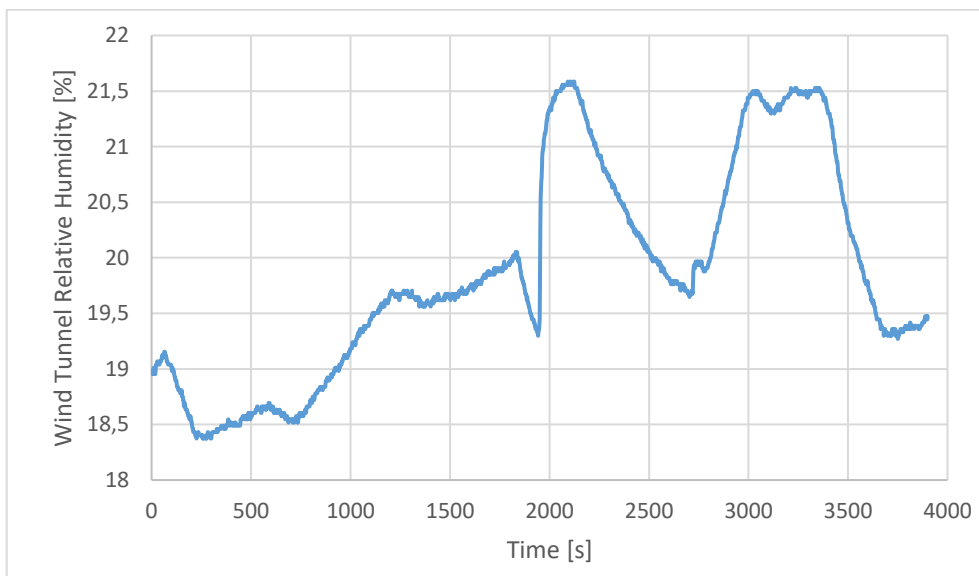
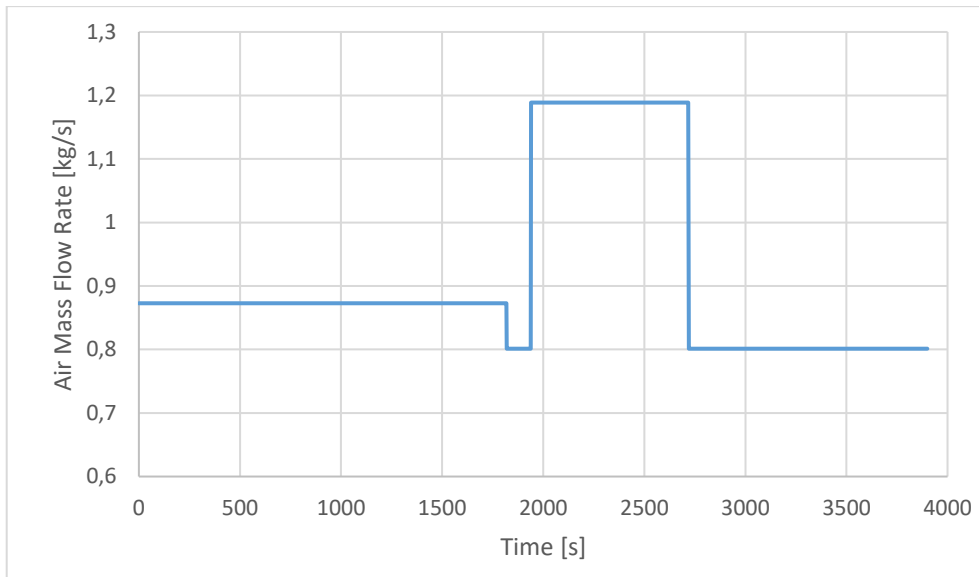


Fig. 2. 20: Behavior of the relative humidity of the air at the condenser inlet as a function of time.



*Fig. 2. 21: Behavior of the mass flow rate of the air flowing through the condenser as a function of time.*

Before defining the characteristics of the air flowing through the evaporator it is important to state that the experimental test considered is performed in recirculation mode. This means that the air considered is not fresh air from the environment but is recirculated air from the inside of the cabin.

Therefore, for the evaporator:

- Air inlet temperature is a function of time shown in Fig. 2.22 and obtained from a thermocouple placed in the recirculation duct.
- Air inlet pressure is assumed be constant at environmental pressure.
- Air inlet absolute humidity consists of an average, provided by FCA archives (Fig. 2.23), of the absolute humidity measurements collected through the years performing the same test. This approach has been implemented since this value has not been measured in the experimental test.
- Air mass flow rate is the maximum mass flow rate provided by the AC blower and it is kept constant throughout the entire test at 0.109 kg/s.

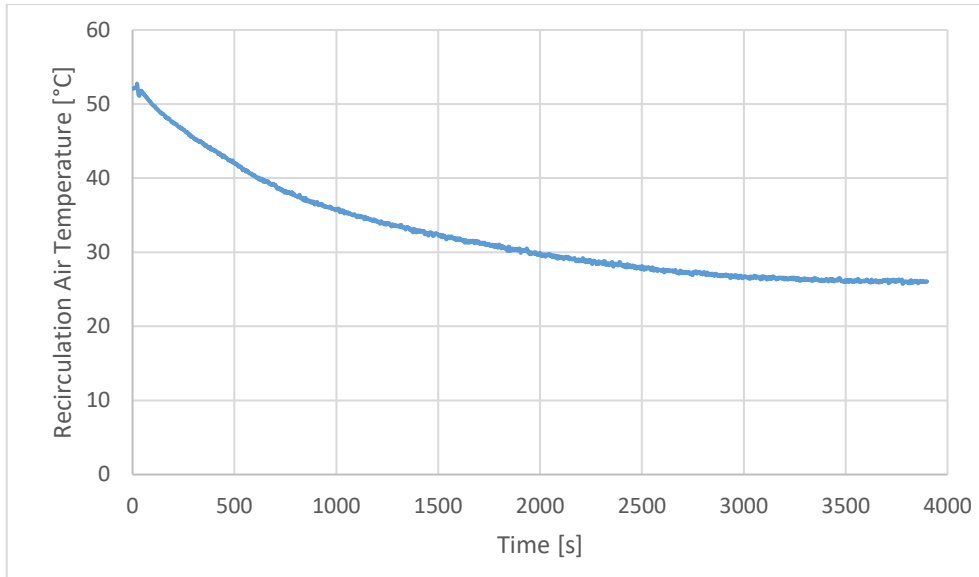


Fig. 2. 22: Behavior of the air temperature measured in the recirculation duct.

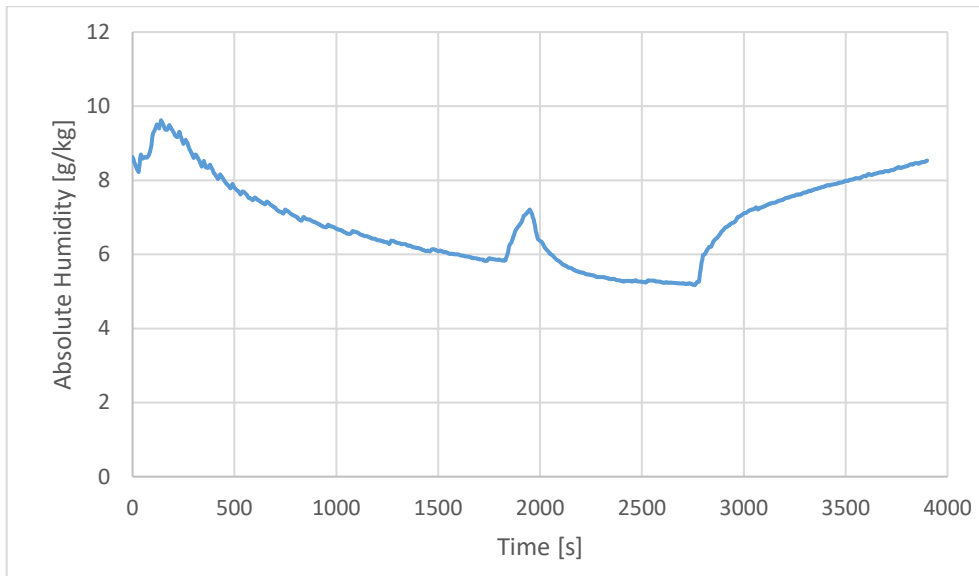


Fig. 2. 23: Behavior of the assumed absolute humidity of the air flowing through the evaporator.

### 2.6.3 Result Comparison

Once the simulation is completed, the values calculated for certain variables are observed and compared with experimental measurements in order to compute their deviation. The variables observed are:

- Evaporator outlet air temperature
- Evaporator outlet refrigerant temperature
- Compressor head pressure

In the following graphs is presented the comparison of such variables (Figs. 2.24-26).

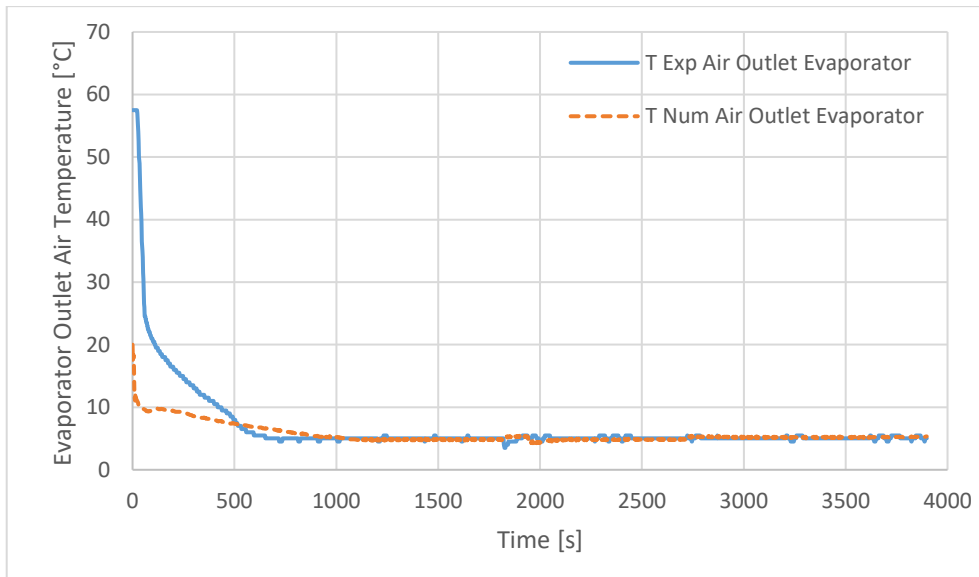


Fig. 2. 24: Comparison between the numerical evaporator outlet air temperature and the experimental one.

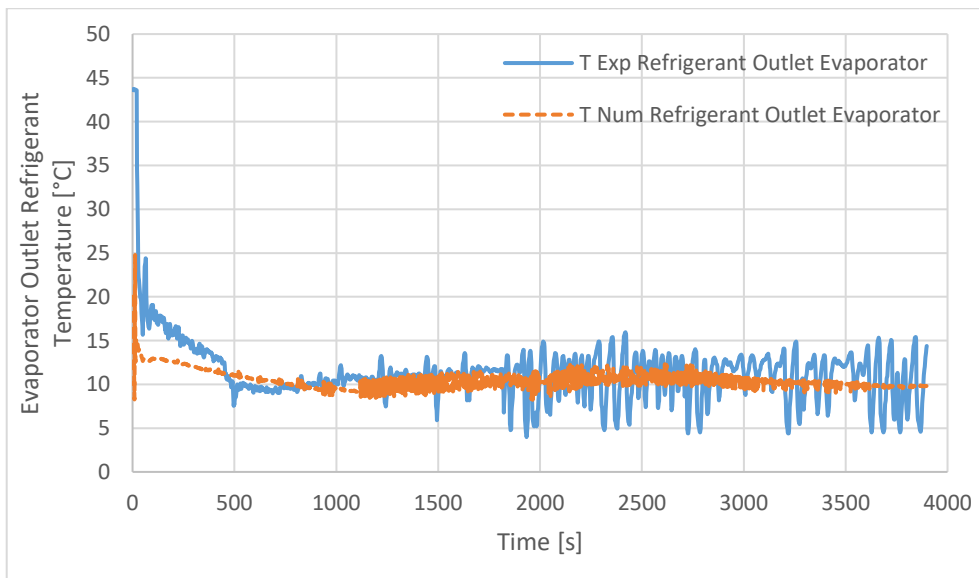


Fig. 2. 25: Comparison between the numerical evaporator outlet refrigerant temperature and the experimental one.

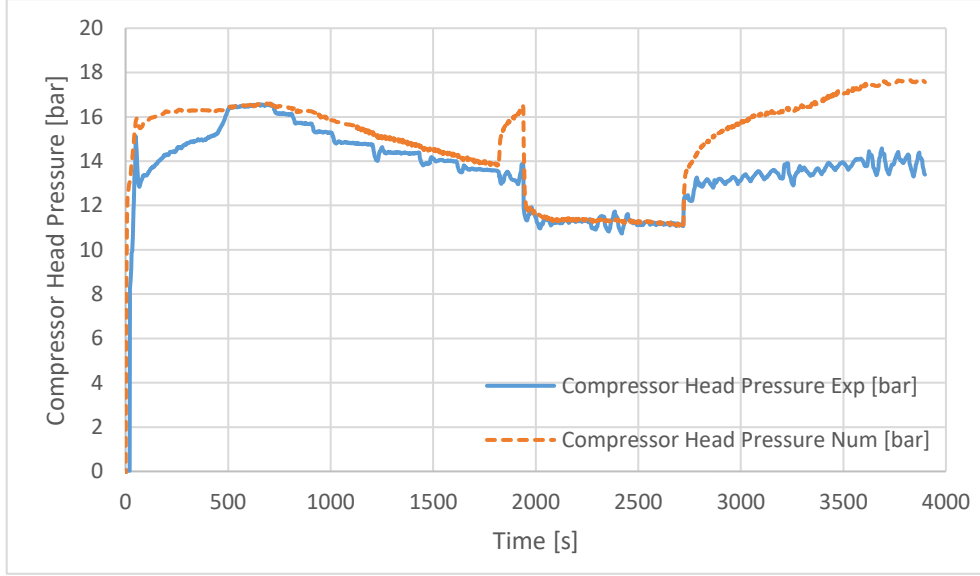


Fig. 2. 26: Comparison between the numerical compressor head pressure and the experimental one.

In order to evaluate the reliability and accuracy of the model, two parameters have been calculated: the validation metric (V), Eq. 2.8, and the cumulative average error (err), Eq. 2.9, both defined as a function of the relative error [68].

$$V = 1 - \frac{1}{t_{end} - t_0} \sum_{i=t_0}^{t_{end}} \tanh \left| \frac{y(t_i) - Y(t_i)}{Y(t_i)} \right| \quad (2.8)$$

$$err = \frac{1}{t_{end} - t_0} \sum_{i=t_0}^{t_{end}} \left| \frac{y(t_i) - Y(t_i)}{Y(t_i)} \right| \quad (2.9)$$

Where:

- $t_{end}$  and  $t_0$  are respectively the instants of end and start of the test
- $y(t_i)$  is the numerical value calculated at the instant  $i$
- $Y(t_i)$  is the experimental value measured at the instant  $i$

The metric selected normalizes the difference between computational results and experimental data, thus computing a relative error norm. However, this formulation is inappropriate when any of the  $Y(t_i)$  are close to zero and then it is necessary to add a condition: for any point in which  $Y(t_i)$  is lower than the 10% of the maximum value measured in the experimental test, the relative error considered is equal to zero. The absolute value permits the value of the relative error to accumulate not allowing positive and negative differences to accumulate. Finally, when the summation of the relative error becomes large, the validation metric approaches zero.

The results obtained for the validation metric and the cumulative average error are shown in Table 2.2.

<i>PARAMETER</i>	<i>V</i>	<i>err</i>
<i>Evaporator outlet air temperature</i>	97.48%	2.72%
<i>Evaporator outlet refrigerant temperature</i>	90.38%	10.43%
<i>Compressor head pressure</i>	95.14%	4.93%

*Table 2. 2: Values of the validation metric and of the cumulative average error for the validation of the refrigeration cycle.*

The value for the validation metric for all the parameter is higher than 90%, which can be considered a very high threshold. The lower one is represented by the evaporator outlet refrigerant temperature and it is due to the high oscillation in the values measured by the thermocouple. This behavior is caused by the action of the anti-frost system which acts on the compressor RPM in order to maintain the minimum outlet temperature of the air at 5 °C. Therefore, even if the error registered is higher, we can graphically confirm that the pattern of the curve is respected with high accuracy. The highest deviation of the numerical model with respect to the experimental result has been recorded at the start of the simulation: the temperature numerically calculated decreases faster than the one measured in the experiment. This difference in the behavior could be determined by the fact that at the beginning of the experimental test the solid components of the vehicle and the environment in which the system is operating are already at a high temperature and they need time to cool down. Unfortunately, this model is not able to consider all this factors that cause differences in the first transient of the simulation. If a vehicle cabin model was included and soak simulation was performed before the cool down with appropriate thermal mass, the drop in the mperature in the simulation would be more realistic. However, this does not affect the overall performance of the model that reproduces with high accuracy the behavior of the actual system.

## Chapter 3 – Heat Pump Model

### 3.1 Introduction

A solution widely used in many electric vehicles, among them also the previous version of the Fiat 500e, is the positive temperature coefficient heater (PTC heater). This device is able to transfer heat to the environment exploiting the Joule effect of a current carrying resistor [69]. In this chapter, a schematic has been designed in order to revert the cycle using the same compressor and external heat exchanger and adding an expansion valve, an internal condenser and bypass valves to direct the refrigerant. This procedure led to the development of a 1D model of a heat pump system, working at different environmental conditions. The results obtained were used to perform an energy and exergy analysis of the system developed, in order to understand its potential and provide insights for future development.

### 3.2 Schematic of the system

Starting from the simple schematic of the AC system already present in the car (compressor, external condenser, thermostatic expansion valve, internal evaporator) a new configuration has been designed in order to develop a new system capable of switching between cooling and heating operations according to the need. This has been achieved by implementing a three heat exchangers structure, as it is shown in Figs. 3.1 and 3.2.

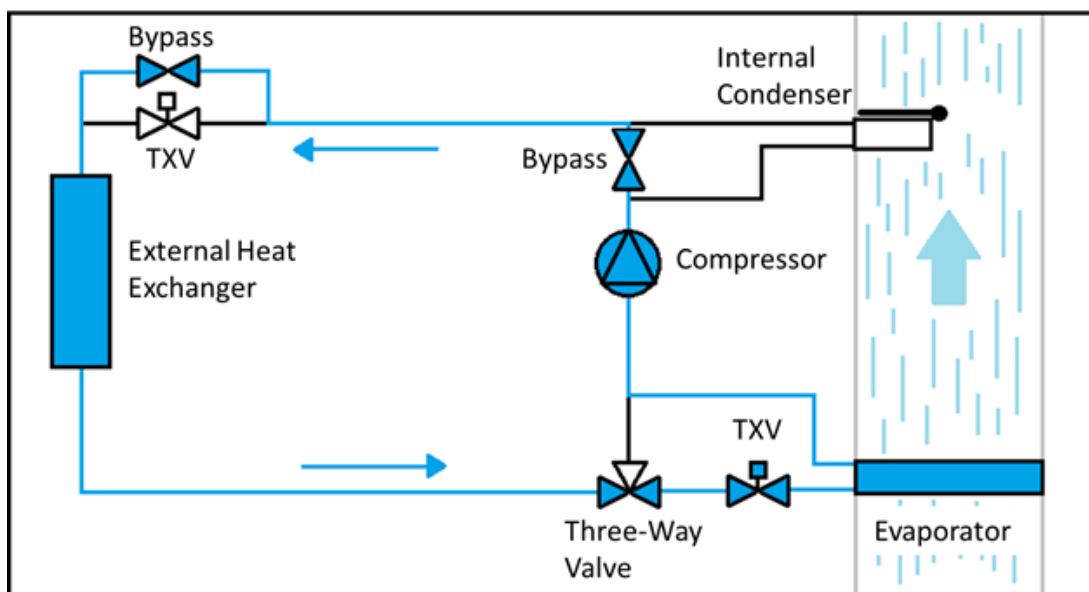
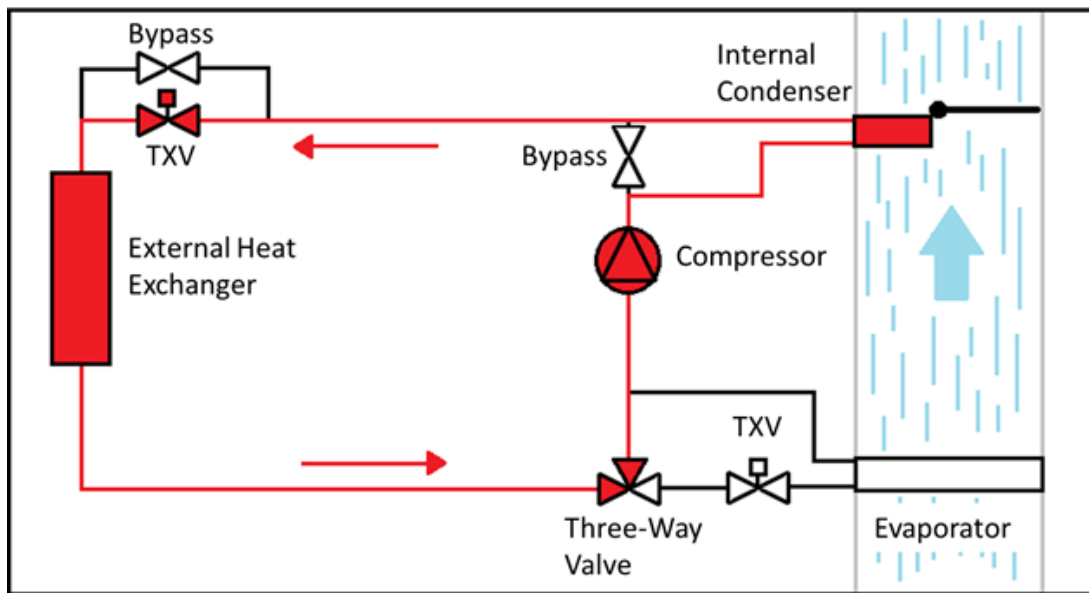


Fig. 3. 1: Schematic of the refrigeration cycle in the new structure of the system: the refrigerant goes through two bypass valves after the compressor, flows in the external heat exchanger (operates as a condenser), and it is directed by the three-way valve in a TXV and in the internal evaporator, completing the loop back to the compressor.



*Fig. 3. 2: Schematic of the heat pump cycle in the new structure of the system: the refrigerant goes through the internal condenser after the compressor, into an expansion valve, which precedes the external heat exchanger (operates as an evaporator) and finally is redirected to the compressor by the three-way valve.*

The schematic relies on the assumption that the external heat exchanger is able to work both as a condenser and an evaporator, depending on which loop is in function. The component present in the AC system is a condenser, which receives gas refrigerant and delivers liquid refrigerant after condensing it. Usually, to favor this operation, the inlet pipe of the condenser is placed at the top and the outlet one at the base. Thus, while the phase of the refrigerant changes, the liquid can easily flow down through the condenser under the effect of gravity. Furthermore, it is common practice to design the cross sectional area of the pipes according to the phase of the refrigerant flowing in it: if the refrigerant is liquid, its density is higher than the one in gaseous condition and, therefore, the section of the pipe required in order to have the same mass flow rate is lower. These characteristics, although implemented to support the operations of a condenser, prove to be obstacles to the activity of the evaporator (at the inlet, the refrigerant will be low pressure liquid, which will vaporize and leave the heat exchanger as gas) and the losses have to be overcome by the work of the compressor. Therefore, the performance of the components and the overall system are expected to be lower during operation as an evaporator with respect to a condenser.

An alternative approach to the problem could be an actual reversion of the direction of the fluid switching inlet and outlet. This could decrease the demand on the compressor and the collateral effects of changing the original purpose of the heat exchanger, however, it would require a complex and elaborated system of valves to complete the circuit of the refrigerant.

### 3.3 Modelling

There are various methods to reproduce the schematic presented in the previous paragraph. However, they are all bound by one condition: compressor and external heat exchanger are already known, and they cannot be modified, while there is no information available on the new components (expansion valve and internal condenser). One approach is to start the analysis by defining the desired output and then designing an appropriate cycle to achieve it. Hence, the desired heat rejection or the desired air temperature at the end of the new internal condenser would be predefined and this information would be sufficient to calculate all the variables concerning the air side. On the other hand, the number of unknown variables on the refrigerant side is too high to directly compute. Therefore, it is necessary to start an iterative process assuming an initial mass flow rate in order to design a thermodynamic cycle on the pressure-enthalpy diagram as given by Eq. 3.1.

$$\dot{Q}_{cond} + \dot{Q}_{evap} = \dot{W}_{comp} \quad (3.1)$$

The second approach, which is the one described in this chapter, consists of virtually modeling the new components of the system with the available information and then completing the cycle. By simulating the system on Amesim it will be possible to evaluate its performance, however, the greatest obstacle encountered in this approach is the lack of information on the components.

#### 3.3.1 Components shared with the AC system

The first step is to retrieve the available information from the AC system already modelled in Chapter 2, which can be considered as starting point. Figure 3.3 shows the components extracted and used to model the new heat pump system: compressor, condenser and receiver. The compressor does not need any modification or consideration since its operation does not change, therefore, it is implemented as described in paragraph 2.3.1 and characterized by the same data.



### 3.3.2 Components Added to the Loop

Additional components are needed to complete the heat pump system such as an expansion valve introduced before the external heat exchanger and the internal condenser, shown in Fig. 3.2. Designing a mechanical Thermostatic expansion valve (TXV), as the one modelled and used in the AC system presented in paragraph 2.3.3, is challenging and requires information that is not readily available. Therefore, in order to simplify the modelling of the system, the expansion valve added to the loop is represented by a variable restriction electronically controlled so that the overheat at the end of the evaporator is maintained at the desired level. This solution reproduces the functioning concept of a TXV avoiding the definition of a 4-quarter diagram needed for its operation. The valve is represented in Amesim by a modulated generic restriction (submodel “TPFMGR00” shown in Fig. 3.4), which is controlled through its cross-sectional area according to a dimensionless signal input at port 1, as shown in Eq. 3.2. This signal is limited between 0 (i.e. fully closed restriction) and 1 (restriction fully open). The maximum cross sectional area is defined in the settings.

$$area = signal * area_{max} \quad (3.2)$$

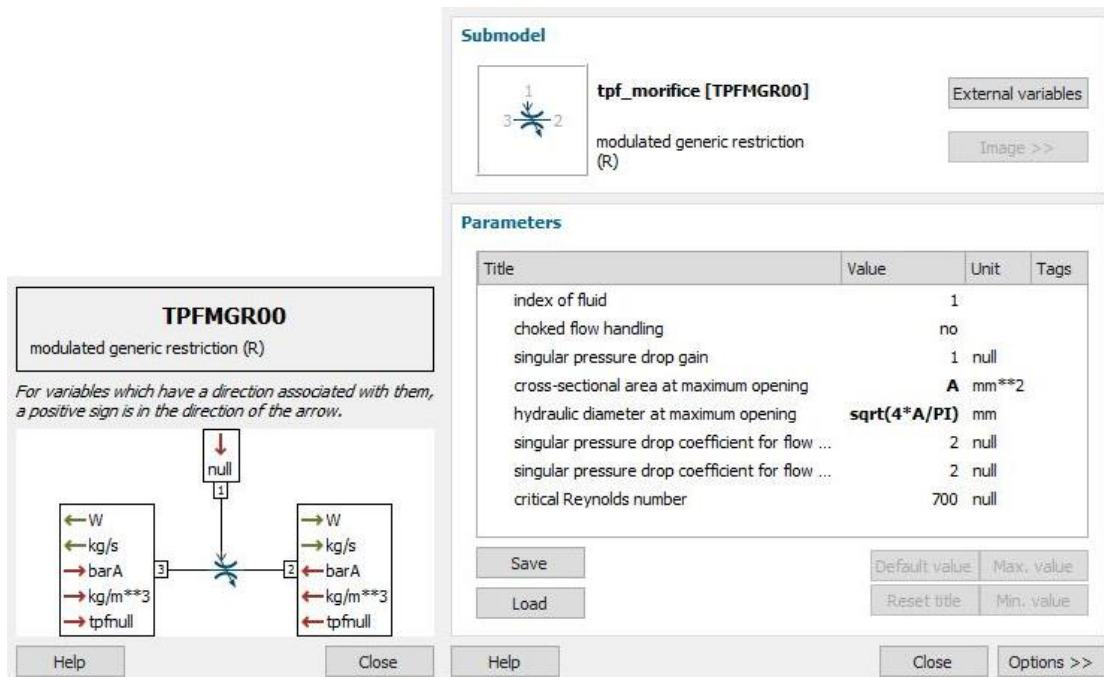


Fig. 3. 4: Element adopted for the modulated generic restriction representing the expansion valve; list of external variables and parametrization.

The controller in charge of providing the input signal of the variable restriction is a proportional integral (PI) control, whose function is to minimize the difference between the actual overheat of the refrigerant at the end of the heat exchanger and the desired one.

The last and most challenging step is the design of the internal heat exchanger. This condenser will be added after the internal evaporator in the air duct delivering the mass flow air to the cabin. Therefore, the main design requirement is compact dimensions in order to fit the section of the duct. The component has been modelled modifying the external condenser used in the refrigeration loop in order to satisfy the new dimensions requirement. The component downsizing is also consistent with the lower heat rejection required to the condenser of the heat pump system with respect to the one of the AC system. Furthermore, the use of a smaller condenser will probably affect the refrigerant virtual charge analysis, requiring a lower amount of refrigerant compared to the one needed by the refrigeration system. The dimension reduction has been obtained matching the width of the condenser with the width of the internal evaporator and removing the two internal passes hence maintaining an even number of passes so that the inlet and outlet pipes are on the same side. The height of the condenser depends on the number of tubes adopted for each pass, however it has to be lower than the height of the evaporator in order to fit the duct. It has been decided to design the heat exchanger modifying an already known condenser instead of redesigning, in order to apply the same thermodynamic correlation obtained for the condenser modelled in paragraph 2.3.2 assuming that the changes applied to the component do not affect the calibration significantly. It is important to highlight that the scope of the research is not to redesign new components in order to produce an actual heat pump system. The focus is on developing a virtual model able to provide reasonable data to analyze the potential of such system. Therefore, while its final characteristic or structure might result odd, the thermodynamic properties of the refrigerant in each point will follow a realistic cycle. This will provide the information required to replace the strange components used with actual ones provided by suppliers.

### **3.3.3 System level model**

The components have been assembled together in Amesim with direct connections instead of pipes, as it was done for the refrigeration cycle in Chapter 2. Figure 3.5 shows the model of the system, highlighting the components shared with the AC system. As explained in paragraph 3.3.1, the receiver cannot be placed inside the external heat exchanger as it was before, but it still has to be included in the system, therefore, it has been placed inside the internal condenser.

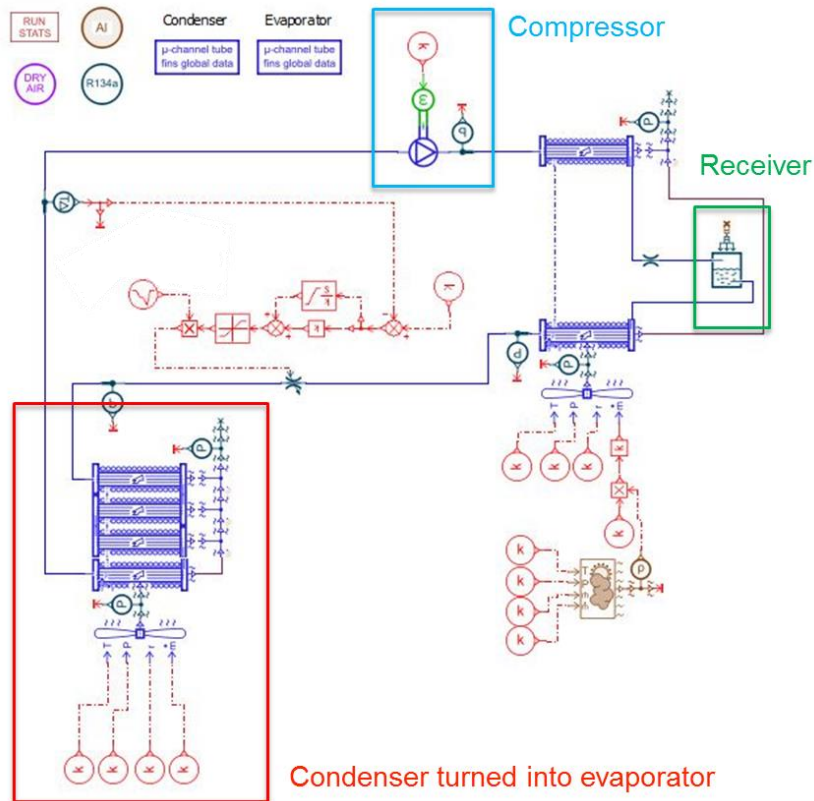


Fig. 3. 5: Heat pump model with highlighted the components shared with the AC system.

Once the model is assembled, it needs to be calibrated before allowing it to operate a complete thermodynamic cycle. The tuning of the system is performed by modifying some selected parameters:

- Maximum cross-sectional area of the variable restriction adopted as an expansion valve
- Number of tubes adopted in each of the two passes of the internal condenser
- Capacity of the receiver

By changing these parameters a specific change in the behavior of the system was observed; this behavior is described by the following variables:

- Mass flow rate
- Overheat at the end of the evaporator
- Subcooling at the end the condenser
- Pressure at the compressor outlet

In order to obtain the desired system, these variables will have to meet some requirements. Since it is not possible to directly control them, this is achieved by acting on the parameters listed before. Before being able to actually calibrate these parameters, it is necessary to set the input conditions of the system in the model, which are collected in Table 3.1.

<i>INPUT PARAMETER</i>		<i>VALUE</i>
<i>Compressor</i>	RPM	8400
<i>Condenser</i>	Air Temperature	-20 °C
	Air Pressure	1.01325 bar
	Air Relative Humidity	19%
	Air Mass Flow Rate	330 m <sup>3</sup> /h
<i>Evaporator</i>	Air Temperature	-20 °C
	Air Pressure	1.01325 bar
	Air Relative Humidity	19%
	Air Mass Flow Rate	0.287 kg/s

*Table 3. 1: Input parameters of the heat pump model. These parameters will be also used for the calculation of the optimal virtual refrigerant charge.*

The air mass flow rates provided to each heat exchanger are the ones adopted in paragraph 2.5 and switched between condenser and evaporator since their positions swapped. At this stage the model is ready for calibration as follows. At first, the number of tubes in the passes (9 and 4) and the capacity of the receiver (same adopted in the AC system, 0.1 L) have been kept constant while decreasing the maximum cross-sectional area of the restriction. This operation decreases the mass flow rate of the refrigerant. As a consequence of this, a lower rate of refrigerant is introduced in the heat exchangers. Therefore, while overheat and subcooling at the end of the respective heat exchanger increase, the pressure at the compressor outlet might increase as well to an unacceptable value. In such a scenario the temperature and pressure in the condenser begin to increase until the calculations stall and the simulation cannot proceed. This happens because with a low mass flow rate the condenser is not able to transfer the required amount of heat. Therefore, in order to still provide the correct amount of heat, the temperature difference between the condenser inlet and the outlet refrigerant is increased, with resultant rise of the compressor efforts. The objective is then to find a value of the maximum cross-sectional area of the restriction in the expansion valve which allows the PI controller to maintain 10 °C of overheat at the end of the evaporator without increasing the subcooling at the end of the condenser at a value higher than 10 °C. In this case, the mass flow rate required to obtain the desired overheat is so low that the subcooling increases, risking a stall in the optimization as explained previously. In order to decrease the value of the subcooling, the number of tubes in the internal condenser has been varied. In fact, by increasing the number of tubes in the first pass and decreasing them in the second pass it is possible to lower its value under the desired one. However, the configuration obtained presents 18 tubes in the first pass and 1 tube in the second one which is not a readily available structure.

Once the system is assembled and calibrated, a virtual refrigerant charge analysis was performed, following the procedure explained in paragraph 2.5. However, the values obtained for the subcooling

revealed a high sensitivity of the system to changes in the refrigerant charge: one ounce of refrigerant makes the difference between a complete and successful simulation and a failed simulation. Therefore, in order to complete the refrigerant charge analysis, it is necessary to lower this sensitivity and identify the interval of refrigerant mass values that defines a plateau in the subcooling. This has been done by increasing the capacity of the receiver from 0.1 L to 0.15 L. The graph in Fig. 3.6 shows the behavior of the subcooling at the end of the condenser for each value of refrigerant charge adopted. As explained in paragraph 2.5, the optimal virtual refrigerant charge is evaluated according to Eq. 3.3 and it is equal to 7.5 oz, which is still a lower value with respect to the AC system.

$$\begin{aligned} & \text{virtual refrigerant charge} \\ & = \text{charge}_{plt,min} + 0.75 * (\text{charge}_{plt,max} - \text{charge}_{plt,min}) \end{aligned} \quad (3.3)$$

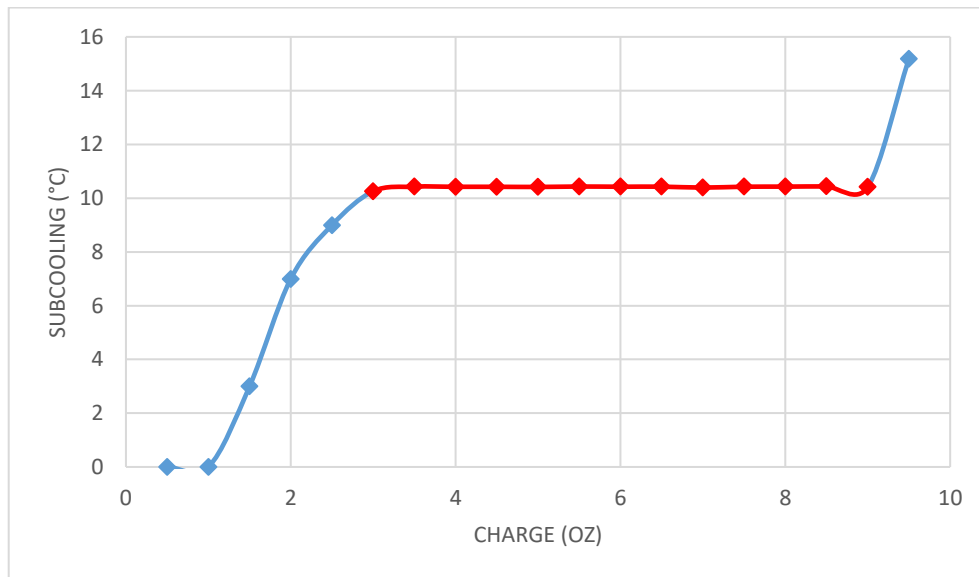


Fig. 3. 6: Graph collecting the behavior of the refrigerant subcooling after the condenser for all the simulations performed, the plateau used for the calculation of the refrigerant charge is highlighted in red and it is limited by 3 and 9 oz.

### 3.3.4 Results

The heat pump system modelled has finally been simulated using the input conditions collected in Table 3.1 and the final values of the parameters used for the calibration:

- The maximum cross-sectional area of the variable restriction is equal to 4 mm
- 18 tubes adopted in the first pass of the internal condenser and 1 tube in the second one
- The capacity of the receiver is equal to 0.15 L

Even if the configuration of the heat exchanger is definitely odd the results produced are fairly reasonable for what concern the thermodynamic transformations of the refrigerant happening in compressor, condenser and expansion valve. However, the results of the calculation performed in the

evaporator are inconsistent: going through the evaporator the temperature decreases for both refrigerant and air. This outcome, even if it is definitely unexpected, can be physically explained. The heat transfer in the evaporator is expected to happen at constant pressure: on one hand the temperature of the air decreases, on the other hand, after the phase change, the temperature of the refrigerant increases until the desired overheat. However, in the modelled evaporator, during the heat transfer the pressure of the refrigerant decreases, hence the saturation temperature also diminishes. Once the refrigerant has completely evaporated the desired overheat is reached, but pressure and temperature are now lower than the expected value. The reason behind this abnormal behavior has to be identified in the evaporator characterization. As previously explained in paragraph 3.3.1, this heat exchanger was originally operating as a condenser in the refrigeration system and, therefore, the data available for the thermodynamic calibration describe its performance in such conditions. In order to make up for the lack of data to calibrate the heat exchanger as an evaporator it was decided to use the same parameters. Due to these limitations in the characterization, the evaporator is not able to achieve the demanded performance with an isobaric transformation and, therefore, a pressure drop is forced in order to still fulfill its duties. However, given the results provided by any other component (state 2, 3 and 4 in Fig. 3.7), it has been decided to complete the cycle by manually selecting the properties of state of the refrigerant at the end of the evaporator (state 1). Such thermodynamic state has been characterized as following: since the heat transfer in the heat exchanger should happen at constant pressure, state 1 will share the same pressure of state 4; furthermore, in paragraph 3.3.3 it has been stated that the aim of the expansion valve is to keep an overheat of 10 °C at the end of the evaporator. Given this two properties Amesim allows the user to easily obtain temperature, specific enthalpy and specific entropy. These considerations led to the completion of the cycle: the thermodynamic properties of each state are collected in Table 3.2 and they are reported in the pressure vs specific enthalpy diagram shown in Fig. 3.7 and in the temperature vs specific entropy shown in Fig. 3.8.

<i>State Point</i>	<i>Pressure [barA]</i>	<i>Temperature [degC]</i>	<i>Mass Flow Rate [kg/s]</i>	<i>Specific Enthalpy [kJ/kg]</i>	<i>Specific Entropy [kJ/kgK]</i>
1	1.102	-14.2	0.0087	392.013	1.777
2	4.813	125.6	0.0087	514.741	2.037
3	4.800	4.0	0.0088	205.465	1.019
4	1.103	-24.2	0.0088	205.467	1.028

Table 3. 2: Thermodynamic properties of the 4 states of the cycle performed by the heat pump shown in Figs. 2.7 and 2.8.

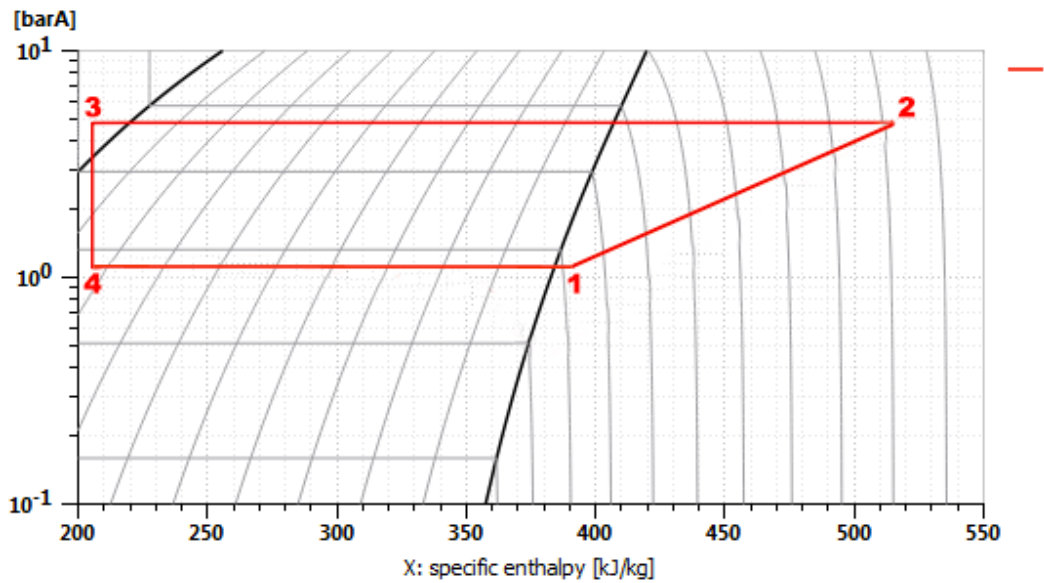


Fig. 3. 7: Pressure-enthalpy diagram of the thermodynamic cycle performed by the heat pump (from 1 to 2 the compressor, from 2 to 3 the condenser, from 3 to 4 the expansion valve and from 4 to 1 the evaporator).

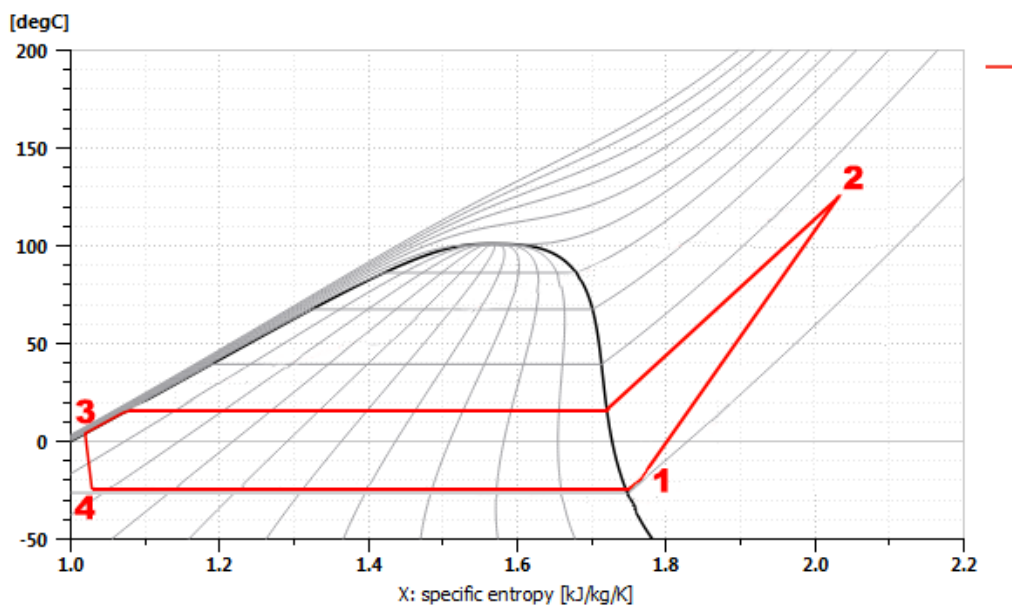


Fig. 3. 8: Temperature-entropy diagram of the thermodynamic cycle performed by the heat pump (from 1 to 2 the compressor, from 2 to 3 the condenser, from 3 to 4 the expansion valve and from 4 to 1 the evaporator).

In order to check if the procedure followed to assume the new state 1 of the cycle, the thermodynamic properties of the air at the inlet and outlet of each heat exchanger have been collected in Table 3.3. Therefore, it is now possible to evaluate the heat rejection on both refrigerant and air side applying Eq. 3.4 and Eq. 3.5 and compare the results obtained: their sum should be null. As shown in Table 3.2, the mismatch in the performances of the condenser and the evaporator and the consequent pressure drop generate a slight change in the refrigerant mass flow rate. For simplicity, in the future

calculations the refrigerant mass flow rate in the system has been considered constant and equal to the average value: 0.00879 kg/s.

	<i>Inlet</i>	<i>Outlet</i>	<i>Mass</i>	<i>Specific</i>
	<i>Temperature</i>	<i>Temperature</i>	<i>Flow Rate</i>	<i>Heat <math>C_p</math></i>
	<i>[degC]</i>	<i>[degC]</i>	<i>[kg/s]</i>	<i>[kJ/kgK]</i>
<i>Condenser</i>	-20	1	0.127	1.006
<i>Evaporator</i>	-20	-25.3	0.287	1.006

Table 3. 3: Thermodynamic properties of the air at the inlet and outlet of condenser and evaporator shown in Figs. 3.7 and 3.8.

$$\dot{Q}_{refr} = H_f - H_i = \dot{m}_{refr}(h_f - h_i) \quad (3.4)$$

$$\dot{Q}_{air} = \dot{m}_{air}c_{p,air}(T_f - T_i) \quad (3.5)$$

From the results collected in Table 3.4 it is possible to state that, while there was a malfunctioning on the refrigerant side calculations in the evaporator, there is a match between the results provided for the air side and the one obtained with the assumed state.

	<i>Refrigerant</i>	<i>Heat</i>	<i>Air Heat Rejection</i>
	<i>Rejection [kW]</i>		<i>[kW]</i>
<i>Condenser</i>	-2.719		2.700
<i>Evaporator</i>	1.640		-1.533

Table 3. 4: Heat rejection in the heat exchangers evaluated from both the refrigerant and the air side.

It is important to highlight that the PI controller plays an important role in the operations of the model. The calculations of this simulation do not converge to a perfect steady-state and oscillates around the desired value of overheat. In this situation the oscillation range is of 3-4 degrees of overheat and, therefore, can be neglected since the scope of the thesis does not focus on automatic control. However, this controller instability will be cause of important issues in the phase described in the next paragraphs.

### 3.4 Second simulation in different environmental conditions

The results obtained in the first simulation, in which the heat pump works in an environment at  $-20\text{ }^{\circ}\text{C}$ , prove that the performance of the system in such extreme conditions is poor and insufficient as the heat rejection provided is enough to increase the temperature of the air of  $21\text{ }^{\circ}\text{C}$  and, therefore, it needs an auxiliary source to successfully perform the heating operations. Furthermore, there is a very high chance that the evaporator core will be subjected to frost formation due to the low temperature working conditions.

In this paragraph, a different environmental condition has been considered in order to identify an operating range that optimize the performance of the heat pump system.

A new simulation was performed considering as inlet air temperature of both evaporator and condenser  $0\text{ }^{\circ}\text{C}$ . Due to this shift in the environmental conditions the PI control returned an unacceptable outcome as the simulation stalled after a significant oscillation in the values calculated and the pressure and temperature of the refrigerant in the condenser increased excessively. In order to avoid this behavior, the desired overheat at the end of the evaporator has been decreased to  $5\text{ }^{\circ}\text{C}$ . In this way, the mass flow rate increases, diminishing the subcooling at the end of the evaporator and the risk of stalling the calculations. However, in this case, the amplitude of the oscillation is not negligible and the control created is not able to stabilize the loop. As explained before, automatic controls are not the focus of this research and, therefore, it has been decided to select a specific instant of the simulation and extract the thermodynamic cycle performed in that instant. The selected point has been chosen in order to have the overheat value close to the desired one, assuming that this procedure will provide a thermodynamic cycle close to the one that would have been obtained in a convergent simulation. As it happened in the previous model, the results provided for the state at the end of evaporator are inconsistent: again the temperature decreases in both the refrigerant and the air. Following the same procedure explained in paragraph 3.3.4, the cycle has been completed by selecting appropriate state of the refrigerant after the evaporator. The thermodynamic properties of such cycle are collected in Table 3.5 and shown in Figs. 3.9 and 3.10, which represent the thermodynamic cycle respectively in the pressure-enthalpy diagram and in the temperature-entropy one.

State Point	Pressure [barA]	Temperature [degC]	Mass Flow Rate [kg/s]	Specific Enthalpy [kJ/kg]	Specific Entropy [kJ/kgK]
1	2.717	3	0.0212	401.865	1.745
2	12.216	128.1	0.0212	510.672	1.955
3	12.192	39.3	0.0132	255.264	1.186
4	2.718	-2.0	0.0132	255.877	1.206

Table 3. 5: Thermodynamic properties of the 4 states of the cycle performed by the heat pump shown in Figs. 3.9 and 3.10.

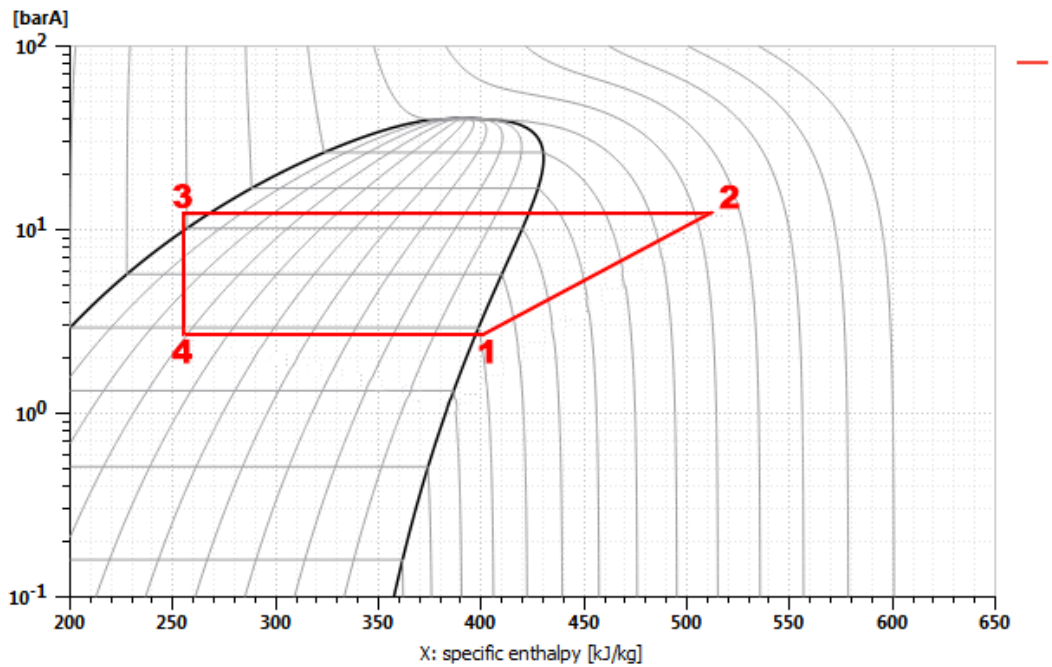


Fig. 3. 9: Pressure-enthalpy diagram of the thermodynamic cycle performed by the heat pump (from 1 to 2 the compressor, from 2 to 3 the condenser, from 3 to 4 the expansion valve and from 4 to 1 the evaporator).

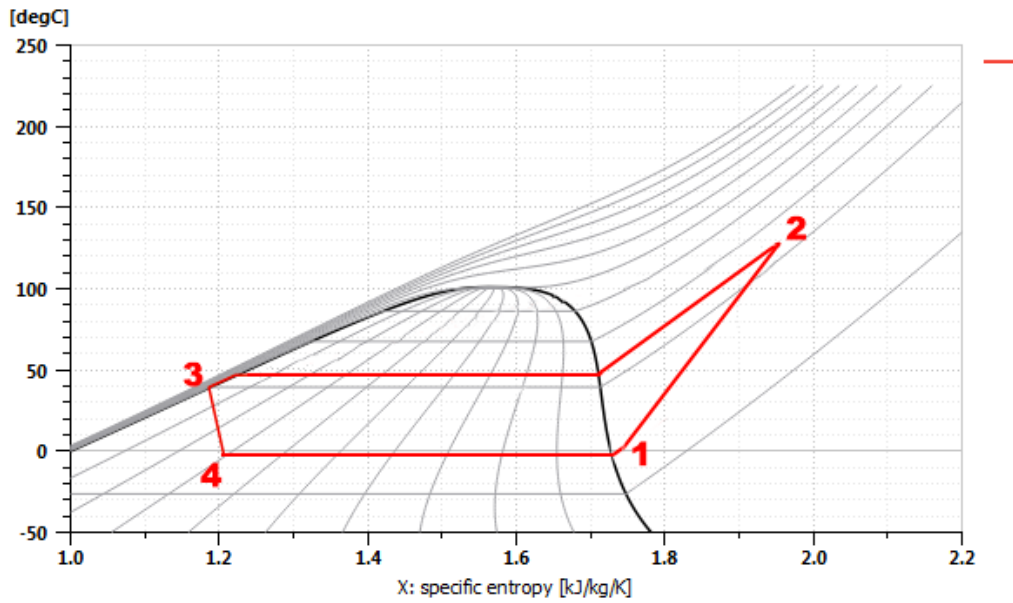


Fig. 3. 10: Temperature-entropy diagram of the thermodynamic cycle performed by the heat pump (from 1 to 2 the compressor, from 2 to 3 the condenser, from 3 to 4 the expansion valve and from 4 to 1 the evaporator).

Applying Eq. 3.4 and Eq. 3.5 to the data collected in Tables 3.5 and 3.6, it is possible to compare the heat rejection evaluated on the refrigerant side, according to the cycle finally obtained, and the ones computed on the air side, according to the values retrieved by the model.

	<i>Inlet</i>	<i>Outlet</i>	<i>Mass</i>	<i>Specific</i>
	<i>Temperature</i>	<i>Temperature</i>	<i>Flow Rate</i>	<i>Heat C<sub>p</sub></i>
	[degC]	[degC]	[kg/s]	[kJ/kgK]
<i>Condenser</i>	0	33.2	0.118	1.006
<i>Evaporator</i>	0	-2.8	0.28745	1.006

Table 3. 6: Thermodynamic properties of the air at the inlet and outlet of condenser and evaporator shown in Figs. 3.9 and 3.10.

The results obtained present a great discrepancy for two reasons. The first and most evident one is that there is no match between the heat rejections for both condenser and evaporator. This means that in this case, unlike the previous model, there is no evident relation between the thermodynamic cycle performed by the refrigerant and transformation in the air state. The second reason is represented by the magnitude of the heat rejection evaluated on the refrigerant side. Comparing the values collected in Table 3.7 with the ones in Table 3.4, they are three times higher and such performances are probably out of the potential of such system.

	<i>Refrigerant Heat Rejection [kW]</i>	<i>Air Heat Rejection [kW]</i>
<i>Condenser</i>	-7.464	3.955
<i>Evaporator</i>	5.156	0.810

Table 3. 7: Heat rejection in the heat exchangers evaluated from both the refrigerant and the air side.

Numerous obstacles and difficulties prevented the model from being executed successfully and the following list reports the most evident sources of error that brought the model to a stall:

- The lack of experimental data to calibrate the external heat exchanger as an evaporator – the assumption that the same parameters obtained while the heat exchanger was operating as a condenser is not valid.
- The lack of an appropriate internal condenser - the condenser used has been built using the information available on the condenser of the refrigeration cycle. According to the difficulties encountered in obtaining the desired overheat at the end of the evaporator without compromising the operations of the internal condenser demonstrate the inadequacy of its use.
- The oscillation produced by an unstable control. Such behavior was further compromised by the high sensitivity of the system to any changes in the mass flow rate refrigerant.

### 3.5 Energy and Exergy Analysis

Since the results obtained in paragraph 3.3.4 represent a physically feasible heat pump cycle (using the proper components), they have been used to perform an energy and exergy analysis. This should provide an idea of the potential of the system in these extreme conditions. The equations used to build the mathematical model have been written taking the work of I. Dincer and M. Rosen [70] as a reference. In order to simplify the analysis of the system considered, some assumptions are needed:

1. All of the processes are steady-state and steady flow, with negligible potential and kinetic energy effects, and no chemical or nuclear reactions. This is validated by the methodology of the data collection, since the model is run for a long interval of time allowing to discard the data collected during the transient period.
2. The air is considered an ideal gas with constant specific heat. The specific heat of a fluid, calculated at constant pressure, is a function of its temperature. However, in the situation considered the value of the specific heat for the air remains constant at 1.006 kJ/kgK. The value of the specific heat for vapour has been assumed to be 1.855 kJ/kgK.
3. Heat transfer to the system and work transfer from the system are considered positive. This is the convention adopted for attribution of the signs and it will be respected by the results.

4. Heat transfer and refrigerant pressure drop in the connecting tubes are negligible since the model of the heat pump system has been assembled using direct connections instead of pipes.
5. The reference state is taken to be at standard conditions, when the temperature is equal to 24 °C and the pressure is 1.01325 bar, as shown in Table 3.9

According to these assumptions we can proceed with the calculation of the specific physical exergy of each state of the system, as shown in Fig. 3.11.

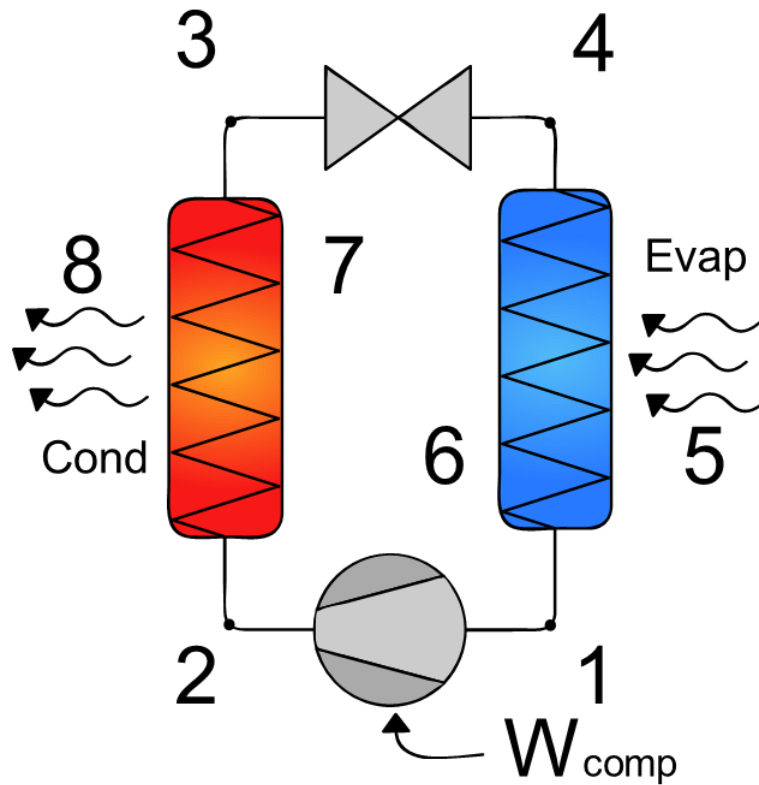


*Fig. 3. 11: Simple schematic of the heat pump system to define each state of the cycle: 1 refrigerant evaporator outlet/compressor inlet, 2 refrigerant compressor outlet/condenser inlet, 3 condenser outlet/expansion valve inlet, 4 expansion valve outlet/evaporator inlet, 5 air evaporator inlet, 6 air evaporator outlet, 7 air condenser inlet, 8 air evaporator outlet.*

The specific flow exergy of the refrigerant (states 1, 2, 3, 4) is evaluated applying Eq. 3.6 on the values collected in Table 3.2.

$$ex_{r,i} = (h_i - h_0) - T_0(s_i - s_0) \quad (3.6)$$

The specific flow exergy of air is calculated applying Eq. 3.7 on the values reported in Table 3.8.

$$\begin{aligned}
ex_{a,i} = & (C_{p,a} + \omega C_{p,v})T_0 \left[ \left( \frac{T}{T_0} \right) - 1 - \ln \left( \frac{T}{T_0} \right) \right] \\
& + (1 + 1.6078\omega)R_a T_0 \ln \left( \frac{P}{P_0} \right) \\
& + R_a T_0 \left\{ (1 + 1.6078\omega) \ln \left[ \frac{(1 + 1.6078\omega_0)}{(1 + 1.6078\omega)} \right] + 1.6078 \ln \left( \frac{\omega}{\omega_0} \right) \right\}
\end{aligned} \tag{3.7}$$

Where  $R_a=0.2871$  kJ/kgK is the ideal gas constant for air and the index '0' indicates the reference state, whose properties are shown in Table 3.9.

	<i>Temperature</i> [degC]	<i>Specific</i> <i>Humidity Ratio</i>	<i>Mass</i> <i>Flow</i> <i>Rate</i> [kg/s]
<i>Condenser Inlet</i>	0	0.0001	0.118407
<i>Condenser Outlet</i>	33.2	0.0001	0.118407
<i>Evaporator Inlet</i>	0	0.0001	0.28745
<i>Evaporator Outlet</i>	-2.8	0.0001	0.28745

Table 3. 8: Thermodynamic properties of the air at the inlet and outlet of condenser and evaporator.

	<i>Refrigerant</i> <i>Reference State</i>	<i>Air</i> <i>Reference</i> <i>State</i>
<i>Temperature</i> [°C]	24	24
<i>Pressure</i> [kPa]	101.325	101.325
<i>Specific Enthalpy</i> [kJ/kg]	423.72	-
<i>Specific Entropy</i> [kJ/kgK]	1.898	-
<i>Specific Humidity Ratio</i>	-	0.002

Table 3. 9: Reference state considered for the refrigerant and the air.

Using the following equations, the values of the exergy destruction through each component can be calculated.

In the compressor:

$$\dot{E}x_{dest,Comp} = \dot{m}_r(ex_1 - ex_2) + \dot{W}_{Comp} \tag{3.8}$$

Where:

$$\dot{W}_{Comp} = \dot{m}_r(h_2 - h_1) \quad (3.9)$$

In the condenser:

$$\dot{E}x_{dest,Cond} = \dot{m}_r(ex_2 - ex_3) + \dot{m}_a(ex_7 - ex_8) \quad (3.10)$$

In the orifice tube:

$$\dot{E}x_{dest,Exp} = \dot{m}_r(ex_3 - ex_4) \quad (3.11)$$

In the evaporator:

$$\dot{E}x_{dest,Evap} = \dot{m}_r(ex_4 - ex_1) + \dot{m}_a(ex_5 - ex_6) \quad (3.12)$$

For each component, it is possible to evaluate a parameter called relative irreversibility (RI), which describes the contribution of each component in the system performance degradation.

$$RI_i = \frac{\dot{E}x_{dest,i}}{\dot{E}x_{dest,tot}} \quad (3.13)$$

Where:

$$\dot{E}x_{dest,tot} = \dot{E}x_{dest,Comp} + \dot{E}x_{dest,Cond} + \dot{E}x_{dest,Exp} + \dot{E}x_{dest,Evap} \quad (3.14)$$

Finally, the criteria used to characterize the efficiency of a heat pump is the coefficient of performance (COP) that is calculated according to both approaches: first (3.15) and second (3.16) laws of thermodynamics.

$$COP_{HP} = \frac{\dot{Q}_{cond}}{\dot{W}_{comp}} \quad (3.15)$$

$$COP_{HP,ex} = \frac{\dot{m}_r(ex_2 - ex_3)}{\dot{W}_{comp}} \quad (3.16)$$

The results of the analysis are provided in Table 3.10.

	$\dot{E}x_{dest} [kW]$	$RI [\%]$	$COP_{HP}$	$COP_{HP,ex}$
<i>Compressor</i>	0.6791	59.68	-	-
<i>Condenser</i>	0.4043	35.53	-	-
<i>Expansion Valve</i>	0.0235	2.73	-	-
<i>Evaporator</i>	0.0311	2.06	-	-
<i>Overall system</i>	1.1380	100	2.52	0.0552

*Table 3. 10: Results of the energy and exergy analysis performed on the system proposed in paragraph 3.3.*

According to the results shown in Table 3.10, the major components responsible for the exergy destruction of the system are compressor and condenser. On the other hand, the impact of expansion valve and evaporator can be considered negligible. The high value of the exergy destruction evaluated for the compressor can be easily explained remembering the considerations made in paragraph 3.3 while developing and simulating the heat pump model. On one hand, since the condenser has not enough refrigerant mass flow rate to provide the required heat rejection, the pressure at the compressor outlet is increased in order to have a higher temperature difference through the condenser. On the other hand, the compressor is in charge of providing enough pressure to overcome all the obstacles encountered in using the external heat exchanger as an evaporator instead of as a condenser, as presented in paragraph 3.3.1. According to these considerations, it is no surprise that the compressor represents the component with the higher exergy destruction. In fact, the work required at the compressor is excessive, hence determining a poor coefficient of performance evaluated according to the First Law of thermodynamics and a very low exergetic coefficient of performance.

## **Chapter 4 – Cabin Model**

### **4.1 Introduction**

A first attempt to improve the possibilities of 1D cabin models and be able to achieve a distribution of the temperature inside the cabin was the creation of a multi-zone cabin [50]. This has been achieved by dividing the volumes in order to consider multiple lumped mass. According to this, the thermic loads on the external surfaces have been split assigning them correctly to the respective volume. The principle behind this methodology is interesting and reasonable, however it presents a flaw that cannot be fixed relying only on a 1D software, which is accounting for the thermodynamic interactions between the different volumes. In this chapter, a new tool provided by Simcenter Amesim (Siemens) has been implemented to approach the problem such that the limitations of previous methods are addressed: the Embedded CFD Tool. After explaining the functioning principles of the tool, the modelling process will be presented. The procedure will consist of defining the geometry in the 3D environment; placing the air vents and defining their dimension; characterizing the material and defining the environmental conditions; and defining the properties of the air flowing in each vent. In order to optimize the results of the process, experimental data have been used as input of the system so that it is possible to immediately analyze the effect of every implementation while building the model.

It is also important to remark that this feature is new and only recently it has been released into the market, hence, there is vast room for improvement. On this purpose, Amesim developers kindly accepted to collaborate in the development of the project. Therefore, considerations and suggestions will be done in order to contribute in the evolution of this tool.

### **4.2 Embedded CFD Tool**

This tool has been developed in order to define a simplified 3D environment to better take into account the effects of the 3D air flow and to organize the cabin volume in different zones interacting with each other. To achieve this 3D environment simulation Simcenter Amesim, in charge of performing the 1D calculations, was coupled with STAR-CCM+, which performs the 3D calculations. This allows for solar radiation and the convective heat exchange with the air flow to be accounted for. More precisely, STAR-CCM+ computes a heat transfer coefficient depending on the air velocity and the mass flow rates between the interfaces, while Amesim is in charge of the calculation of:

- moist air flow average temperature in each zone
- mass temperatures of the car cabin

- energy balance within the components

In this study the volume of the cabin was divided in 10 different volumes, each of which represents a specific zone inside the vehicle, as we can see in Fig. 4.1.

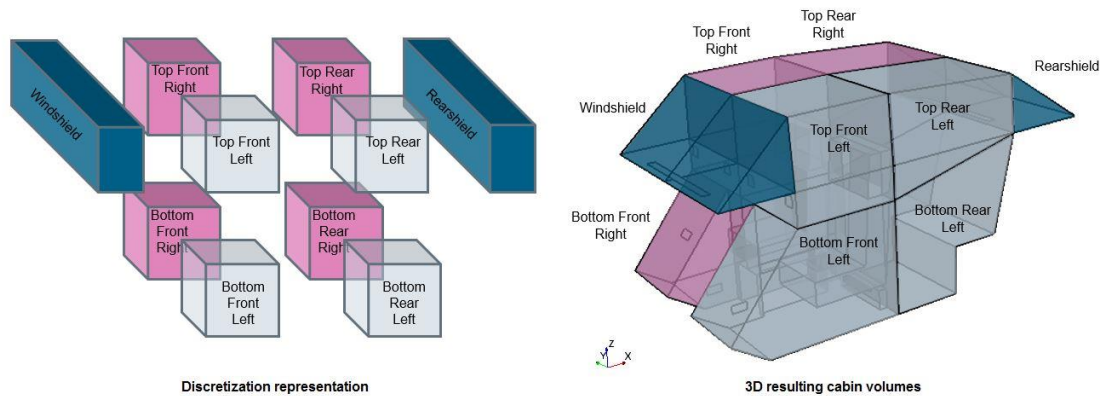


*Fig. 4. 1: Representation of the cabin space split in 10 volumes.*

The calculations between the different volumes at the interfaces are made following the principle of the conservation of mass, both in Amesim and in STAR-CCM+. The Embedded CFD Tool, as it is shown in Fig. 4.2, has only one output port and different inputs as follows:

- 9 air vents to provide the properties of the air flowing inside the cabin from the HVAC system (temperature, pressure, relative humidity, mass flow rate): 1 defrosting vent in the windshield, 4 air vents in the dashboard (top front, 2 for each zone), 2 air vents in the front feet zones (bottom front, 1 for each zone), 2 air vents in the rear feet zones (bottom rear, 1 for each zone)
- The speed of the vehicle, which can be a constant or a function of time
- The external air temperature, which can also be a constant or a function of time

The output port provide the properties of the air entering the recirculation duct. The value of the variables provided by this port can be very significant, since most of the experimental test performed on the vehicle (as for example the cool down considered for the validation) can be performed in recirculation mode.

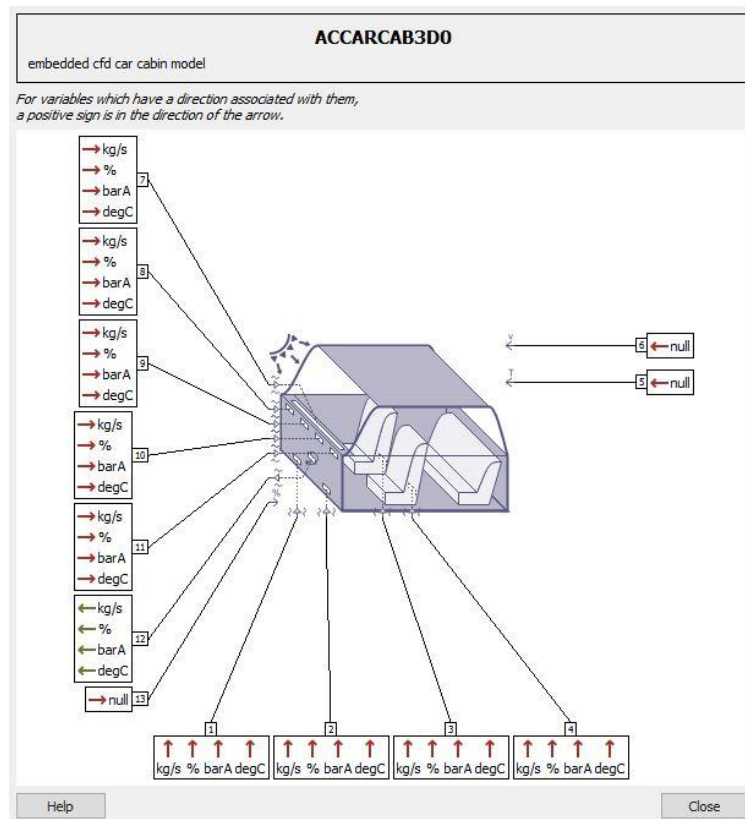


Fig. 4. 2: The Embedded CFD Tool and its external variables.

The tool has a first interface that allows the user to provide some basic information to the software: the initialization of the parameters of the model and definition of the material of the solid parts of the cabin. The initialization consists of:

- Temperature of the solid surfaces of each volume
- Temperature of the interfaces between the different zones
- Average temperature of the air inside each volume
- Mass flow air in each zone

On the other hand, the materials requested by the tool are: glass, steel, canvas, interior trim, seat foam.

Furthermore, the ambient conditions need to be specified using the submodel “THAMBCON0”, which allows the user to define the solar radiation to which the vehicle is subjected.

In order to define the interface between Simcenter Amesim and STAR-CCM+, the tool is equipped with the Embedded CFD car cabin application. This application is divided in 4 sections which represent different stages of the modelling process: Geometry, Physics, Run, Post Processing.

In the geometry section the user can set the main dimensions of the cabin needed to create the related CAD model in STAR-CCM+. This section is further divided in 4 different parts:

- Outside Geometry: to set all the external dimensions of the car cabin
- Inside Geometry: group concerning the dimensions of seats of the vehicle

- Air Vents: to define each air vent position and its width and height
- Body Components: parameters that determine the thickness of each layer of the car body (roof, side panels, windows)

Once all the information required have been provided, the software will be able to fully build the CAD of car cabin.

The second section is concerned with the physics and these parameters allow the user to enable the definition of reference conditions and properties, the definition of physical material properties and, lastly, the determination of the mesh properties, as follows:

- Material radiative exchange properties: emissivity, absorption factor and transmission factor for transparent materials
- Air flow orientation for each air vent
- Parameters for the initialization of the fluid domain for the CFD simulation
- Average mesh size of the fluid domain

This information allow the model to generate an automatic mesh of the volume considered.

The next step requires to set the parameters that govern the CFD simulation and the coupling between Amesim and STAR-CCM+. The coupling scheme is transient and enables the user to perform a complete transient simulation on Amesim using boundary conditions provided by the CFD calculations. This boundary conditions are evaluated running a steady-state simulation on STAR-CCM+ with the initial inputs provided by Amesim. During the evolving of the simulation, this conditions can become obsolete with respect to current state of the system and, therefore, every time they need to be updated, the 1D simulation on Amesim is stopped and a new steady-state simulation is performed on STAR-CCM+ using up-to-date variables provided by Amesim. Therefore, it is also necessary to define a stopping process in order to trigger the communication between Amesim and STAR-CCM+ at relevant moments. This can be done following different stopping criteria:

- Monitoring the changes of significant variables
- Selecting specific instants during the simulation
- Defining time intervals
- At switch conditions

At the end of this section, results will be generated and the simulation can be considered complete. The last division, the post-processing, simply allows the user to store the values of the variables of interest regardless if they have been calculated by Amesim or STAR-CCM+.

### **4.3 Development of the Model**

In this paragraph, each step of the modelling of the cabin of the Fiat 500e will be explained and analyzed thoroughly, outlining all the decisions made and proposing ideas for further improvement.

### 4.3.1 External Variables Input

In order to clearly see the effects of every decision taken in the modelling process, the first step has been to select all the experimental data required as input of the system (Fig. 4.2). The experimental test in examination is the same cool down test considered in the first chapter implemented to validate the refrigeration loop. The test is a cool down performed in a climatic wind tunnel on the entire vehicle. The solar radiation flux to be specified in the ambient conditions is  $1000 \text{ W/m}^2$ . The test is performed in full recirculation mode, which means that the air flowing through the evaporator consists entirely of air coming from the cabin and not from the external environment. One input required is the speed of the vehicle during the experiment (Fig. 4.3) defined as follows:

- 40 km/h for the first 1820 seconds
- 0 km/h for 120 seconds
- 105 km/h for 780 seconds
- 0 km/h for the last 1180 seconds

Another information to be provided to the model is the temperature of the tunnel environment, which is almost kept constant at  $43.8^\circ\text{C}$ , as shown in Fig. 4.4.

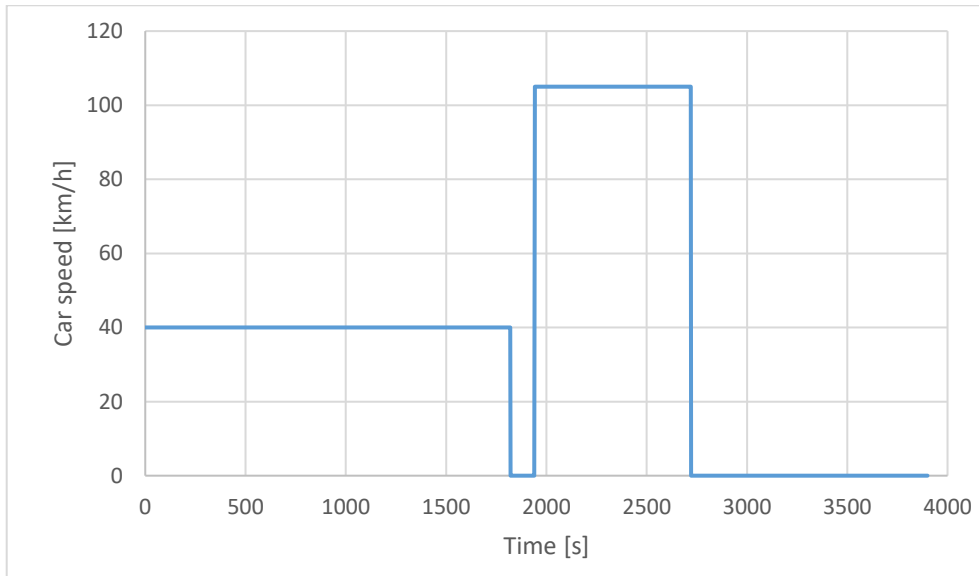


Fig. 4. 3: Graph showing the speed of the vehicle during the simulation as a function of time.

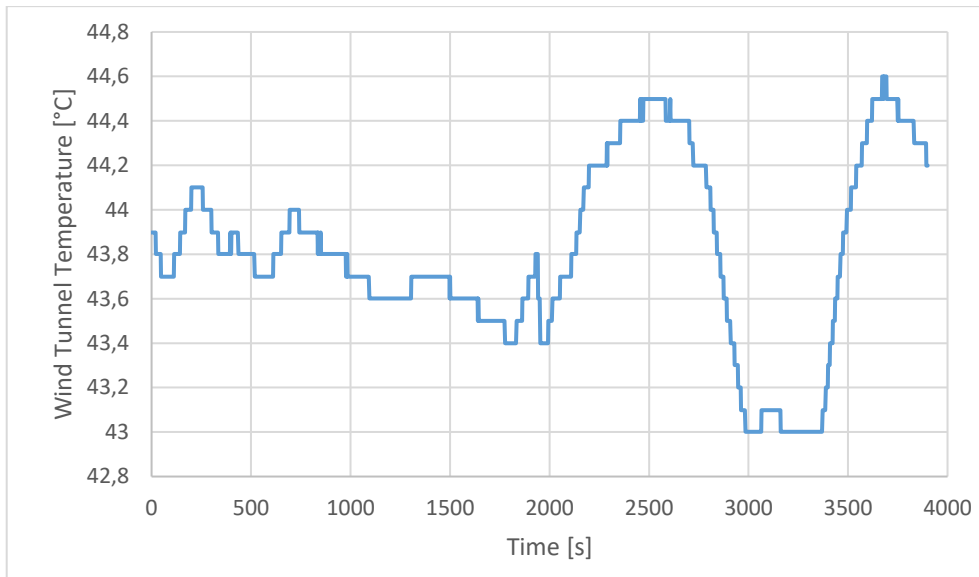


Fig. 4. 4: Graph showing the temperature of the wind tunnel during the simulation as a function of time.

The last set of data required are the properties (temperature, pressure, relative humidity and mass flow rate) of the air flowing through the 9 air vents. During the cool down test only the 4 top front vents allow the air to flow inside the cabin (right, center right, center left, left), while the others are closed, as shown in Fig. 4.5.

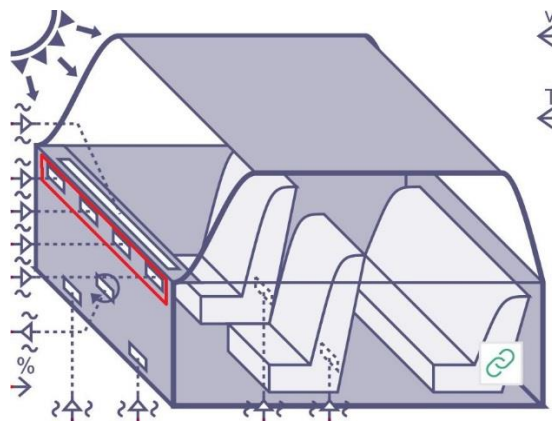


Fig. 4. 5: The air vents used in the cool down test are shown in red.

In order to exclude all the other air vents in the model it is sufficient to set the mass flow rate of air to zero hence, they will not have any impact on the simulation. As with the evaporator in the first chapter, the mass flow rate provided by the blower is 330 m<sup>3</sup>/h and it is split in equal parts between the 4 top front vents. Also, the absolute humidity is the same as provided to the evaporator in the refrigeration loop and it is shown in Fig. 4.6.

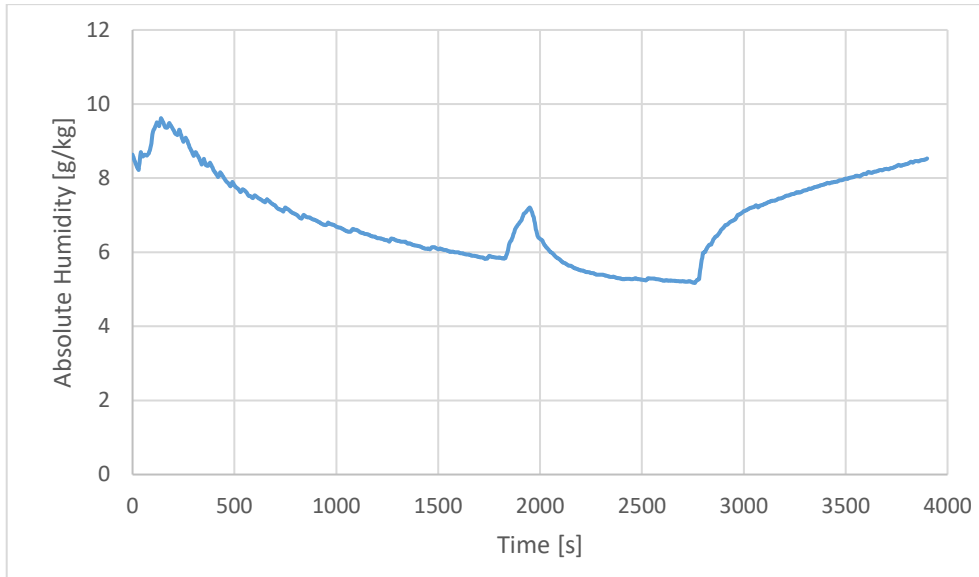


Fig. 4. 6: Behavior of the assumed absolute humidity of the air flowing through the evaporator.

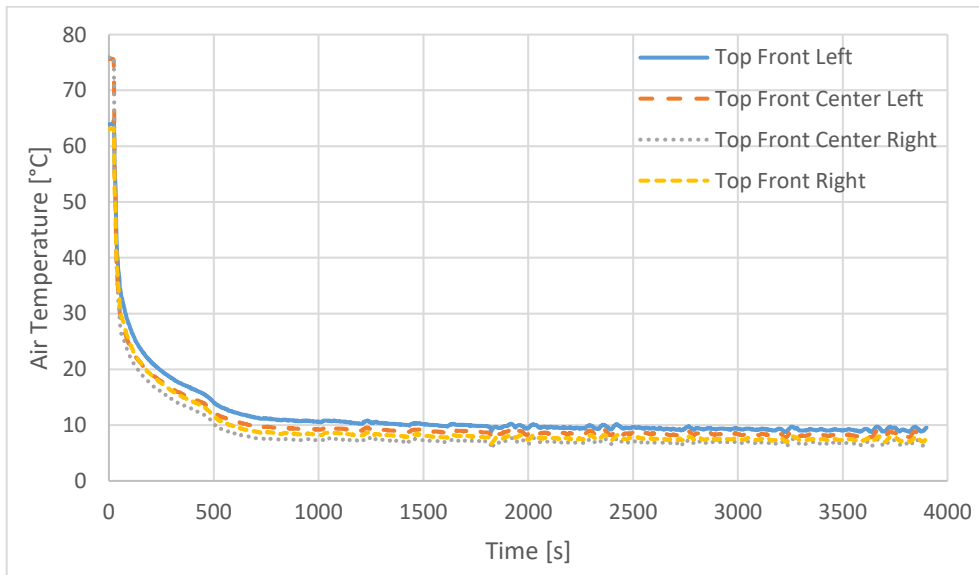


Fig. 4. 7: Temperature of the air flowing in the top front vents during the cool down test.

The pressure is assumed to be constant at environmental pressure while the temperature of the air at each air vent considered is provided by the measurements of 4 different thermocouples during the test. Therefore, they will be represented by a function of time and the values will be different for each vent (Fig. 4.7). Finally, the last operation is to provide the values of temperature and mass flow rate to initialize each component of the model. The air mass flow rate in each zone has been set to 0 since at the beginning of the test the vehicle is turned off and the HVAC system is not operational. Then, each zone requires the initial temperature of its solid surfaces and the average initial temperature of its air. For simplicity, these values have been assumed as the first value measured by the thermocouple placed in the respective zone in the experimental test for each volume. To give a clarifying example, if the temperature measured by the driver head thermocouple measures 70°C then this will be the value of the initial temperature of the top front left (i.e. average air, roof, side

and seat). Although this method of initialization is not very accurate it is reasonably sufficient to run a simulation, since every element included in each volume should be in thermal equilibrium with each other.

### 4.3.2 Geometry Definition

In this phase of the modelling process, the aim is to provide every information needed in order to build the 3D CAD environment for Amesim and STAR-CCM+ (Fig. 4.8).

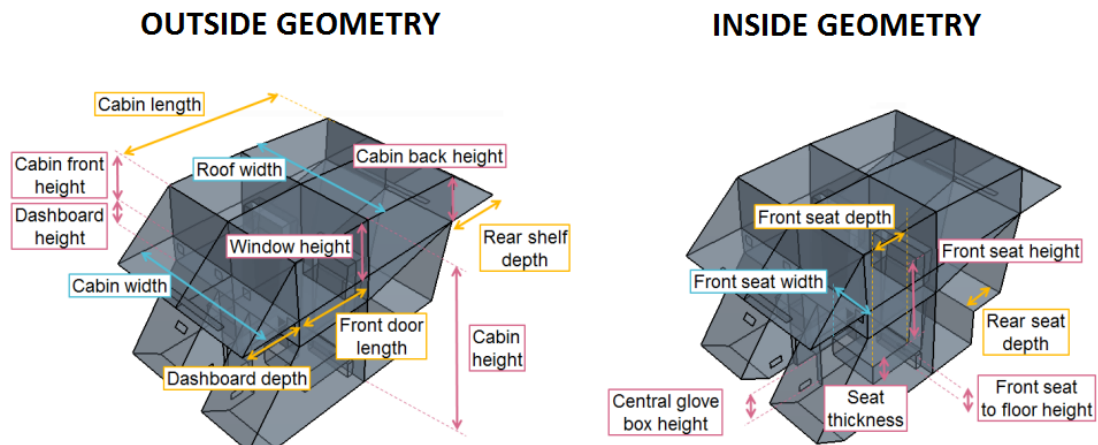
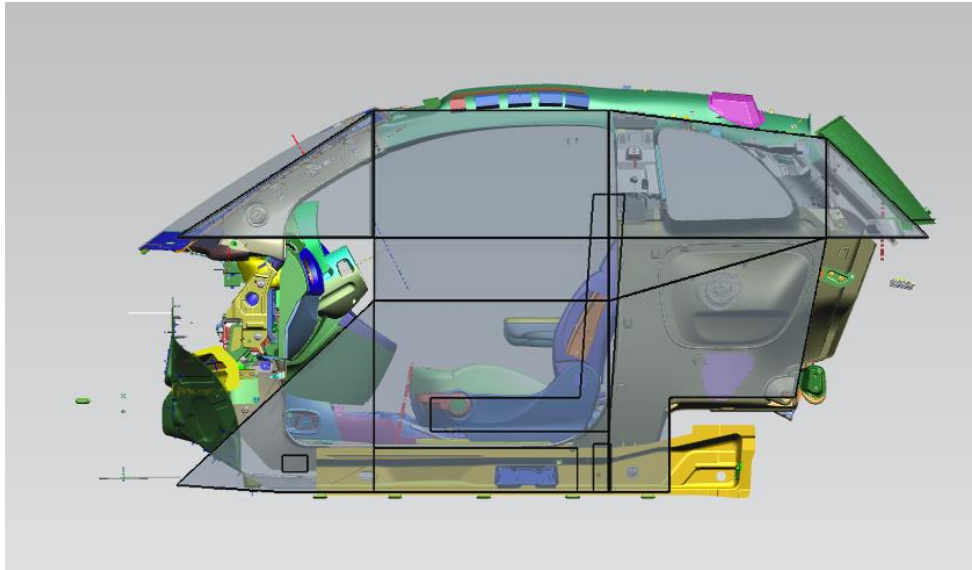
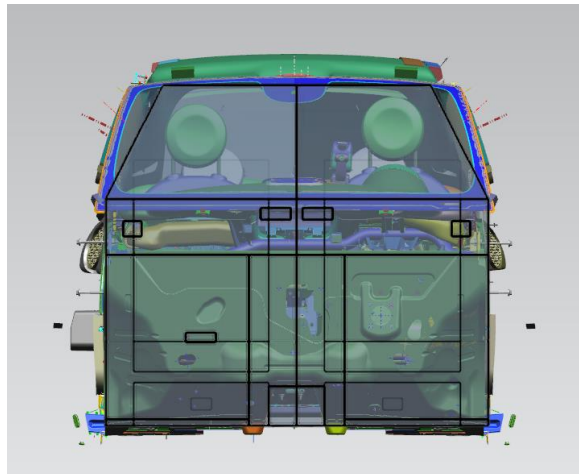


Fig. 4. 8: Dimensions required to parametrize the CAD geometry: external dimensions of the car cabin on the left; dimensions of the seats on the right.

The divisions of the cabin volume in different zone is fixed and, therefore, also the basic shape of the virtual geometry is predetermined. This means that there is a lack of customization of the three-dimensional environment, which could cause problems in meeting the user's necessities. However, since the geometry is being modelled simultaneously in Amesim and STAR-CCM+, giving the chance to further personalize the cabin shape would increase excessively the complexity of the tool. The first step is then to choose the appropriate dimensions of the simplified virtual geometry in order to closely match the actual cabin environment. The required data have been selected measuring the CAD of the Fiat 500e trying to achieve the best possible fit between the two geometries, as it is shown in Figs. 4.9 and 4.10. A troublesome point, for example, has been the selection of the value of the dashboard depth, which also determines, in the virtual geometry, the length of the windshield. However, in the real cabin of the car there is no correspondence between these two points. As it can be seen in Fig. 4.10, priority has been given to the correct definition of the dimensions of the windshield with respect to the ones of the dashboards, according to the belief that their impact on the simulation results would have been higher.



*Fig. 4. 9: Side view of the match between the virtual shape and the cabin CAD to extrapolate the measurements needed in the geometry definition.*



*Fig. 4. 10: Front view of the match between the virtual shape and the cabin CAD to extrapolate the measurements needed in the geometry definition.*

Once the main CAD geometry has been refined, it is necessary to provide the thickness of the external surfaces of the cabin. These surfaces are usually composed by multiple layers of different materials. In the tool, the roof and the side panels are characterized as three-layers components composed of insulation material (canvas for the roof and interior trim for the side panels), air gap and metal sheet. The last class of surfaces to be defined are the glasses (windshield and side windows) which, in the interface of the tool provided by Amesim are all characterized with the same parameters even if usually there are important differences between them. However, it is possible to bypass this limitation manually changing the desired values inside the supercomponent of the Embedded CFD Tool (ECFD). Therefore, in the geometry interface of ECFD application, the value of the side windows

has been inserted under the heading glass thickness, and it has been manually modified in the windshield inputs inside the supercomponent. The last set of data required to complete the geometry definition section of the model regards the air vents: the position of the center of the vents in the relative volumes, and the height and width of the air vent ports noting that, as explained in the paragraph 4.3.1, the air vents used in the test considered are only the top front. According to this, the information regarding all the other vents have been neglected, since they do not affect the simulation. Each air vent is bound to its original zone and the user is not allowed to move it into a different region. Although, it is unlikely to be an issue with the main air ports, it could represent a problem with the position of the recirculation port since it might be placed in a different position in the vehicle considered.

### **4.3.3 Material Characterization**

The tool interface requires the definition of five different materials used in the cabin environment: metal sheets, glass, canvas in the roof, interior trim in the side panels and seat foam. In this section, the same consideration presented in the paragraph 4.3.2 regarding the differences between windshield and side windows has been implemented. A common windshield produced for automotive purposes is usually composed of two external layers of glass which, in the event of breaking are held in place by an interlayer of polyvinyl butyral (PVB) or ethylene-vinyl acetate (EVA) hence, the windshield is composed of three layers. Therefore, its thermophysical properties will be different with respect to the ones of the side glass, which consist of a single layer of glass meant to shatter into tiny pieces in case of impact. A separate material card has been created to characterize the windshield material and its index number has been manually inserted in the supercomponent of the ECFD tool as it was done for the thickness. The data needed to completely define a material card in this model are density, specific heat and thermal conductivity. Furthermore, it is necessary to set the radiative exchange properties of the materials of the external surfaces exposed to sun rays: emissivity, absorption factor and transmission factor for both steel and windshield glass. The value of all these properties has been determined using FCA data.

### **4.3.4 Stopping Criterion**

The coupling principle between Amesim and STAR-CCM+ has been explained in paragraph 4.2 and it has been pointed out that a critical step is represented by the choice of the criterion that regulates the update of the boundary conditions provided by CFD calculations. The approach selected consists of defining the time intervals between the update iterations. The length of this intervals is not fixed and it follows a nearly exponential curve, which resets at every switch of the vehicle speed. In this

way, a higher number of updates will be performed in correspondence of important changes in the experimental set up. Figure 4.11 clearly shows the instants in which the simulation on Amesim is stopped to update the boundary condition, comparing their pattern with the profile of the vehicle speed, which is the main switching condition during the test.

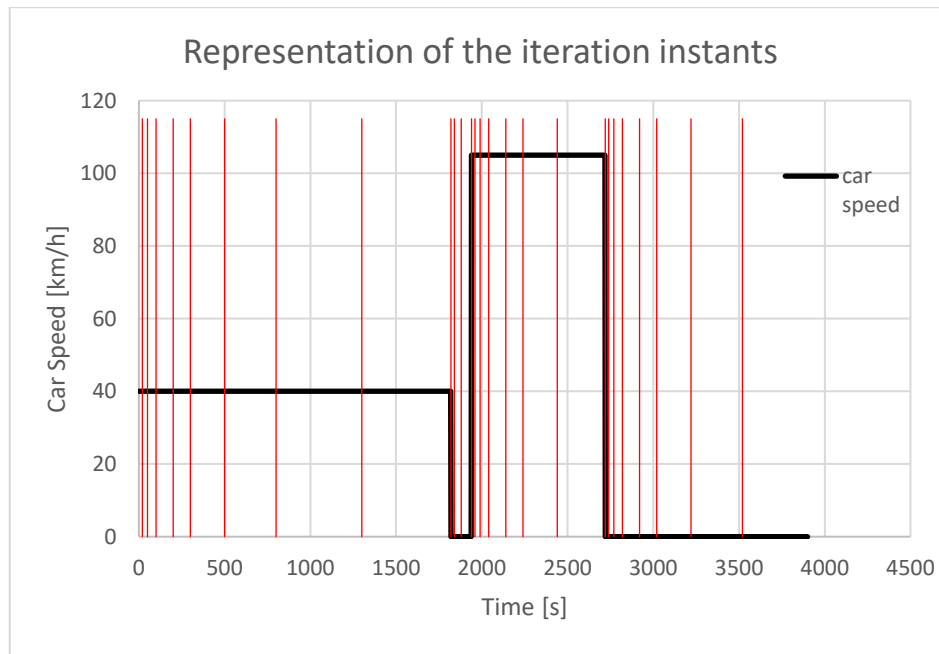


Fig. 4. 11: Instants (in red) at which the simulation on Amesim stops and asks to STAR-CCM+ for an update on the boundary conditions, compared to the profile of the vehicle speed (in black).

It is important to outline the most significant direct consequences of the choice of the stopping criterion. On one hand, increasing the number of update iterations with CFD calculations should improve the accuracy of the result getting closer to an ideal result obtained with a continuous coupling. On the other hand, each iteration added to the simulation will increase the amount of time and computational resources required diminishing the advantages brought by 1D analysis. The goal is then to find a compromise to maximize the accuracy of the results minimizing the duration of the simulation. In order to decide which one was the most appropriate set of iterations to use, a sensitivity study has been performed. This analysis consists of multiple simulations of the same model executed with different choices of profiles for the stopping criterion, starting with relaxed profiles and progressively tightening them. When increasing the number of updates there are no significant changes in the values obtained, the chosen profile can be considered appropriate.

#### 4.3.5 Results cleaning

In the output collections of the values of the variables each instant is printed multiple times with a discontinuous pattern; therefore, the results obtained need to be “cleaned” before being ready to be

post-processed and analyzed. This has been achieved with the Matlab script provide below, which reads the values in the first column (reserved for the time variable) one at a time and prints the related row only if it recognizes a different value with respect to previous one.

```
%post-processing for Embedded CFD tool results
%script to eliminate multiple rows repeated

D=dataset('file','Soaking_patchalt4_unprocessed.txt'); %every column is a
different variable, the first has to be TIME
F=double(D);
flag=-1;
cleaned=fopen('Soaking_patchalt4_precessed.txt','w');

for i=1:length(F);
    if flag~=F(i,1);
        fprintf(cleaned,'%0.8f %0.8f %0.8f %0.8f %0.8f %0.8f %0.8f %0.8f %0.8f %0.8f
%0.8f\r\n',F(i,:)); %be sure to define the correct number of columns
    end
    flag=F(i,1);
end

fclose(cleaned);
```

#### 4.3.6 First simulation

This first version of the model is completed and ready to be simulated. The results obtained for the average temperature of the air in each volume have been compared with the measurements of the thermocouples present in the vehicle. The following list shows the correspondence between zones and thermocouples:

- Top Front Left (TFL) – Head Front Left
- Top Front Right (TFR) – Head Front right
- Top Rear Left (TRL) – Head Rear Left
- Top Rear Right (TRR) – Head Rear Right
- Bottom Front Left (BFL) – Feet Front Driver Left, Feet Front Driver Right
- Bottom Front Right (BFR) – Feet Front Passenger Left, Feet Front Passenger Right
- Bottom Rear Left (BRL) – Feet Rear Passenger Left
- Bottom Rear right (BRR) – Feet Rear Passenger Left

The abbreviations will help in identifying the different zones in this chapter. The BFL and BFR zones are related to two thermocouples each, which represent the temperatures at each foot position. The deviation of the numerical results will be calculated with respect to the average one between the two thermocouples. Furthermore, the windshield (WS) and rearshield (RS) zones do not appear in the list

because they cannot be related to any thermocouple, since the company is not interested in those values. As it is shown in Figs. 4.12 and 4.13, the results obtained for the top zones (TFL and TFR in the graphs) are really close to the experimental ones. However, the bottoms zones instead present an abnormal behavior in the first 50 seconds of the simulation. Taking as example the graphs (BRL) shown in Fig. 4.14, an unexpected peak of about 15 degrees is noticeable. This behavior has been associated with an inaccurate initialization of the model.

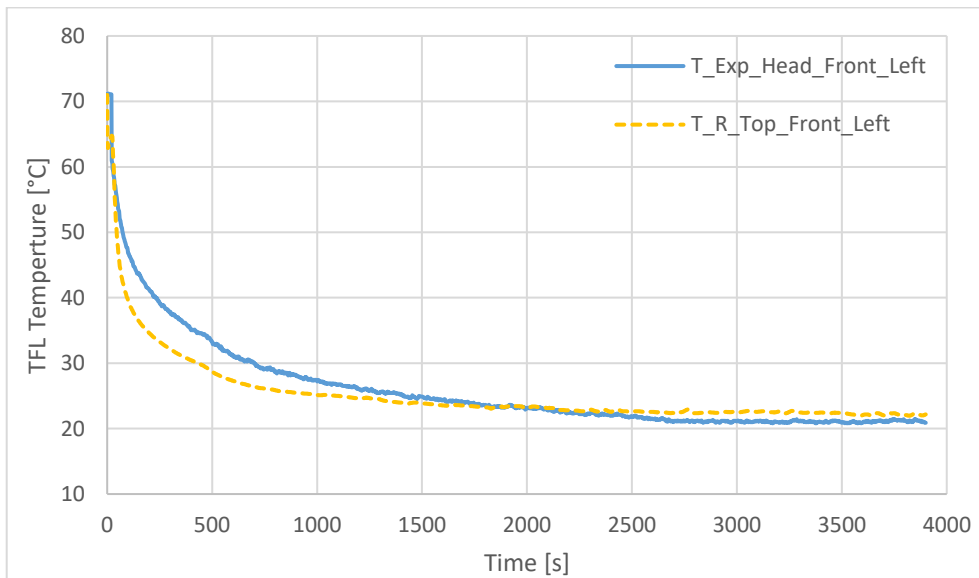


Fig. 4. 12: Comparison between the experimental values measured from the thermocouple Head Front Left and the numerical results obtained for the zone Top Front Left (TFL) in the first simulation.

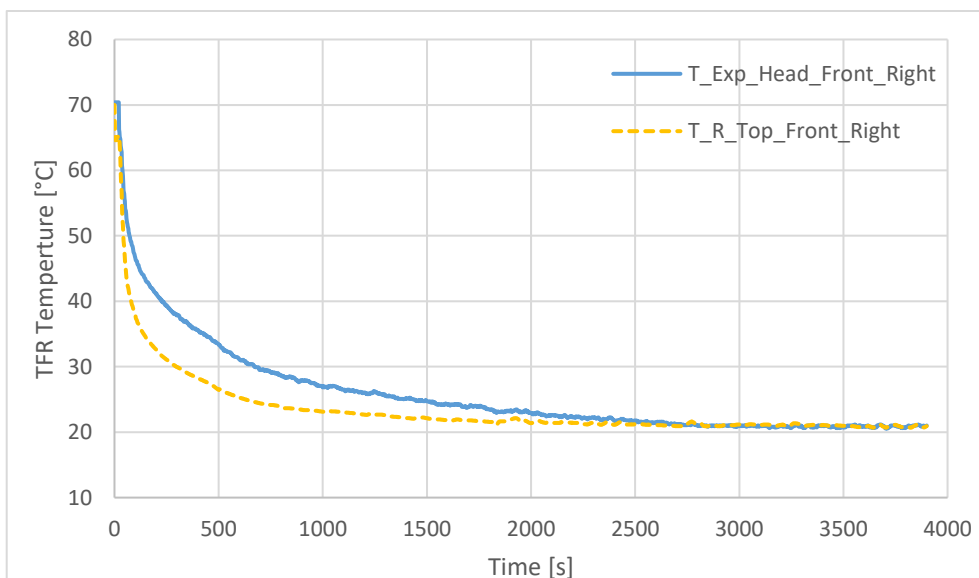


Fig. 4. 13: Comparison between the experimental values measured from the thermocouple Head Front Right and the numerical results obtained for the zone Top Front Right (TFR) in the first simulation.

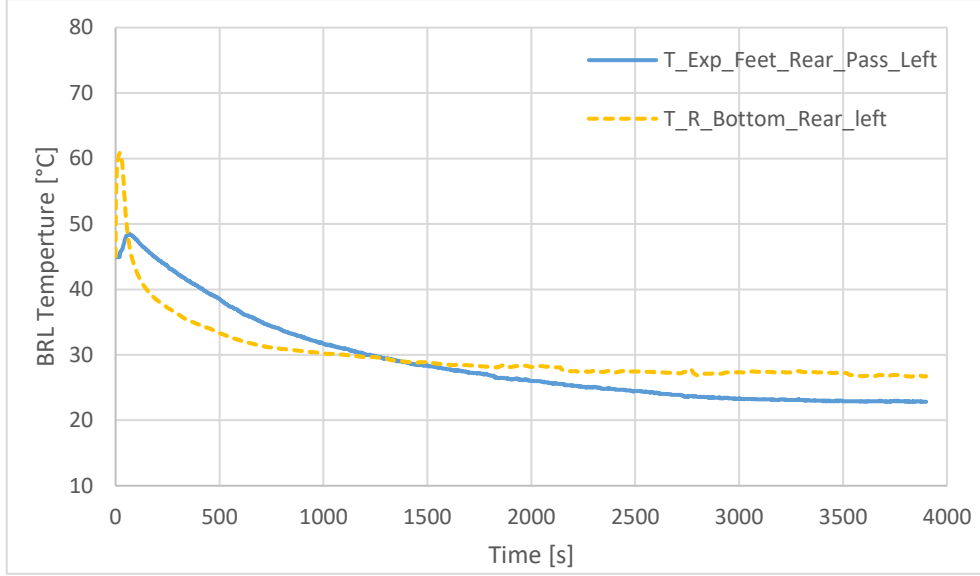


Fig. 4. 14: Comparison between the experimental values measured from the thermocouple Feet Rear Passenger Left and the numerical results obtained for the zone Bottom Rear Left (BRL) in the first simulation.

Validation metric and cumulative average error were evaluated as explained in paragraph 2.6.3 using Eq. 2.8 and Eq. 2.9 [68] and the obtained values are tabulated in Table 4.1

$$V = 1 - \frac{1}{t_{end} - t_0} \sum_{i=t_0}^{t_{end}} \tanh \left| \frac{y(t_i) - Y(t_i)}{Y(t_i)} \right| \quad (8)$$

$$err = \frac{1}{t_{end} - t_0} \sum_{i=t_0}^{t_{end}} \left| \frac{y(t_i) - Y(t_i)}{Y(t_i)} \right| \quad (9)$$

<b>PARAMETER</b>	<b>V</b>	<b>err</b>
<i>Top Front Left</i>	96.74%	3.27%
<i>Top Front Right</i>	95.97%	4.07%
<i>Top Rear Left</i>	92.19%	7.93%
<i>Top Rear Right</i>	90.81%	9.41%
<i>Bottom Front Left</i>	95.58%	4.45%
<i>Bottom Front Right</i>	92.51%	7.57%
<i>Bottom Rear Left</i>	94.49%	5.55%
<i>Bottom Rear Right</i>	93.72%	6.35%
<i>Recirculation</i>	89.69%	10.50%

Table 4. 1: Values of the validation metric and of the cumulative average error for the validation for the temperature of the 8 main volumes of the cabin and for the temperature of the recirculation air for the first simulation.

Even considering the irregularities caused by the initialization chosen, the results for the validation metric obtained are higher than expected. The lower validation metric calculated is related to the recirculation temperature. This value, which can still be considered satisfactorily, can be explained by the fact that while the thermocouple measures the temperature of the air at the start of the recirculation, the value calculated by the model corresponds with the average temperature of the air of the volume in which the duct port is placed. As a direct consequence, the accuracy of the recirculation air temperature calculation is strongly limited. Furthermore, taking into account the considerations moved in paragraph 4.3.2 regarding the position definition of air vents, it becomes evident that the model is not suited to evaluate the temperature of a precise point as the start of the recirculation duct. This statement is consistent with the nature of the model built whose results are not provided by an accurate CFD simulation, but by a 1D calculation of average temperatures. However, this consideration on the recirculation temperature has been brought up because, in the event of a direct connection between the cabin model and the refrigeration loop model, this parameter would play a main role in the simulation. Since the test is performed in complete recirculation (100% of the air going through the evaporator is coming from the recirculation duct, while 0% is fresh air from the external environment), the temperature calculated at the recirculation port will be an important input for the AC system.

#### **4.3.7 Soaking Pre-simulation**

The condition in which a cool down experimental test is performed represents a possible, though extreme, situation in which general drivers could find themselves using the car after it was parked under the sun in a hot day of summer for several hours. Therefore, before performing the actual cool down experimental test, it is necessary to go through a preparation to reproduce these initial conditions. During this phase, the car is introduced in the wind tunnel, in which:

- the speed of the wind is null
- the temperature of the air is kept to 43.8 °C
- a solar radiation of 1000 W/m<sup>2</sup> is provided
- the vehicle is turned off and, therefore, the HVAC system is not in operation

This state persists until the average temperature of the air inside the cabin of the vehicle reaches 60 °C. Once this condition is achieved, the vehicle and the wind tunnel are turned on and the cool down test is started. In order to eliminate the abnormal behavior of the temperature explained in the previous paragraph and to improve the initialization of the simulation, a soaking pre-simulation has been performed. The purpose of this operation is to reproduce the preparation of the conditions from which the cool down starts. This has been achieved by running a simulation in which the inputs provided to the model have been modified as following:

- the mass flow rate at each air vent is null (this operation is sufficient to eliminate every possible action of the HVAC system)
- the ambient temperature is constant and equal to 43.8 °C
- the speed of the vehicle is null

When the average of the temperatures calculated in all the 10 volumes has reached 60 °C, the simulation is stopped and this point is considered as initial point of the cool down simulation. The graph in Fig. 4.15 shows the behavior of the temperature in each zone during the soaking simulation.

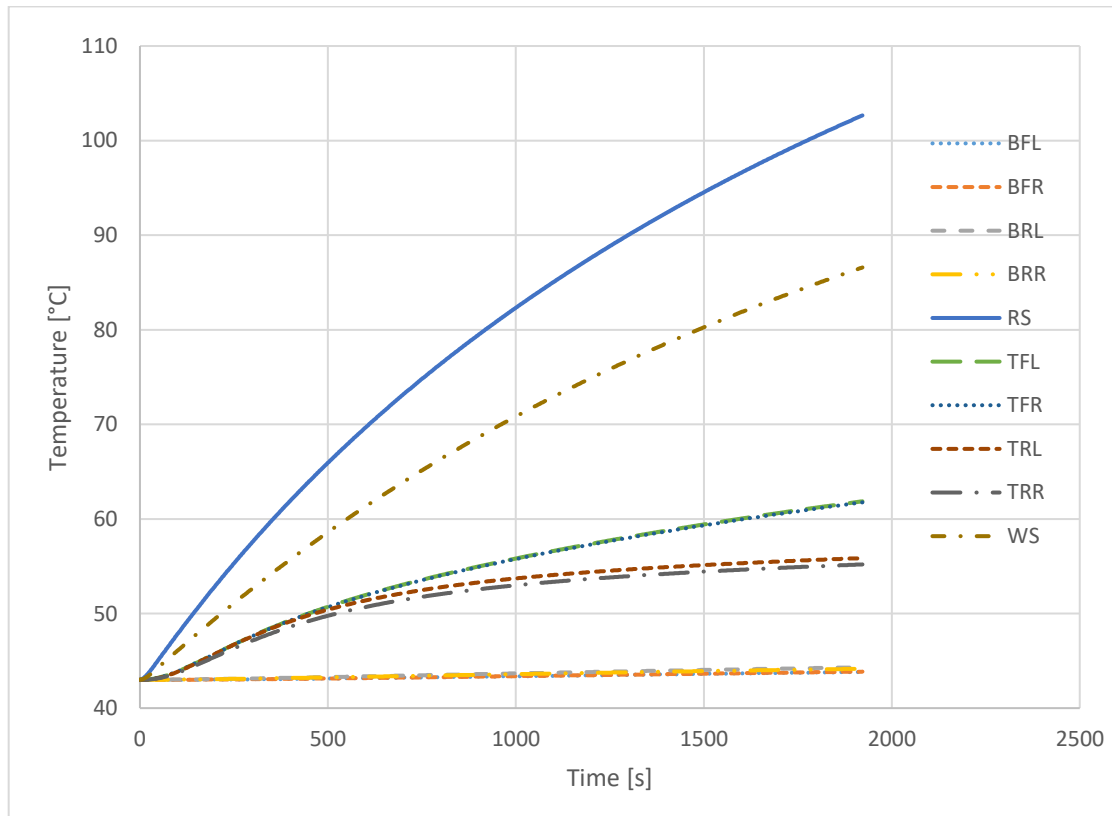


Fig. 4.15: Behavior of the temperature of the 10 volumes during the soaking simulation, at 1922 s the average temperature reaches 60 °C.

It is noticeable that during this phase the bottom zones are not affected by any significant change, while instead the temperature in the windshield and rearshield zones reaches excessive values. Furthermore, the temperature in the top zones is supposed to reach uniformly 70 °C, however, it was determined a temperature lower and significant differences between the temperatures in the top front zones and the ones in the top rear zones. The main reason behind this behavior has been identified in one setting of the CFD simulation, which is in charge to provide the evaluation of the mass flow air and the heat transfer coefficient at the interface between the volumes. In fact, the simulation in STAR-CCM+ is performed without considering the action of the gravity. Therefore, the model is unable to consider the effects of natural convection produced by the variations of density of the air.

During the soaking of the vehicle, the HVAC system is not in operation and the air vents are not providing any mass flow air, hence the main and only source of mass flow air is represented by the natural convection. This explains the high differences in the values of the average temperatures of the various zones, since their interactions are limited by the absence of flow of air. However, this pre-simulation has been added at the beginning of the cool down simulation and in this way, a single run all the process (soaking + cool down test) has been reproduced with continuity.

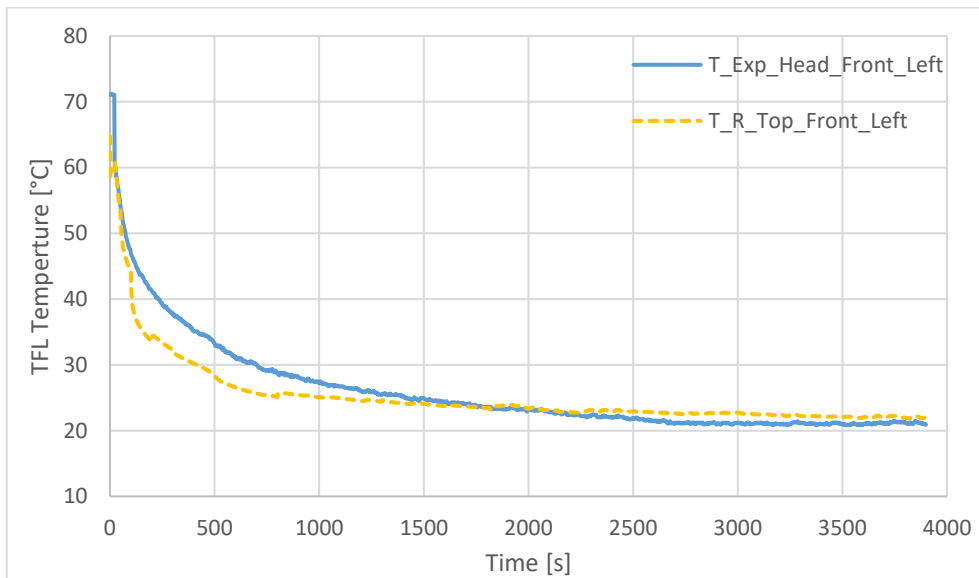


Fig. 4. 16: Comparison between the experimental values measured from the thermocouple Head Front Left and the numerical results obtained for the zone Top Front Left (TFL) in the second simulation.

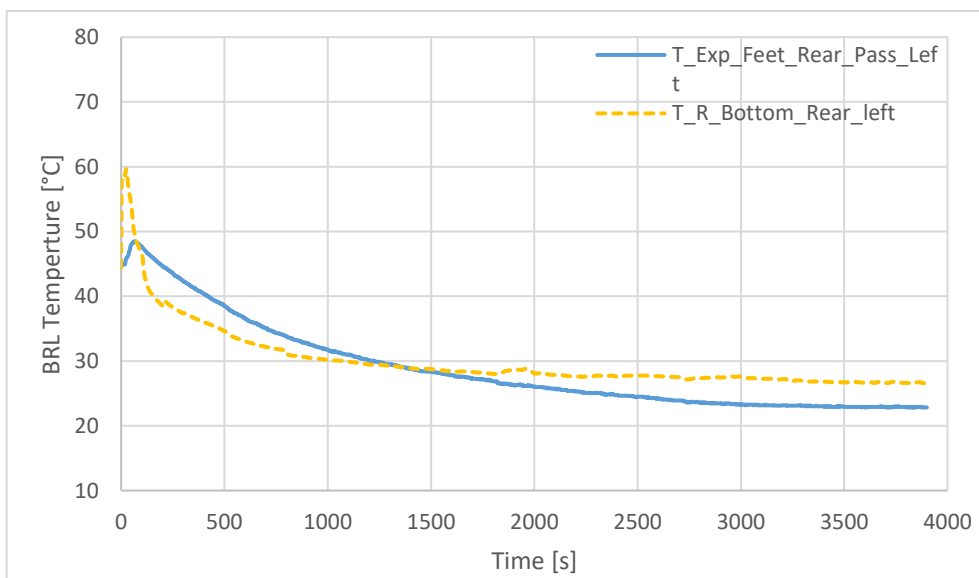


Fig. 4. 17: Comparison between the experimental values measured from the thermocouple Feet Rear Passenger Left and the numerical results obtained for the zone Bottom Rear Left (BRL) in the second simulation.

<i>PARAMETER</i>	<i>V</i>	<i>err</i>
<i>Top Front Left</i>	96.67%	3.34%
<i>Top Front Right</i>	96.57%	3.44%
<i>Top Rear Left</i>	92.74%	7.37%
<i>Top Rear Right</i>	90.23%	9.96%
<i>Bottom Front Left</i>	95.96%	4.07%
<i>Bottom Front Right</i>	93.49%	6.56%
<i>Bottom Rear Left</i>	94.75%	5.28%
<i>Bottom Rear Right</i>	94.01%	5.95%
<i>Recirculation</i>	90.58%	9.55%

*Table 4. 2: Values of the validation metric and of the cumulative average error for the validation for the temperature of the 8 main volumes of the cabin and for the temperature of the recirculation air for the second simulation.*

As it is shown in Figs. 4.16 and 4.17 and in Table 4.2, performing the initialization of the model by simulating the soaking of the vehicle has been beneficial overall. The highest improvements, even if limited, have been registered for the bottom zones, which benefits of a better initialization and the unexpected peak outlined in paragraph 4.3.6 is still present but it has been slightly reduced. The only two zones presenting a slightly lower value of the validation metric are Top Front Left (validation metric diminished of 0.07%) and Top Rear Right (validation metric diminished of 0.58%).

#### **4.4 Simulations with Gravity Enabled**

After discussing the issues encountered during the soaking pre-simulation and the cool down simulation with Siemens developers, an alternative java scripts of the command execution of the Embedded CFD Tool was developed in order to be able to change the settings in the CFD simulation, which cannot be defined in the interface in Amesim. It is sufficient to replace the execute command script in the Amesim installation folder and perform the generation of the geometry and of the physics in order to apply the modifications. Hence, it was possible to explore the possibilities of the model and experiment the different settings as presented in the following sub-sections.

##### **4.4.1 Third Simulation**

The first change made to the settings of the CFD simulation has been the enabling of the gravity in order to consider the natural convection of the air inside the cabin. Therefore, a third simulation has been performed reproducing the soaking and the cool down. Prior to running the complete

simulation, it is important to perform a soaking separately in order to determine the instant where the average temperature inside the vehicle reaches 60 °C. In this case, the duration of the soaking stage is 1706 Seconds. In Fig. 4.18 the comparison between experimental and numerical results is shown.

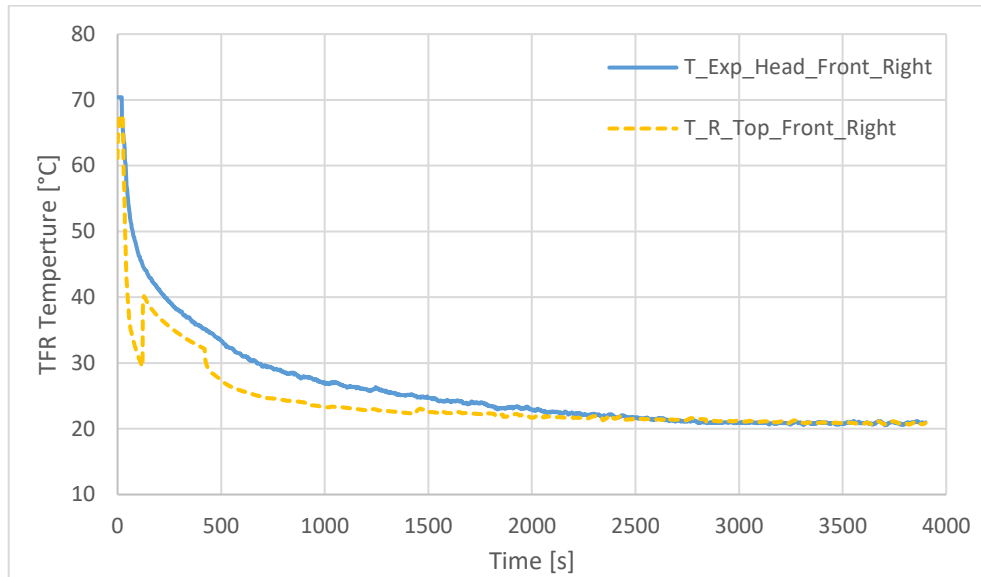


*Fig. 4. 18: Comparison between the experimental values measured from the thermocouple Head Front Right and the numerical results obtained for the zone Top Front Right (TFR) in the first attempt of the third simulation.*

From the behavior of the numerical results, it is evident that the first consequence of enabling gravity in the model has been a higher sensitivity to the stopping criterion regulating the coupling mechanism. Therefore, the number of stops in first 500 seconds of the simulation has been increased in order to update the boundary conditions with an adequate frequency, as it is shown in Fig. 4.19. A new simulation is performed according to this new stopping pattern. Figures 4.20 and 4.21 present respectively the result of Top Front Left and Bottom Rear Left zones, chosen as examples, while Table 4.3 collects the values of the validation metric and of the cumulative average error for each zone calculated applying Eq. 2.8 and Eq. 2.9.

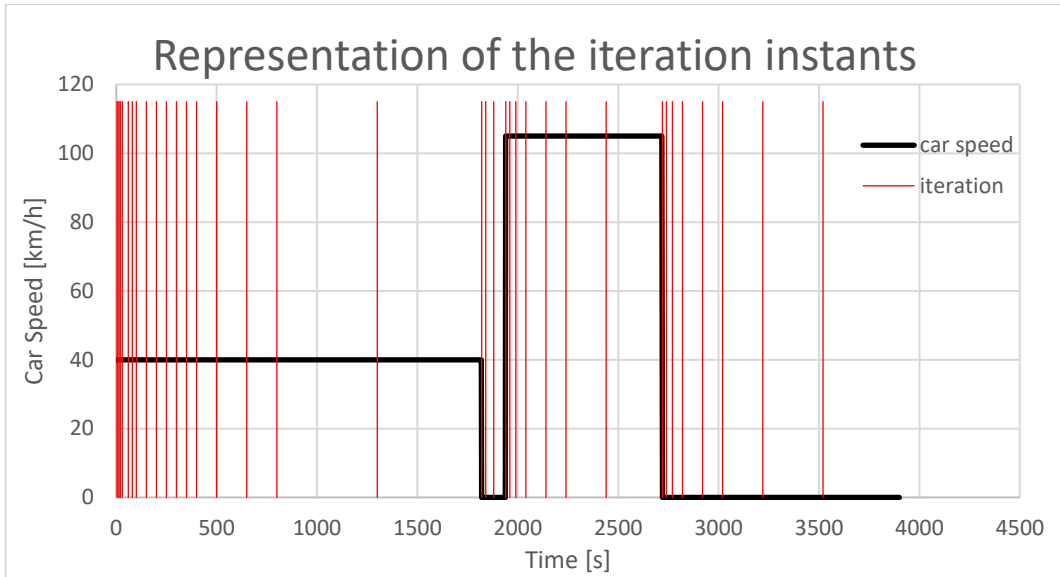


Fig. 4. 19: Instants (in red) at which the simulation on Amesim stops and asks to STAR-CCM+ for an update on the boundary conditions, compared to the profile of the vehicle speed (in black).

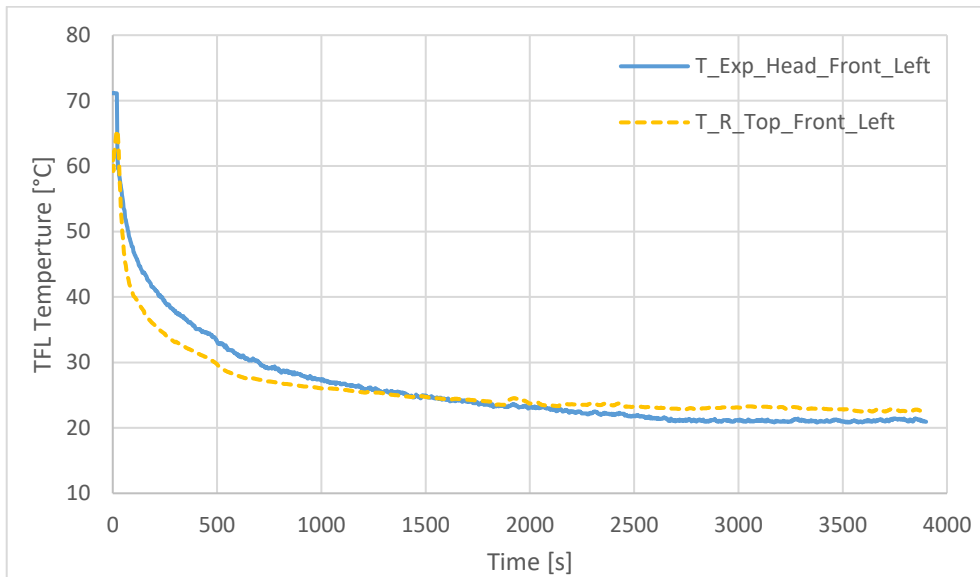


Fig. 4. 20: Comparison between the experimental values measured from the thermocouple Head Front Left and the numerical results obtained for the zone Top Front Left (TFL) in the third simulation.

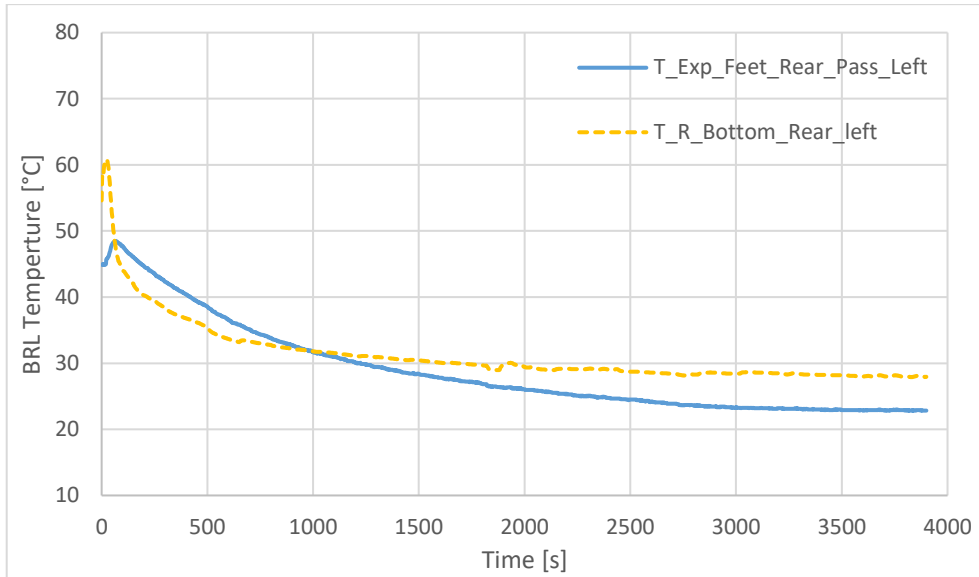


Fig. 4. 21: Comparison between the experimental values measured from the thermocouple Feet Rear Passenger Left and the numerical results obtained for the zone Bottom Rear Left (BRL) in the third simulation.

<i>PARAMETER</i>	<i>V</i>	<i>err</i>
<i>Top Front Left</i>	96.66%	3.35%
<i>Top Front Right</i>	96.56%	3.46%
<i>Top Rear Left</i>	90.42%	9.78%
<i>Top Rear Right</i>	90.28%	9.94%
<i>Bottom Front Left</i>	96.28%	3.74%
<i>Bottom Front Right</i>	93.38%	6.68%
<i>Bottom Rear Left</i>	93.34%	6.74%
<i>Bottom Rear Right</i>	93.11%	6.97%
<i>Recirculation</i>	90.48%	9.67%

Table 4. 3: Values of the validation metric and of the cumulative average error for the validation for the temperature of the 8 main volumes of the cabin and for the temperature of the recirculation air for the third simulation.

The new stopping criterion adopted solved the issues generated by the increased sensitivity to duration of the intervals between different iterations. However, even if under a theoretical point of view introducing the gravity effect in the calculation represents a great step forward, there are not significant changes in the results. It is worth to notice a decrease in the validation metric of all the rear zones due to a lower accuracy in the prediction of the steady-state temperature reached in those volumes of the cabin. The most significant effects of the introduction of gravity can be found in the results produced by the soaking simulation, since natural convection is the only source of mass flow air between volumes. Comparing Figs. 4.15 and 4.22, the following can be made:

- The temperatures reached in the windshield and rearshield have decreased of 20 °C and are now more similar adjoining top zones
- There is higher uniformity between the temperatures of the top zones, while before there was a significant difference between the front zones and the rear ones
- The increase in the bottom zones temperature is about 10 °C, while before was almost negligible
- The soaking simulation is highly sensitive to the stopping criterion; the number of updates required in order to obtain smooth curves not affected by the coupling mechanism of the Embedded CFD tool is too high.

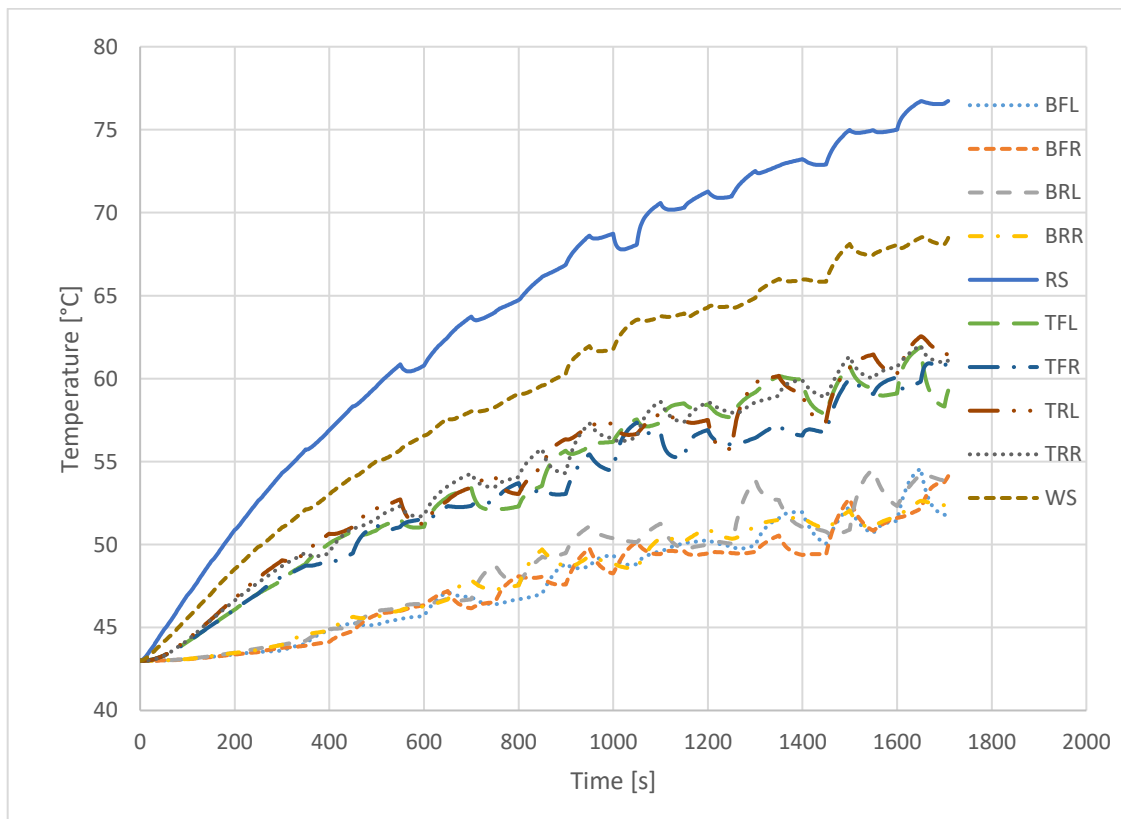


*Fig. 4. 22: Behavior of the temperature of the 10 volumes during the soaking simulation, at 1708 s the average temperature reaches 60 °C.*

#### 4.4.2 Fourth simulation

In all simulations performed so far the heat transfer coefficient in the CFD simulation is the local heat transfer coefficient, which can be highly sensitive to the mesh size adopted. The mesh used in the Embedded CFD tool is automatically generated by the software in the physics section of the tool, allowing the user to select the average mesh size. Furthermore, in this research the focus is not on the effects of the average size of the mesh. Therefore, the local heat transfer coefficient might not be

the most accurate hence introducing an inaccuracy to the simulation. Following the same procedure explained in the previous paragraph, a new execute command script has been used in which the gravity and the specified  $y^+$  heat transfer coefficient has been chosen. This choice combines the best features of the heat transfer coefficient and the local heat transfer coefficient eliminating the sensitivity to near-wall mesh size. A final simulation has been performed to make a comparison between the results obtained with this alternative heat transfer coefficient. The sensitivity of the simulation to the stopping criterion is definitively lower with respect the previous one, since it is possible to use the first pattern created, shown in Fig. 4.11, obtaining quite satisfactory results.

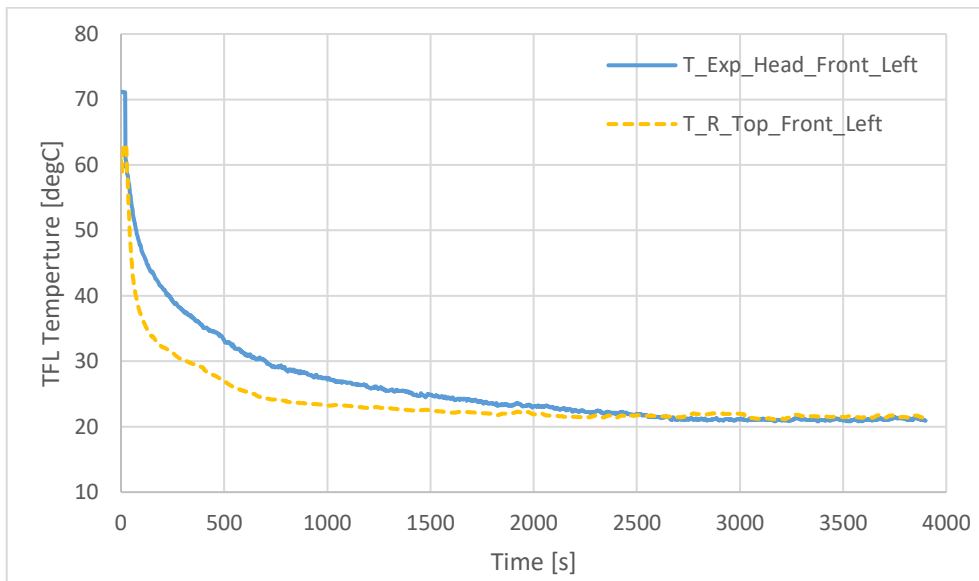


Fig. 4. 23: Comparison between the experimental values measured from the thermocouple Head Front Left and the numerical results obtained for the zone Top Front Left (TFL) in the fourth simulation.

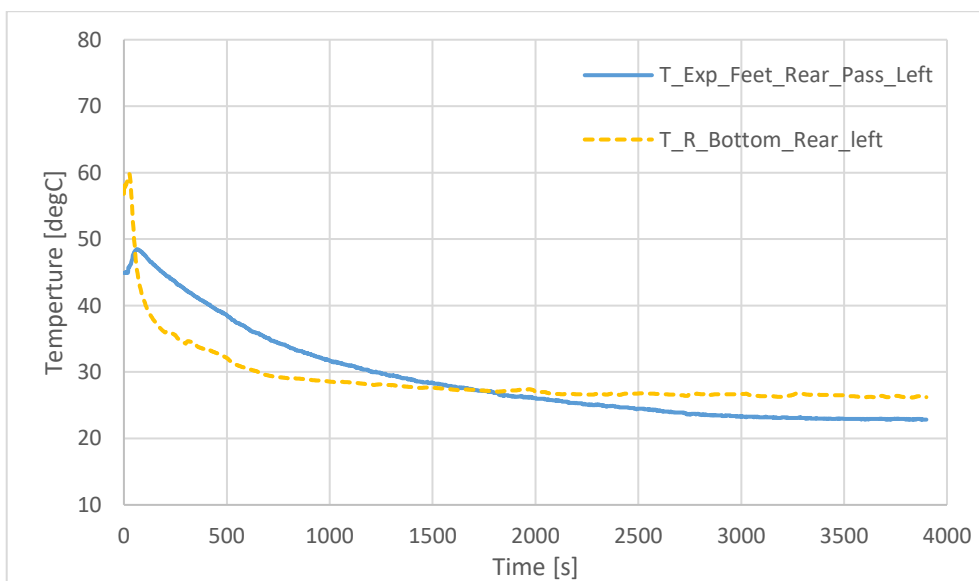


Fig. 4. 24: Comparison between the experimental values measured from the thermocouple Feet Rear Passenger Left and the numerical results obtained for the zone Bottom Rear Left (BRL) in the fourth simulation.

However, to obtain more accurate results, the simulation was performed using the last stopping pattern shown in Fig. 4.19. Figures 4.23 and 4.24 present respectively the result of Top Front Left and Bottom Rear Left zones, chosen as examples, while Table 4.4 collects the values of the validation metric and of the cumulative average error for each zone calculated applying Eq. 2.8 and Eq. 2.9.

<i>PARAMETER</i>	<i>V</i>	<i>err</i>
<i>Top Front Left</i>	95.87%	4.17%
<i>Top Front Right</i>	93.74%	6.33%
<i>Top Rear Left</i>	93.44%	6.63%
<i>Top Rear Right</i>	93.39%	6.68%
<i>Bottom Front Left</i>	93.11%	6.97%
<i>Bottom Front Right</i>	90.19%	9.99%
<i>Bottom Rear Left</i>	94.63%	5.41%
<i>Bottom Rear Right</i>	94.39%	5.66%
<i>Recirculation</i>	87.58%	12.74%

*Table 4. 4: Values of the validation metric and of the cumulative average error for the validation for the temperature of the 8 main volumes of the cabin and for the temperature of the recirculation air for the fourth simulation.*

By comparing Tables 4.3 and 4.4 an evident trend is noticed. While the correlation between numerical results and experimental data has improved significantly in the rear zones (TRL +3.02%, TRR +3.11%, BRL +1.29%, BRR +1.28%), it has decreased for the front zones (TFL -0.79%, TFR -2.82%, BFL -3.17%, BFR -3.19%). According to this, the validation metric evaluated for the temperature of the air recirculated has decreased, since it depends on the temperature of the BFR zone.

## **Chapter 5 – Conclusions and Future Work**

This chapter collects all the considerations and conclusions developed during the research project. Furthermore, suggestions for future studies that could not be exhaustively considered in this project are provided.

### **5.1 Heat Pump Model**

At the beginning of the modelling phase addressed in Section 3.3, two different approaches to design the heat pump system were identified. In order to remain consistent with the scope of the research (provide an overview of the potential of the application of a heat pump system for electric vehicles using 1D models), a pragmatic approach has been selected. However, the results obtained while building the model of the system demonstrated that the lack of components data is one of the greatest obstacles. Hence, assumptions had to be made while defining the thermodynamic behavior of the external evaporator and this led to a weak characterization of the component. Furthermore, designing the new condenser using the information already available based on the condenser used in the refrigeration system produced a system unable to work in harmony: on one hand, the refrigerant mass flow rate required to obtain the desired overheat at the end of the evaporator is low and it determines an excessive increase in pressure and temperature in the condenser which leads to an exaggerated subcooling at the end of the condenser; on the other hand, the mass flow rate required to properly operate the condenser does not allow the evaporator to completely vaporize the refrigerant. Finally, another important issue encountered is the electronic control of the expansion valve. The system considered proved to be very sensitive to refrigerant mass flow rate changes, therefore, an accurate and precise control is needed to stabilize the behavior of the system.

The first step to favor the approach to heat pump modelling in this situation was a study of the performance of the external heat exchanger. In order to understand its thermodynamic behavior while working as an evaporator instead of as a condenser it is necessary to perform experimental tests, which would provide the data necessary to calibrate its performance and correctly model the component. However, even doing so, information regarding the internal condenser would still be missing, hence there would still be the chance of obtaining poor match between the two heat exchangers. Therefore, it is recommended to proceed following a different methodology as proposed in Section 3.3, which is a more theoretical approach that is helpful in providing the missing information needed to overcome the obstacles encountered in this research. It consists of an iterative process meant to design a thermodynamic cycle of the heat pump system on the pressure vs. enthalpy diagram according to Eq. 3.1, assuming an initial mass flow rate. After having designed the desired thermodynamic cycle according to the characteristics of the components already present in

the system, there would be enough information to contact a supplier and find the best solution for the missing components. At this point, the main obstacle highlighted in this project would be solved and it could be now possible to correctly model the system.

## 5.2 Cabin Model

The vehicle cool down process has been simulated on the cabin model multiple times analyzing the impact of different settings. First, the effect of performing a soaking simulation to assess the initial conditions of the cool down test against manually selecting the initialization parameters for temperature and mass flow rate was examined. This analysis demonstrated an improvement in the results obtained in the validation and a mild correction of the transient behavior of the model, especially in the bottom zones. Second, the impact of considering the gravity effect in the simulation has been analyzed. Even if under a theoretical point of view adding the gravity to the simulation represents an important improvement in the mathematical and physical modelling of reality, there were no significant changes in the results obtained in the validation of the model. However, the consequences of the introduction of gravity are evident in the soaking simulation, where natural convection is the only source of air mass flow rate. In order to understand how this setting improves the reliability of the simulation, it would be necessary to record the temperatures of the air measured by the different thermocouples also during the soaking of the vehicle and not only during the actual cool down test. In this way it would be possible to perform a validation of the soaking simulation too. Finally, the last setting that has been examined is the choice of the heat transfer coefficient in STAR-CCM+. The third simulation has been performed considering the local heat transfer coefficient, while the fourth one uses the specified  $y^+$  heat transfer coefficient. The results obtained in the validation showed that the third simulation obtained a higher match with the experimental data for the front zones, while the fourth simulation better represented the behavior of the temperature in the rear zones. However, the use of the local heat transfer coefficient also produced a higher sensitivity to the stopping criterion adopted requiring a higher number of stops and interactions between the 1D and the 3D software, which reflects on a longer time required compute a stable simulation. Figure 4. 22 shows clearly the oscillation in the results produced by this sensitivity.

It is important to state that the thermocouples used to measure the values used for the model validation record the temperature of a specific point of the cabin environment, while the aim of the model created is to calculate the average temperature of a certain volume of the cabin. This means that a perfect match between numerical results and experimental data cannot be expected. In order to provide a solid validation of this model, it would be necessary to increase the number of thermocouples in the vehicle and calculate an average of the temperature measured in each zone.

In light of this, the Embedded CFD tool can be considered a good instrument to provide a fairly accurate prediction of the distribution of the temperature inside the cabin without requiring complex and expensive CFD simulations.

### **5.3 Future work**

For future work it is recommended to perform a sensitivity analysis of the model to the average size of the mesh, defined in the physic section. This should be done considering both the local heat transfer coefficient, which is expected to be more likely to be affected by this parameter, and the specified  $y^+$  heat transfer coefficient.

Furthermore, an interesting development is the chance of directly connecting the HVAC system (in this case the refrigeration system modelled in Chapter 2) to this model and perform a complete simulation. In this scenario, the recirculation port of the Embedded CFD tool and the outlet of the evaporator air acquire a great importance. In Chapter 4, it has been demonstrated that the output provided by the recirculation port is one of the weakest aspects of the entire model. The main reason of this is represented by the fact that, as previously explained, the aim of this model is not to evaluate the temperature of a specific point but the average temperature of a volume. Therefore, before being able to connect refrigeration system and cabin models, it is necessary to solve or at least moderate this issue. Furthermore, it would be necessary to model the ducts in charge of delivering the recirculated air from the cabin to the evaporator and the conditioned air from the evaporator to air vent ports.

## References

- [1] M. Hosoz and M. Direk, "Performance evaluation of an integrated automotive air conditioning and heat pump system," *Energy Convers. Manag.*, vol. 47, no. 5, pp. 545–559, Mar. 2006.
- [2] NASA, "Carbon Dioxide," *Climate.nasa.gov*. [Online]. Available: <https://climate.nasa.gov/vital-signs/carbon-dioxide/>.
- [3] M. Frondel, C. M. Schmidt, and C. Vance, "A regression on climate policy: The European Commission's legislation to reduce CO<sub>2</sub> emissions from automobiles," *Transp. Res. Part Policy Pract.*, vol. 45, no. 10, pp. 1043–1051, Dec. 2011.
- [4] European Commission, "Reducing CO<sub>2</sub> emissions from passenger cars." [Online]. Available: [https://ec.europa.eu/clima/policies/transport/vehicles/cars\\_en](https://ec.europa.eu/clima/policies/transport/vehicles/cars_en).
- [5] R. Alvarez and M. Weilenmann, "Effect of low ambient temperature on fuel consumption and pollutant and CO<sub>2</sub> emissions of hybrid electric vehicles in real-world conditions," *Fuel*, vol. 97, pp. 119–124, Jul. 2012.
- [6] R. T. Doucette and M. D. McCulloch, "Modeling the prospects of plug-in hybrid electric vehicles to reduce CO<sub>2</sub> emissions," *Appl. Energy*, vol. 88, no. 7, pp. 2315–2323, Jul. 2011.
- [7] A. Lajunen, "Energy Efficiency and Performance of Cabin Thermal Management in Electric Vehicles," presented at the WCX™ 17: SAE World Congress Experience, 2017.
- [8] J. Neubauer and E. Wood, "Thru-life impacts of driver aggression, climate, cabin thermal management, and battery thermal management on battery electric vehicle utility," *J. Power Sources*, vol. 259, pp. 262–275, Aug. 2014.
- [9] J. Jaguemont, L. Boulon, and Y. Dubé, "A comprehensive review of lithium-ion batteries used in hybrid and electric vehicles at cold temperatures," *Appl. Energy*, vol. 164, pp. 99–114, Feb. 2016.
- [10] G. E. Khoury and D. Clodic, "Method of Test and Measurements of Fuel Consumption Due to Air Conditioning Operation on the New Prius II Hybrid Vehicle," presented at the Vehicle Thermal Management Systems Conference & Exposition, 2005.
- [11] Y. Shin, S. Sim, and S. Kim, "Performance Characteristics of a Modularized and Integrated PTC Heating System for an Electric Vehicle," *Energies*, vol. 9, no. 1, p. 18, Dec. 2015.

- [12] R. Musat and E. Helerea, "Characteristics of the PTC Heater Used in Automotive HVAC Systems," in *Emerging Trends in Technological Innovation*, vol. 314, L. M. Camarinha-Matos, P. Pereira, and L. Ribeiro, Eds. Berlin, Heidelberg: Springer Berlin Heidelberg, 2010, pp. 461–468.
- [13] B. Torregrosa-Jaime, J. Paya, and J. M. Corberan, "Modelling of mobile air conditioning for electric vehicles," presented at the 4th European workshop MAC and vehicle thermal systems, Torino, Italy, 02-Dec-2011.
- [14] J. Meyer, G. Yang, and E. Papoulis, "R134a Heat Pump for Improved Passenger Comfort," presented at the SAE 2004 World Congress & Exhibition, 2004.
- [15] Q. Peng and Q. Du, "Progress in Heat Pump Air Conditioning Systems for Electric Vehicles—A Review," *Energies*, vol. 9, no. 4, p. 240, Mar. 2016.
- [16] Z. Qi, "Advances on air conditioning and heat pump system in electric vehicles – A review," *Renew. Sustain. Energy Rev.*, vol. 38, pp. 754–764, Oct. 2014.
- [17] K. J. Chua, S. K. Chou, and W. M. Yang, "Advances in heat pump systems: A review," *Appl. Energy*, vol. 87, no. 12, pp. 3611–3624, Dec. 2010.
- [18] T. Suzuki and K. Ishii, "Air Conditioning System for Electric Vehicle," presented at the International Congress & Exposition, 1996.
- [19] J. Dixon, *Modern diesel technology: heating, ventilation, air conditioning, & refrigeration*, 2nd edition. Clifton Park, NY: Delmar Cengage Learning, 2014.
- [20] M. Makino, N. Ogawa, Y. Abe, and Y. Fujiwara, "Automotive Air-conditioning Electrically Driven Compressor," presented at the SAE 2003 World Congress & Exhibition, 2003.
- [21] M. Naidu, T. W. Nehl, S. Gopalakrishnan, and L. Würth, "Electric Compressor Drive with Integrated Electronics for 42 V Automotive HVAC Systems," presented at the SAE 2005 World Congress & Exhibition, 2005.
- [22] R. Baumgart, J. Aurich, J. Ackermann, and C. Danzer, "Comparison and Evaluation of a New Innovative Drive Concept for the Air Conditioning Compressor of Electric Vehicles," SAE International, Warrendale, PA, 2015-26-0045, Jan. 2015.
- [23] M. Wei, H. Huang, P. Song, F. Peng, Z. Wang, and H. Zhang, "Experimental investigations of different compressors based electric vehicle heat pump air-conditioning systems in low

temperature environment,” in *2014 IEEE Conference and Expo Transportation Electrification Asia-Pacific (ITEC Asia-Pacific)*, Beijing, China, 2014, pp. 1–6.

- [24] D. Krahenbuhl, C. Zwysig, H. Weser, and J. W. Kolar, “A Miniature 500 000-r/min Electrically Driven Turbocompressor,” *IEEE Trans. Ind. Appl.*, vol. 46, no. 6, pp. 2459–2466, Nov. 2010.
- [25] R. W. Cummings and R. K. Shah, “Experimental Performance Evaluation of Automotive Air-Conditioning Heat Exchangers as Components and in Vehicle Systems,” presented at the Vehicle Thermal Management Systems Conference & Exposition, 2005.
- [26] Y. Han, Y. Liu, M. Li, and J. Huang, “A review of development of micro-channel heat exchanger applied in air-conditioning system,” *Energy Procedia*, vol. 14, pp. 148–153, 2012.
- [27] Z. Qi, Y. Zhao, and J. Chen, “Performance enhancement study of mobile air conditioning system using microchannel heat exchangers,” *Int. J. Refrig.*, vol. 33, no. 2, pp. 301–312, Mar. 2010.
- [28] J. H. Ahn, J. S. Lee, C. Baek, and Y. Kim, “Performance improvement of a dehumidifying heat pump using an additional waste heat source in electric vehicles with low occupancy,” *Energy*, vol. 115, pp. 67–75, Nov. 2016.
- [29] C. Kwon, M. S. Kim, Y. Choi, and M. S. Kim, “Performance evaluation of a vapor injection heat pump system for electric vehicles,” *Int. J. Refrig.*, vol. 74, pp. 138–150, Feb. 2017.
- [30] C. Kowsky, L. Leitzel, F. Oddi, and E. Wolfe, “Unitary HPAC System - Commercial Vehicle Applications,” presented at the SAE 2012 Commercial Vehicle Engineering Congress, 2012.
- [31] V. Pommé, “Reversible Heat Pump System for an Electrical Vehicle,” presented at the 1995 Vehicle Thermal Management Systems Conference and Exhibition, 1997.
- [32] J. H. Ahn, H. Kang, H. S. Lee, H. W. Jung, C. Baek, and Y. Kim, “Heating performance characteristics of a dual source heat pump using air and waste heat in electric vehicles,” *Appl. Energy*, vol. 119, pp. 1–9, Apr. 2014.
- [33] J. H. Ahn, H. Kang, H. S. Lee, and Y. Kim, “Performance characteristics of a dual-evaporator heat pump system for effective dehumidifying and heating of a cabin in electric vehicles,” *Appl. Energy*, vol. 146, pp. 29–37, May 2015.

- [34] D. Wang, T. Gao, W. Li, Y. Yang, J. Shi, and J. Chen, "System Characteristics of Direct and Secondary Loop Heat Pump for Electrical Vehicles," presented at the WCX World Congress Experience, 2018.
- [35] S. Bilodeau, "High Performance Climate Control for Alternative Fuel Vehicle," presented at the 1995 Vehicle Thermal Management Systems Conference and Exhibition, 2001.
- [36] D. Antonijevic and R. Heckt, "Heat pump supplemental heating system for motor vehicles," *Proc. Inst. Mech. Eng. Part J. Automob. Eng.*, vol. 218, no. 10, pp. 1111–1115, Oct. 2004.
- [37] J. M. Calm, "The next generation of refrigerants – Historical review, considerations, and outlook," *Int. J. Refrig.*, vol. 31, no. 7, pp. 1123–1133, Nov. 2008.
- [38] European Parliament, "Regulation (EC) No. 842/2006 of the European Parliament and of the council of 17 May 2006 on certain fluorinated greenhouse gases," *Official Journal of the European Union*, vol. L161, p. 11, Jun. 2006AD.
- [39] R. Mcenaney and P. Hrnjak, "Clutch Cycling Mode of Compressor Capacity Control of Transcritical R744 Systems Compared to R134a Systems," presented at the Vehicle Thermal Management Systems Conference & Exposition, 2005.
- [40] M. Petersen, C. Bowers, S. Elbel, and P. Hrnjak, "Development of high-efficiency carbon dioxide commercial heat pump water heater," *HVACR Res.*, vol. 19, no. 7, pp. 823–835, Oct. 2013.
- [41] D. Wang, B. Yu, J. Hu, L. Chen, J. Shi, and J. Chen, "Heating performance characteristics of CO<sub>2</sub> heat pump system for electrical vehicle in a cold climate," *Int. J. Refrig.*, vol. 85, pp. 27–41, Jan. 2018.
- [42] C. Bullard, J. Yin, and P. Hrnjak, "Transcritical CO<sub>2</sub> Mobile Heat Pump and A/C System. Experimental Model Results," *SAE Alternate Refrigerant Symposium*, 2000.
- [43] R. P. McEnaney, Y. C. Park, J. M. Yin, and P. S. Hrnjak, "Performance of the Prototype of a Transcritical R744 Mobile A/C System," presented at the International Congress & Exposition, 1999.
- [44] S. C. Kim, M. S. Kim, I. C. Hwang, and T. W. Lim, "Performance evaluation of a CO<sub>2</sub> heat pump system for fuel cell vehicles considering the heat exchanger arrangements," *Int. J. Refrig.*, vol. 30, no. 7, pp. 1195–1206, Nov. 2007.

- [45] M. Kim, "Fundamental process and system design issues in CO<sub>2</sub> vapor compression systems," *Prog. Energy Combust. Sci.*, vol. 30, no. 2, pp. 119–174, 2004.
- [46] World Meteorological Organization, "Scientific Assessment of Ozone Depletion: 2014, World Meteorological Organization," Global Ozone Research and Monitoring Project, Geneva, Switzerland, 55, 2014.
- [47] Y. Lee and D. Jung, "A brief performance comparison of R1234yf and R134a in a bench tester for automobile applications," *Appl. Therm. Eng.*, vol. 35, pp. 240–242, Mar. 2012.
- [48] L. Seybold, W. Hill, and C. Zimmer, "Internal Heat Exchanger Design Performance Criteria for R134a and HFO-1234yf," presented at the SAE 2010 World Congress & Exhibition, 2010.
- [49] Z. Qi, "Experimental study on evaporator performance in mobile air conditioning system using HFO-1234yf as working fluid," *Appl. Therm. Eng.*, vol. 53, no. 1, pp. 124–130, Apr. 2013.
- [50] G. Peri, S. Sambandan, and S. Sathish Kumar, "Cool Down Analysis of an HVAC System Using Multi-Zone Cabin Approach," presented at the WCX<sup>TM</sup> 17: SAE World Congress Experience, 2017.
- [51] ASHRAE, "Thermal environmental conditions for human occupancy." American Society of Heating, Refrigerating and Air-Conditioning Engineers, 2013.
- [52] M. Simion, L. Socaciu, and P. Unguresan, "Factors which Influence the Thermal Comfort Inside of Vehicles," *Energy Procedia*, vol. 85, pp. 472–480, Jan. 2016.
- [53] P. Danca, A. Vartires, and A. Dogeanu, "An Overview of Current Methods for Thermal Comfort Assessment in Vehicle Cabin," *Energy Procedia*, vol. 85, pp. 162–169, Jan. 2016.
- [54] ASHRAE, "Thermal environmental conditions for human occupancy." American Society of Heating, Refrigerating and Air-Conditioning Engineers, 1992.
- [55] S. Shah, "Integration of 1D and 3D CFD Software for Cabin Cool Down Simulation," presented at the WCX World Congress Experience, 2018.
- [56] H. Lee, Y. Hwang, I. Song, and K. Jang, "Transient thermal model of passenger car's cabin and implementation to saturation cycle with alternative working fluids," *Energy*, vol. 90, pp. 1859–1868, Oct. 2015.

- [57] M. A. Fayazbakhsh and M. Bahrami, "Comprehensive Modeling of Vehicle Air Conditioning Loads Using Heat Balance Method," presented at the SAE 2013 World Congress & Exhibition, 2013.
- [58] C.-Y. Tseng, Y.-A. Yan, and J. C. Leong, "Thermal Accumulation in a General Car Cabin Model," *J. Fluid Flow Heat Mass Transf.*, 2014.
- [59] J. Rugh, L. Chaney, L. Ramroth, T. Venson, and M. Rose, "Impact of Solar Control PVB Glass on Vehicle Interior Temperatures, Air-Conditioning Capacity, Fuel Consumption, and Vehicle Range," presented at the SAE 2013 World Congress & Exhibition, 2013.
- [60] S. Paulke, "Thermal Simulation of a Complete Vehicle Using Manikin Models," presented at the SIMVEC, Baden-Baden, Germany, 18-Nov-2014.
- [61] R. Yumrutaş, M. Kunduz, and M. Kanoğlu, "Exergy analysis of vapor compression refrigeration systems," *Exergy Int. J.*, vol. 2, no. 4, pp. 266–272, Jan. 2002.
- [62] E. Bilgen and H. Takahashi, "Exergy analysis and experimental study of heat pump systems," *Exergy Int. J.*, vol. 2, no. 4, pp. 259–265, Jan. 2002.
- [63] P. Byrne and R. Ghouali, "Exergy analysis of heat pumps for simultaneous heating and cooling," *Appl. Therm. Eng.*, vol. 149, pp. 414–424, Feb. 2019.
- [64] J. U. Ahamed, R. Saidur, and H. H. Masjuki, "A review on exergy analysis of vapor compression refrigeration system," *Renew. Sustain. Energy Rev.*, vol. 15, no. 3, pp. 1593–1600, Apr. 2011.
- [65] A. Hepbasli and O. Akdemir, "Energy and exergy analysis of a ground source (geothermal) heat pump system," *Energy Convers. Manag.*, vol. 45, no. 5, pp. 737–753, Mar. 2004.
- [66] E. Torres R, M. Picon Nuñez, and J. Cervantes de G, "Exergy analysis and optimization of a solar-assisted heat pump," *Energy*, vol. 23, no. 4, pp. 337–344, Apr. 1998.
- [67] M. V. Duarte, L. C. Pires, P. D. Silva, and P. D. Gaspar, "Experimental comparison between R409A and R437A performance in a heat pump unit," *Open Eng.*, vol. 7, no. 1, Apr. 2017.
- [68] W. L. Oberkampf and T. G. Trucano, "Verification and validation in computational fluid dynamics," *Prog. Aerosp. Sci.*, vol. 38, no. 3, pp. 209–272, Apr. 2002.
- [69] K. Umezu and H. Noyama, "Air-conditioning system for electric vehicles (i-MiEV)," SAE Automotive Refrigerant & System Efficiency Symposium, 2010.

- [70] İ. Dinçer and M. Rosen, *Exergy: energy, environment, and sustainable development*, 2nd ed. Oxford, UK ; Amsterdam, Netherlands ; Waltham, MA: Elsevier, 2013.

## **Vita Auctoris**

NAME: Carlo Ciacci

PLACE OF BIRTH: Treviso, Italia

YEAR OF BIRTH: 1995

EDUCATION: Liceo classico M. Foscarini, Venezia, Italy, 2009-2014  
Università degli Studi di Padova, Padova, Italy, 2014-2017  
Politecnico di Torino, Torino, Italy, 2017-2020  
University of Windsor, M.Sc., Windsor, ON, 2018-2019